AN EXPERIMENTAL TECHNIQUE FOR THE STUDY OF THE MECHANICAL BEHAVIOR OF THIN FILM MATERIALS AT MICRO- AND NANO-SCALE

by

Arash Tajik

A thesis
presented to the University of Waterloo
in fulfillment of the
thesis requirement for the degree of
Master of Applied Science
in
Mechanical Engineering

Waterloo, Ontario, Canada, 2008

Author's Declaration

I hereby declare that I am the sole author of this thesis. This is a true copy of the thesis, including any required final revisions, as accepted by my examiners.

I understand that my thesis may be made electronically available to the public.

Arash Tajik

Abstract

An experimental technique has been presented to probe the mechanical behavior of thin film materials. The method is capable of tensile testing thin films on substrate and free-standing thin film specimens. A mechanical gripper was designed to address the current challenges in gripping thin film specimens. In order to measure the strain field across the gage section, the moiré interferometry technique was used and the respective optical setup was designed.

A versatile microfabrication process has been developed to fabricate free-standing dog-bone specimens. Aluminum was used as the model material; however, any other metallization material can be integrated in the process. Thin film specimens have been characterized using SEM, AFM, and TEM. A process has been developed to fabrication diffraction gratings on the specimen by FIB milling. Different grating geometries were fabricated and the diffraction efficiency of the gratings was characterized. The structural damage induced by the Ga^{+} ions during the FIB milling of the specimens was partially characterized using STEM and EDS.

In order to extract the strain field information from the moiré interferogram data, a numerical postprocessing technique was developed based on continuous wavelet transforms (CWT). The method was applied on simulated uniform and nonuniform strain fields and the wavelet parameters were tuned to achieve the best spatial localization and strain accuracy.

Acknowledgment

I would like to express my sincere gratitude to my supervisor, Professor Hamid Jahed, for his guidance, support, and encouragement throughout my research. I am deeply inspired by his patience and passion for research. It has been an honor and a privilege for me to do research under his supervision.

I would also like to thank Professors Raafat R. Mansour and Pearl Sullivan for their invaluable suggestions and comments on my thesis.

The financial support from the Natural Sciences and Engineering Research Council of Canada (NSERC) is also appreciated.

A great portion of this research would have not been possible without the generosity of Professor Raafat R. Mansour, director of the Centre for Integrated RF Engineering (CIRFE), who kindly provided me access to the microfabrication facility in the CIRFE clean-room. I would like to thank the members of the CIRFE group for their invaluable assistance and guidance during the fabrication of my specimens. I am really indebted to Bill Jolley, Roger Grant, Mojgan Daneshmand, Arash Akhavan, Siamak Fouladi, Reena Al-Dahleh, and Tania Oogarah for sharing their knowledge.

I am grateful to Dr. Todd Simpson of the Nanofabrication Laboratory of the University of Western Ontario who passionately spent endless hours on the FIB milling of my samples with me. His knowledge and insight in this work is appreciable.

Likewise, I would like to thank Professor Dayan Ban for providing me access to his AFM facilities.

I sincerely thank Fred Pearson of the Canadian Centre for Electron Microscopy in McMaster University for the TEM analysis of my samples. The invaluable work of Marcia Reid of the Health Sciences Centre in preparing the TEM sections is highly appreciated.

The knowledge and efforts of my colleagues in our group was a valuable source of inspiration and success. In particular, Amin Eshraghi and Mohammad Noban are thanked for the great discussions we had.

Many thanks to Majid Yahyaei, Pedram Hassanzadeh, Hamidreza Alemohammad, Mohsen Shahini, Yaser Shanjani, Azad Qazizade, Omid Aminfar, and other wonderful friends. Their friendship has made the past two years full of joy and pleasure.

Above all, I am grateful to my parents, Reza and Maryam, and to my sister, Sara, for their endless love and continuous support in every single moment of my life. This thesis is dedicated to them.

Table of Contents

List of Figures

Chapter 1
Introduction

Thin film materials have been widely used in microelectronics, microelectromechanical systems (MEMS), and optics, as well as surface coatings to perform electrical, optical, thermal, mechanical, magnetic, tribological, or biological functions.

In this chapter, the technological and scientific motivation to study the mechanical properties of thin film materials is presented. Since the main objective of this research was to develop a technique to study the mechanical behavior of thin film materials, a brief comparative background of the current mechanical testing techniques is discussed in section 1.2. Finally, the objective and the organization of the thesis are presented in section 1.3.

1.1 Motivation: Study of the Mechanical Behavior of Thin Films

The microelectronics industry has been consistently driven by the scaling roadmap, colloquially referred to as the Moore's law. Consequently, during the past decades, integrated circuits have scaled down further. This shrinkage could have never been possible without the efficient integration and exploitation of thin film materials.

Thin film materials, on the other hand, are the essential building blocks of the micro- and nano-electromechanical systems (MEMS and NEMS). These devices are the main components of many sensors and actuators that perform electrical, mechanical, chemical, and biological functions. In addition to the wide application of thin film materials in micro- and nano-systems, this class of materials has been historically utilized in optical components, wear resistant coatings, protective and decorative coatings, as well as thermal barrier coatings on gas turbine blades.

In some applications, thin film materials are used mainly as the load-bearing component of the device. Microelectromechanical systems (MEMS) are the example of these applications. Thin film materials carry mechanical loads in thermal actuators, switches and capacitors in RF MEMS, optical switches, micro-mirror hinges, micromotors, and many other miniaturized devices. In these applications, one of the main criteria to choose a specific material is its ability to perform the mechanical requirements. Therefore, a clear understanding of the mechanical behavior of thin film materials is of great importance in these applications. This understanding helps better ana-

lyze the creep in thermal actuators [1,2], to investigate the fatigue of polysilicon [3,4] and metallic micro-structures [5,6], to scrutinize the relaxation and creep behavior of switches made of aluminum [7,8] and gold films [9], to study the hinge memory effect (creep) in micro-mirrors [10], and to address the wear issues in micro-motors. [11]

In some other applications, the thin film material is not necessarily performing a mechanical function. However, during the fabrication process or over the normal life, the device experiences mechanical loads and hence may suffer from any of the mechanical failure issues. Examples of these cases are the thermal fatigue in IC interconnects [12], strain ratcheting in passivated films [13,14], the fracture and delamination of thin films on flexible substrates [15], the fracture of porous low-k dielectrics [16], electromigration [17], the chip-package-interaction (CPI) [18], and thin film buckling and delamination [19].

In order to address the above-mentioned failure issues and to design a device that has mechanical integrity and material reliability, an in-depth knowledge of the mechanical behavior of thin film materials is required. This information will help design engineers, integrate materials and design devices that are mechanically reliable and can perform their specific functions during their life-time without any mechanical failure.

In addition to the tremendous industrial and technological driving force that was mentioned earlier, there is a strong scientific motivation to study the mechanical behavior of thin film materials. The mechanical behavior of thin film structures have

been known to drastically differ from their bulk counterparts. [20] This discrepancy that has been referred to as the length-scale effect has been one of the main motivations in the scientific society to study the mechanical behavior of thin film materials. In order to provide fundamental mechanistic understanding of this class of materials, old problems and many of the known physical laws in materials science and mechanical engineering have to be revisited from a different and multidisciplinary prospective. These investigations will not be possible unless a concrete understanding of the mechanical behavior of thin film materials is achieved through rigorous experimental and theoretical research in this area.

1.2 Testing Methods for Thin Films

In order to probe the mechanical behavior of thin film materials different approaches have been used by researchers. Tensile testing [25-70], nano-indentation [21], buldge test [22,23], curvature method [24], micro-beam bending [24], and a few other techniques were used to measure the mechanical properties of thin films on substrate and free-standing thin films. Among these methods, the first four techniques were more popular among the researchers and different measurements have been carried out using these methods.

In tensile testing, the film is patterned into a dog-bone shape specimen and is then loaded in tension. By monitoring the load and strain across the gage length the mechanical properties of the film in different load conditions namely monotonic, fati-

gue, creep, and relaxation can be found. Although tensile testing has been the primary method of experimental work in macro-scale applications, it has not been very popular among the thin film researchers, due in part to the difficulties in specimen handling, gripping, and strain measurements. The tensile testing has the advantage that all of the properties of the material can directly be extracted from the measurement data and no calibration model is required. On the other hand, all loading conditions can be applied to the specimen. Free-standing films and films on substrate can be tested using this technique.

In buldge test method, a thin film specimen is loaded by a hydrostatic pressure and the deflection of the specimen is monitored. The pressure-deflection data is then correlated to the actual plain stress-strain behavior of the material through a correlation model. Free-standing single layer and multi-layer materials can be tested by this technique. Only the application of this method in monotonic static tests has been reported in the literature.

Nano-indentation is the advanced version of the classic hardness test method. In this technique, the specimen is loaded by a sharp indenter and the load-displacement (P-h) of the indenter is monitored during loading and unloading. The reduced elastic modulus and hardness are the two material parameters that can be extracted from the P-h data. This method can only be used for thin films on substrate. However, due to the straight-forward approach and the relative ease of use, this method has been popular among researchers.

Curvature method is one of the early methods that was used to probe the mechanical behavior of the thin film materials on substrate. In this method, the initial curvature of a substrate is measured and then the film material is deposited on the substrate. The variations in the curvature of the substrate before and after the deposition of the film are a good measure of the residual stresses in the film. On the other hand, this method can be used to investigate the mechanical behavior of thin film materials on substrate under temperature cycling.

Among the aforementioned experimental methods, tensile testing technique is the only technique that can be used to extract the mechanical behavior of thin film materials under different loading conditions. In this method, all material parameters can be directly measured from the experimental data and it provides a straightforward approach to the measurement. However, as it was discussed earlier, due to the difficulties in sample preparation, handling, and gripping and because of the uncertainties involved in the measured strains this method has not been widely used in micro- and nano-scale. If these challenges are met, this technique can become a versatile method of probing the mechanical behavior of thin film materials at micro- and nano-scale.

1.3 Objectives and Outline of the Thesis

The main objective of this thesis is to design and develop a technique that can be used to experimentally probe the mechanical behavior of thin film materials at mi-

cro- and nano-scale. The method is based on the tensile technique that has been used for decades in macro-scale applications and is to address the current challenges involved in tensile testing of thin film materials. In this thesis the process of developing and evaluating such a technique is presented. The organization of the thesis is as follows:

In Chapter 2, the current methods of tensile testing are reviewed in detail. A brief overview of all methods is presented. A detailed discussion is then given to each individual challenge, namely sample preparation, gripping, load actuation and measurement, and strain measurement.

In Chapter 3, the experimental setup that was proposed in this thesis is described. Design requirements are reviewed, and a test rig is designed and developed based on the specific requirements. A novel gripper is proposed, loading setup has been designed, and a strain measurement technique based on moiré interferometry has been developed. The optical setup is discussed in this chapter and the related results are presented. Finally, the software and control setup of the experimental equipment are discussed.

In Chapter 4, the sample preparation procedure has been introduced and the results of developing a microfabrication process to fabricate free-standing dog-bone thin film specimens are discussed. The SEM, AFM, and TEM characterizations that were performed on the fabricated specimens are also presented in this chapter. In order to use moiré interferometry, a series of diffraction gratings have to be fabricated on the surface of the specimen. In this chapter, the process of fabricating these dif-

fraction gratings using the Focused Ion beam (FIB) instrument is discussed and the related characterizations are presented. The ion damage to the sample is also scrutinized in this chapter.

In Chapter 5, a method of extracting the strain field data from the interferogram images is proposed based on Continuous Wavelet Transforms (CWT) and wavelet ridge detection. The wavelet parameters are tuned using a set of simulated interferograms representing uniform and nonuniform strain fields. The strain accuracy and spatial resolution of the method is also discussed.

Finally, in Chapter 6 the concluding remarks of the thesis are presented and the recommendations for future work are proposed.

Chapter 2

Tensile Testing Techniques for Thin Films; Background

Tensile testing technique is a versatile tool to study the mechanical behavior of thin film materials. Since in tensile testing, the stress and strain states are directly related to the measured values of load and displacement, no calibration model or post-processing is required. Therefore, comparing to other techniques such as nano-indentation, buldge test, and substrate curvature, tensile testing can provide the material characteristics with less ambiguity. However, when this technique is used for the mechanical testing of thin film materials, there are a number of issues that make the testing procedure complicated and in cases less accurate. Sample preparation, gripping, alignment, loading, and strain measurement are among these issues.

During the past decade many researchers have tackled these issues from different prospective. In this chapter, these efforts are reviewed and discussed. In section 2.1, a brief review of all the related works is presented. A detailed discussion is dedicated to challenges in sample preparation, gripping, loading, and strain measurement in sections 2.2 to 2.5.

2.1 Overview

The early efforts in the tensile testing of thin films were the concurrent research work of Ruud *et al* [25], Koskinen *et al* [26], and Read *et al* [27] in the early 1990's. Ruud *et al* [25] introduced a tensile testing technique to test free standing thin film specimens with gage section area of 10 mm long by 3.3 mm wide. They sandwiched the specimen ends between polished aluminum grippers using 5μm thick copper films and used a motor-driven micrometer for loading. Strain was measured by monitoring the displacement of laser spots diffracted from a series of lithography patterned photoresist islands. With this technique, they managed to determine the Young's modulus, Poisson's ratio, and yield strength of free-standing Cu, Ag, and Ni films [25] and Ag/Cu multilayers [28], and to study the yield strength [29] and anelastic behavior [30] of thin Cu films on Kapton substrate.

Koskinen *et al* [26] used a relatively simple technique to test LPCVD polysilicon films. They introduced a gripping setup that could hold an array of 20 samples and was capable of loading individual specimens. Specimen ends were glued to the

gripper and loaded by a motor driven stage. Gripper displacement was measured and used to calculate the strain.

While both of these techniques suffered from a reliable gripping and load train alignment, Read *et al* [27,31] developed a sample fabrication procedure that could meet the demanding gripping and alignment issues, simultaneously. In their method, films were deposited on silicon substrate and after patterning the film to a dog-bone shape, the substrate was etched from the backside to open a window frame under the film, leaving it free-standing. After mounting the specimen in grippers, the frame edges were cut so that only the film is carrying the load. In this way, since the thick substrate is mounted in gripper jaws, there would be less slip and alignment will be an easier task. The concept of free standing film on supporting frame was used by other researchers to overcome the alignment issues [32-37, 40-42, 52, 53]. This setup was later on improved by adding laser speckle interferometry [38] and Digital Image Correlation (DIC) [39] to measure in-plane strains. E-beam evaporated Ti-Al-Ti multilayer [27], polySi, aluminum and its alloys, and electrodeposited copper [39] were tested using this technique in the temperature range of 25-200ºC.

Sharpe *et al* [40-44] used interferometric strain displacement gage (ISDG) technique to measure strains in free-standing films under tensile loading. The ISDG was originally developed in the late 1980's for strain measurement in a non-contact mode [45-47] for macro-scale high-temperature applications [48]. This technique is based on Young's two-slit interference [49] generated from the diffraction of a laser beam from two sufficiently separate markers. Tensile behavior of polysilicon [40] and

silicon nitride [44] were studied using this technique. Oh *et al* [43] used this technique to investigate thermal expansion and creep behavior of polysilicon films, while Zupan and Hemker [50,51] studied the high temperature properties of γ-TiAl micro samples.

The tensile behavior of free standing gold films was studied by Emery and Povirk [52,53]. They used the procedure of Read *et al* [27] for sample preparation and measured the cross-head displacement for strain calculations. Cornella and Bravman [32,35] used the same concept to study the mechanical behavior of thin films with an emphasis on time dependent behavior of Al films. [33-37]

Allameh and Soboyejo [54,55] investigated fatigue behavior of LIGA Ni thin films under tensile loading. They used Focused Ion Beam (FIB) to mill 1μm deep markers on the specimen surface and monitored the motion of these markers under an optical microscope to calculate strain. Since LIGA films are relatively thick, i.e. a few tens of micrometers, they used common mounting methods for specimen gripping.

The advent and wide-spread availability of high resolution microscopy techniques led some researchers to use *in situ* tensile testing methods to characterize the mechanical behavior of thin films. Atomic Force Microscopy (AFM), Transmission Electron Microscopy (TEM), and Scanning Electron Microscopy (SEM) were among the instruments that were used for *in situ* studies. These techniques were utilized either to measure strain or to study the micro-structural deformations during specimen loading. Chasiotis and Knauss [56-58] used AFM to measure the changes in surface topography during the loading and correlated this measurement to strain field using

Digital Image Correlation (DIC). They also revised the electrostatic gripping technique, originally proposed by Tsuchiya *et al* [59,60], to prevent specimen slipping during the long-time AFM scans for each measurement point. They used this technique to study the influence of surface conditions [61] and the size effect of elliptical and circular perforations [62] on the mechanical strength of polysilicon. Chasiotis *et al* [63] used the same setup to study the strain rate effect on the mechanical behavior of Au films. However, due in part to the slow scan rate of AFM, they used cross-head displacement for strain measurements. Zhu *et al* [64] integrated the specimen with the loading system in a MEMS based device and used AFM to measure strains in polysilicon films under uniaxial tensile loading.

Haque and Saif [65,66] proposed a quantitative technique to study the deformation mechanisms in Al and Au nano-scale thin films. They used a MEMS device to load samples in TEM and SEM. Using same technique, Samuel *et al* [67] studied the relaxation of Au films and Rajagopalan *et al* [68] reported the plastic deformation recovery in Al and Au thin films.

The above-mentioned methods were among the main research activities that used tensile testing to study the mechanical characteristics of thin film materials. Each research group built its own test set up and regarding the requirements for a specific test procedure, they developed a technique that met their requirements. In the following sections, the different parts of the current tensile testing devices, including gripper, loading system, and strain measurement subsystem along with the sample preparation process is discussed in more detail.

2.2 Sample Preparation

Sample preparation is one of the main challenges in tensile testing of thin film specimens. Thin film materials are usually fabricated using one of the deposition techniques, namely Physical Vapor Deposition (PVD) or Chemical Vapor Deposition (CVD). In order to utilize either of these techniques to fabricate free-standing thin film "dog-bone" specimens, a designated process has to be developed. This process depends on the specific requirements defined by the choice of gripping and sample handling method, the film material and deposition technique, and the availability of the specific procedures in any fabrication laboratory. This tedious process usually takes a good amount of time and effort and is necessary for any material under study.

Ruud *et al* [25] used a relatively simple technique to fabricate free-standing films. They evaporated Cu and Ag films on glass substrate and after patterning the film to a dog-bone shaped specimen, they took the films off the substrate by sliding a razor blade underneath them while submerged in water. For Ni films, glass substrate was first coated with a layer of photoresist and Ni was then sputter deposited on it. The film was then released by etching the resist in acetone. Although both processes developed by Ruud *et al* [25] are relatively simple, films are prone to be damaged and wrinkle while releasing. The author's past experience in microfabrication shows that releasing specimens in acetone results in highly wrinkled films caused, in part, by the resist residues left on the sample.

The concept of using a window frame in substrate which was originally introduced by Read *et al* [27] was among the most popular methods that was used and fur-

ther developed by other researchers. In this process, double-sided polished (DSP) <100> silicon wafers, were first coated by a thin layer of silicon oxide. Oxide layer on front-side was patterned and etched at specimen locations. Ti-Al-Ti multilayer was then deposited by e-beam evaporation and patterned to dog-bone shape specimens. The oxide layer on both sides was then patterned and etched in HF to form a hard mask for silicon substrate etching. Silicon was then etched in hydrazine to open window frames. Sharpe *et al* [42] utilized this technique to test thin polysilicon films. Figure 2-1 shows a silicon carbide specimen that was fabricated by Edwards *et al* [44] using this concept. Emery and Povirk [52,53] used the same process to fabricate e-beam evaporated gold. The main issue with this technique is the long Si substrate etching times that may cause the specimen film be attacked during etching process and special care is required in this regard.

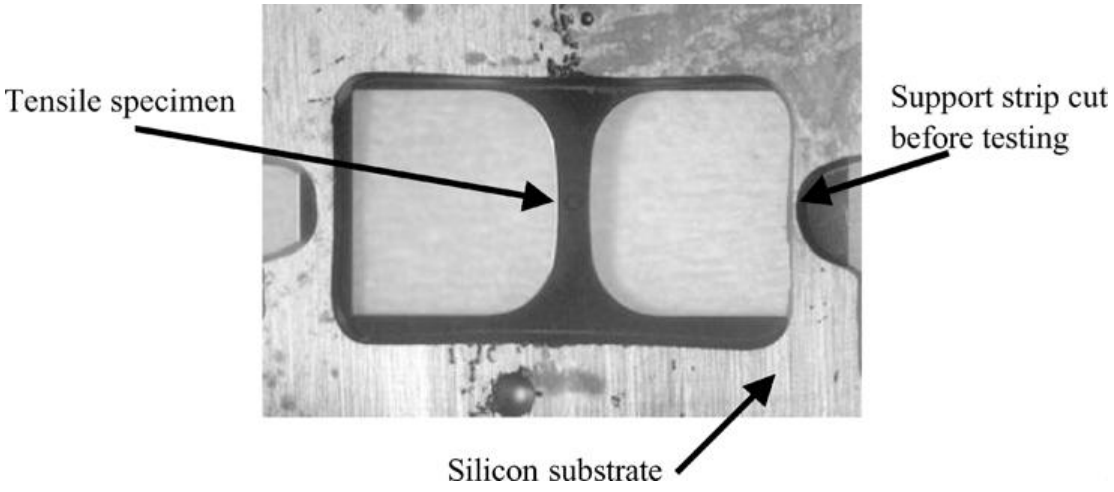

Figure 2-1- A free-standing silicon carbide specimen on substrate window frame. [42]

Cornella [32] improved this concept by using dry etching processes rather than wet etching processes to fabricate specimens with higher film quality and process yield. In their process, Si substrate was first coated on front side with 1μm thick LPCVD silicon nitride to be used as an etch stop. Aluminum was then sputter deposited on front side and patterned to the dog-bone shape. Backside of the substrate was coated with thick photoresist to act as the etching mask during substrate etching. Silicon substrate was entirely dry-etched until it reached silicon nitride layer. This layer was then removed in RIE to release the aluminum specimen. A specimen fabricated through this process is shown in Figure 2-2.

A few researchers, who mainly worked on the mechanical behavior of polysilicon, used factory processes like polyMUMPS to fabricate their specimens. Although these processes are well developed and are readily available, they are limited to a few thin film materials, most of which are silicon based.

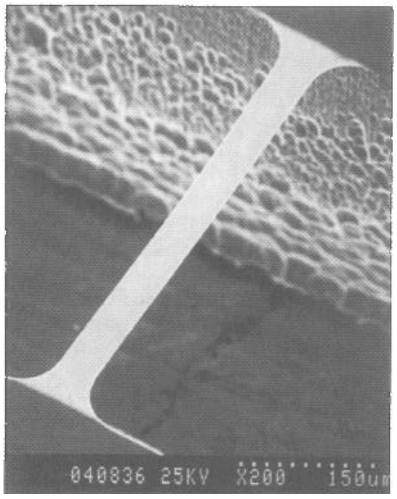

Figure 2-2- SEM image of an Al free-standing film on window frame. [33]

When metallic materials are used as the structural layer, traditional silicon-based films are not good choices for sacrificial layer. A common practice in the fabrication of metallic devices in Radio Frequency Microelectromechanical Systems (RF MEMS) is to use polymers as the sacrificial layer. Chasiotis *et al* [63] used this technique to fabricate tensile specimens of Au films. As shown in Figure 2-3, they used PMMA and AZ 4110 photoresist as the sacrificial material for electroplated and evaporated Au films, respectively. For electroplated Au films, a molding process was utilized to pattern gold on PMMA and sacrificial layer was then etched to release the film. Evaporated Au films, however, were lithography patterned and the photoresist sacrificial layer was then stripped to release the structure. Although polymeric sacrificial layers are easier to remove and hence result in less attack to the metallic film, they are less applicable when high temperature processes are involved. In fact in high temperatures two problems arise; above the glass transition temperature, polymer layer starts a significant flow which causes deformation and wrinkling in the metallic film; on the other hand, the thermal mismatch between the polymer and the metallic film causes significant stresses on the film that, in high temperatures, may result in creep and permanent deformation. [69]

In conclusion, among the sample preparation processes that were reviewed in this section, the two strategies of using either a window frame in substrate or polymeric sacrificial layer seem more versatile and reliable than other techniques and depending on the test setup design either case can be utilized.

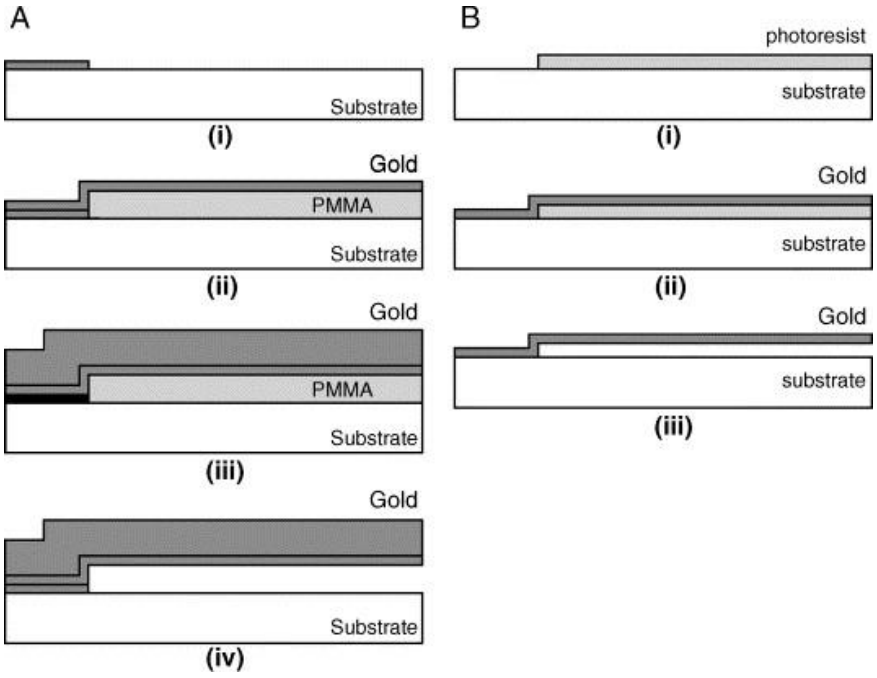

Figure 2-3- Microfabrication process for electroplated (a), and evaporated (b) dog-bone specimens [63]

2.3 Gripping

Gripping a film that usually has smaller thickness than even the surface roughness of the macro-machined grippers is a tough challenge. Under these circumstances, the film may slip or experience high stresses at the griper due, in part, to stress concentrations. On the other hand, aligning the two grippers is, in fact, a demanding task. Therefore, many researchers have designed and utilized a variety of gripping techniques to overcome this issue.

Ruud *et al* [25] sandwiched the free-standing thin film specimens between polished aluminum grippers using 5μm thick Cu foils. The concept of window frame in

substrate [27,32] has made gripping much easier and common macro-machined grippers can be used to mount thick end grips of the specimen which is basically the thick silicon substrate rather than the thin film. As shown in Figure 2-4, Greek and Johnson [70,71] used a connecting ring as a gripper. They inserted a probe connected to the load-train setup in the ring and loaded the specimen. Buchheit *et al* [72] used the same concept to pull micromachined silicon films. A cylindrical sapphire nano-indenter tip was inserted into the so-called "pull-tab" and utilizing the lateral loading capability of a nano-indenter, samples were loaded in tension. Emry and Povirk [52,53] used the same technique for pulling tensile specimens on a substrate window frame.

Tsuchiya *et al* [59,60] introduced a novel technique to grip tensile testing specimens using electrostatic force. This technique is schematically shown in Figure 2-5. In this technique, a free-standing specimen with large end grip (puddle) is fabricated and is fixed to the gripper by electrostatic force. Specimen can be easily fixed to and released from the gripper by changing the polarity of the applied voltage.

Sharpe *et al* [73] argued that although the electrostatic gripping is very useful in static tensile tests, it fails during tension-tension fatigue testing. To overcome this issue, they glued a silicon carbide fiber to the puddle using viscous UV curable adhesive.

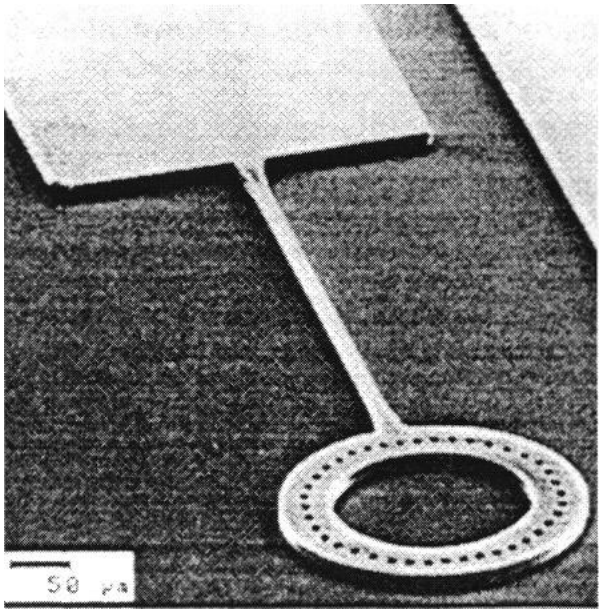

Figure 2-4- Tensile testing specimen with a ring at one end for gripping and loading [70]

Chasiotis and Knauss [56] also reported that specimens mounted by electrostatic gripping slip during long-time static loadings and they experienced rigid-body motion of the specimen during their long-time AFM scans for deformation measurement. It was shown that the electrostatic gripping is only reliable when the applied tensile loads are below 0.1 N for their specimen geometry. They improved the technique by combining the electrostatic actuation with UV adhesive to meet their demanding requirements for a no-slip reliable gripper. (Figure 2-6)

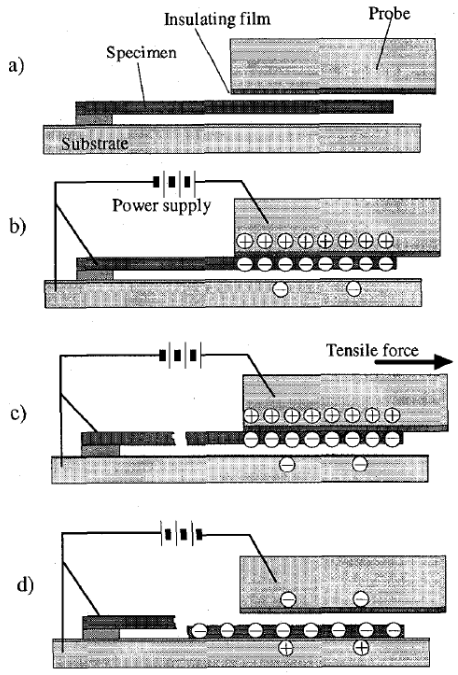

Figure 2-5- Schematic representation of electrostatic gripping technique. [59]

In conclusion, the application of substrate frame window concept makes griping much easier in expense of having a more complex specimen fabrication process. The electrostatic gripping, although seems straight forward, is only applicable for static low-load (<0.1 N) tests. The utilization of adhesive layer is necessary when conducting time-dependant tests or applying a dynamic load that requires a reliable no-slip gripper.

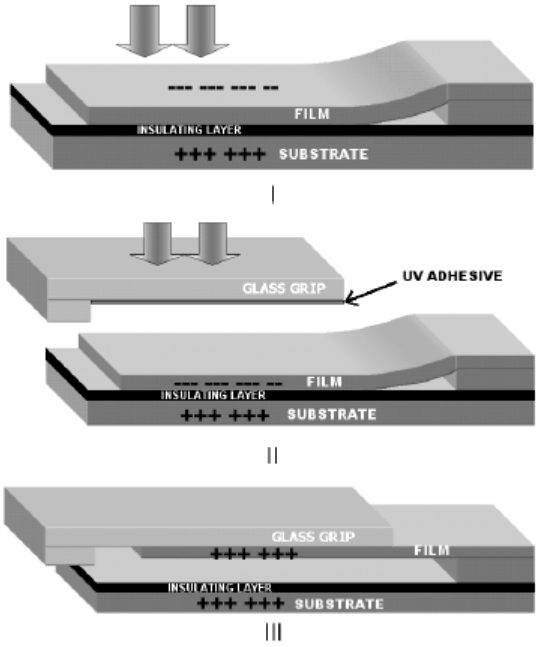

Figure 2-6- Combination of the electrostatic and UV adhesive gripping. [56]

2.4 Load Actuation and Measurement

Having prepared the samples and mounted them in gripers, they had to be loaded to the required load level and the load value has to be measured. With the availability of different types of commercial actuators and load cells, this part of a tensile testing setup is not as challenging as the other parts. Piezo driven actuators were among the popular tools for loading which provided the capability of loading the specimen with different waveform functions and work at low and high frequencies. If they are fitted with any type of displacement sensor, e.g. strain gage, LVDT, or capacitive sensors, they can be controlled in a close-loop system in order to compensate for hysteresis and drift. On the other hand this displacement feedback was

recorded in tensile setups that the cross-head displacement was used for the measurement of strain. Many of the research works discussed earlier in this chapter are equipped with this type of actuators [27, 32, 40, 50, 54]. Inchworm [56] and motor-driven micrometer [25] actuators are also among the type of actuators that were used for specimen loading. Sharpe *et al* [73] used a loud-speaker operating at 20 kHz in their early fatigue tests on polysilicon to dynamically load their specimens. Almost all research groups used strain gage-based load cells to measure the applied load and hence the stress.

A specific group of tensile test setups are those that have integrated the load-actuation and measurement with the specimen itself on a MEMS-based tensile testing device. These devices provide much higher resolution for load actuation and load measurement, making them a versatile tool to study the mechanical properties of nano-scale structures like carbon nanotubes and nano-wires [74], and films that are substantially thin or have very small gage section areas that have a demanding load resolution.[65] On the other hand, because of their small size they can be used for *in situ* study of deformation in Scanning Electron Microscope (SEM) or Transmission Electron Microscope (TEM).[64-68] However, these devices are not so applicable at the length scale where most of the thin films are usually fabricated and used in MEMS and microelectronics applications.

In summary, loading and load measurement is the most straight-forward part of the setup and can be provided from the commercially available products.

2.5 Strain Measurement

The measurement of strain is the most challenging part of the tensile testing of thin film specimens. Due to the small size of thin films, none of the current macro-scale methods of strain measurement are applicable to tensile testing of thin films. Thin film specimens are at the same size of resistive strain gages and are too small for LVDT-based extensometers. Technically, any method of strain measurement that is used in contact with the specimen is not useful. Therefore, many researchers have developed or adapted non-contact strain measurement techniques to measure the strain during tensile testing. These techniques can be categorized into four different groups, including cross-head displacement; optical imaging; interferometry-based methods; and advanced microscopy techniques like AFM, SEM, and TEM for *in situ* strain measurement. In what follows, these methods are discussed in detail.

Read *et al* [27] monitored the cross-head displacement and used it as a measure for strain. There are many sources of error involved in this technique. Specimen may slip at the gripper. On the other hand, the gripper itself may have clearances that cause backlash during the changes in load direction. Compliance of the test setup is the other source that deteriorates the accuracy of the method. The cross-head displacement is a combination of all of the deformations in the load train, i.e. the deformations in load-cell, load actuator, the test rig, grippers and albeit in the specimen itself. Therefore, this measurement will not provide an accurate measure of stain in the gage section of the sample.

Cornella [32] measured the compliance of the test setup by compressing the load actuator to the load cell in the absence of specimen and subtracted this compliance from the actual measurements to find the deformation in the specimen. They reported that 76% of the measured displacement accounts for the actual deformation in the specimen [33]. In order to validate the strain relaxation measurements and to show that the drop in the stress level over time is the actual behavior of the specimen itself and not the test setup, they used iridium specimens. Iridium, due to its high melting point, has a very low relaxation at room temperature. Since these tests revealed no relaxation, they argued that their test setup is stiff enough and that the relaxation behavior that they monitored during the tensile testing of Al films is the actual material behavior.

Chasiotis *et al* [63] used the cross-head displacement to study the relaxation in gold thin films. They measured the deformation of the load-cell and the apparatus compliance and subtract it from the results. Due to the high compliance of their specimens compared to the setup, 99% of the cross-head displacement was due to the deformation in the specimen. They verified the accuracy of the crosshead displacement method by testing brittle materials with known elastic modulus.

Greek and Johnson [70] cancelled out the effect of the compliance of the test setup by testing specimens with identical gages section areas and different gage lengths. Assuming that the compliance of the test setup is constant for any test, they calculated the deformations caused by test setup and subtract it from the test results.

This method is only applicable to the cases that the compliance of the specimens are sufficiently different at different gage lengths.

Emry and Povirk [52] also measured the displacement in grippers by monitoring the displacement of two markers using a video camera. They argued that their method has the limitation that the measured strain is not the actual strain in the gage section. They also reported a non-linearity in the stress-strain curve in low loads. Figure 2-7 shows this non-linearity which is technically an experimental error. They extrapolated the linear portion of the results to find the zero point of stress-strain curve. Due to this non-linearity in the curve, calculating the yield stress using the 0.2% offset rule was erroneous. Therefore they found the yield point by defining it as the point where the slope of the σ-ϵ curve drops to one tenth of the elastic modulus.

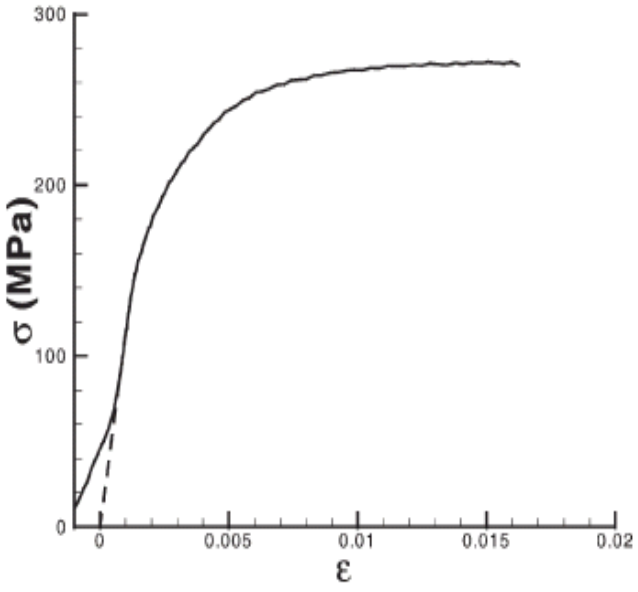

Figure 2-7- Stress-strain curve of gold thin films, showing non-linearity at low loads. The dashed line is fitted to the curve to find the zero point. [52]

Due to the uncertainties involved in the application of cross-head displacement for strain measurements, a number of techniques have been introduced to measure the strain directly on the gage section. An inexpensive way of measuring strain is to put markers on the specimen's gage section and monitor their displacement using a camera. Allameh *et al* [54] used a video camera and monitored the deformation of two markers milled by Focused Ion Beam (FIB) on LIGA Ni specimens. Markers were 300μm apart and were located by block matching in a series of images captured by a camera during tensile testing. They have not discussed the accuracy of their setup; however, they reported that the strains that were measured as such were only used in the plastic deformation regime. Assuming a gage length of 300μm, the displacement resolution required to have 10μstrain resolution is about 3 nanometers. Therefore, for a commercial CCD camera with nominal pixel size of 6μm, at least a 2000X magnification should be utilized to be able to capture a 3nm displacement. However, in this magnification, the field of view (FOV) of the objective is so small that the two markers cannot be fit in a single image, simultaneously. To overcome this issue, two different approaches have been used. Cheng *et al* [39] used a low magnification (350X) to fit 180μm-apart markers in a single image. Utilizing the digital image correlation (DIC) method, they post-processed the data to the resolution of 0.02 pixel. For their optical setup, this resolution is the equivalent of 0.01μm displacement on the specimen which translates to 55μstrain resolution for a 180μm gage length. Since compared to other techniques, usually less or no preparation is required on the surface of the specimen and inexpensive optical imaging equipment can be

used for this purpose, this method is becoming more popular among researchers. The only disadvantage of DIC is that this method is computationally expensive and requires hours of post-processing.

In another attempt to tackle the small FOV issue in high magnifications, Ogawa *et al* [75] proposed a double field of view approach. As shown in Figure 2-8, a low magnification objective is used to view the two markers which were 1-1.4mm apart. Image of each marker position was then magnified on a separate CCD and their displacement was monitored. In their technique, they could measure displacements to better than 1μm corresponding to 0.1% strain for a 1mm gage length.

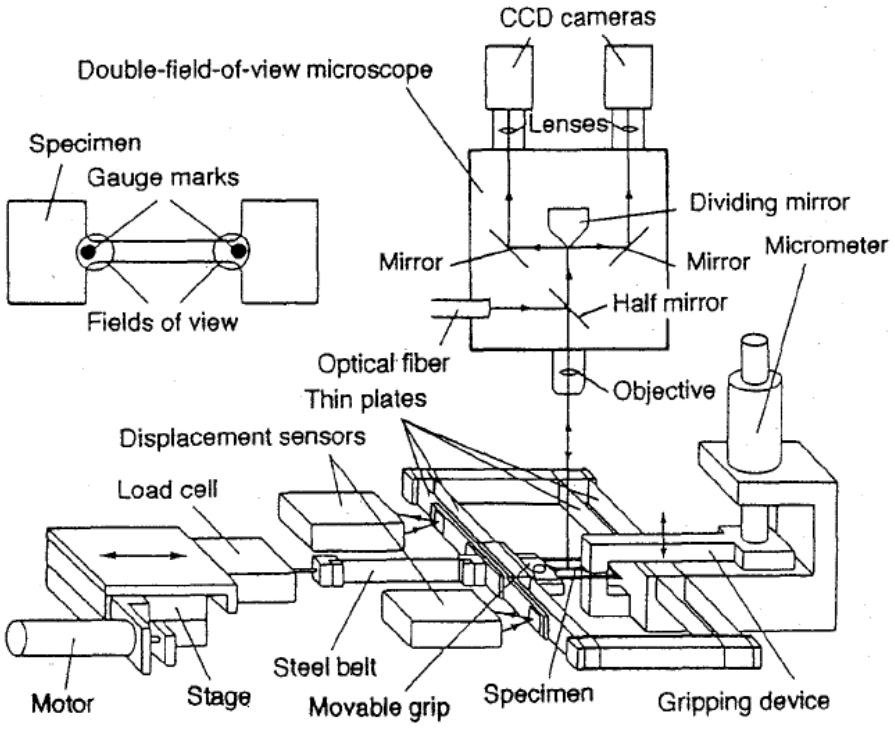

Figure 2-8- Double field of view microscope setup for strain measurement [75]

Ruud *et al* [25,28-30] patterned a two-dimensional area of photoresist islands on the specimen and monitored the displacement of the diffracted spots from these islands to directly measure the strain on the gage section. As shown in Figure 2-9, presence of the photoresist islands results in diffraction pattern when a laser beam is illuminated on the surface of the sample. Diffracted spots are then detected using a two-dimensional position sensor. By monitoring the displacement of these spots, the relative displacement of the islands and hence the specimen deformation can be measured. In this setup, system works in the third diffraction order and the distance between the sample and position detector serves as an optical lever for magnification. They reported that the resolution of the system is limited by the signal-to-noise ratio of the detector and provides strain resolution of 50μstrains.

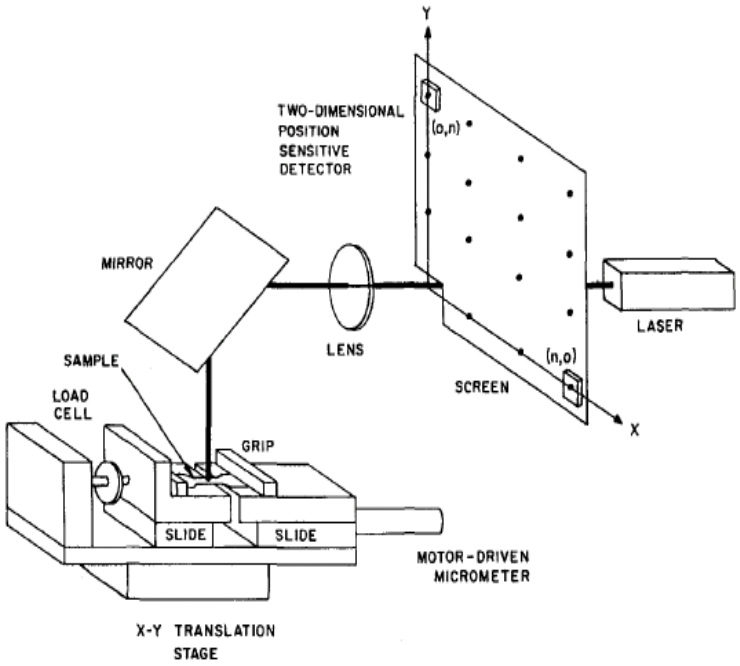

Figure 2-9- Schematic diagram of the setup to use diffraction spots for strain measurement [25]

The main advantage of this technique is that since axial and lateral strains can be measured simultaneously, not only Young's modulus but also the Poisson's ratio can be calculated. Since the modulus of the photoresist islands is sufficiently lower than the film's, their presence has no effect on the mechanical behavior of the specimen material.

The aforementioned techniques were all based on optical imaging. The main issue with imaging techniques is that their resolution is limited by the optical setup, and more specific, the magnification and the CCD resolution. An advanced method of improving the resolution of optical devices is to use light interference. This approach which is the basis of interferometry techniques has been used by a few researchers for strain measurement in thin film materials.

Sharpe *et al* [40-44] used Interferometric Strain/Displacement Gage (ISDG) method to measure axial and lateral strains in thin film specimens. ISDG was originally proposed by Sharpe [45-48] in the late 1980s to measure strains in macro-specimens in non-contact mode. The principle of this technique is based on the diffraction and interference of light from two slits, i.e. Young's two slit interference. In this method, two markers are put on the specimen. They can be fabricated either by nano-indentation or by FIB-assisted deposition. When the laser beam is illuminated on them the beam is diffracted. The diffracted beams interfere to form interference fringes. The frequency of the fringes is directly proportional to the distance between the two markers. When the specimen is elongated under the applied load, the distance between the two markers varies, resulting in a change in the fringe frequency. By

monitoring this frequency the strains can be directly calculated on the specimen. Since the fringe frequency is also affected by the rigid-body motion of the specimen, two separate detectors have to be used to cancel out the effect of this motion. A schematic of this setup is shown in Figure 2-10. In the original setup, in order to measure the strains from the fringe data, the location of the fringe minimum was isolated at the beginning of the test and was followed through a complex algorithm. In this algorithm only a small part of the optical signal was used and most of it which contained a lot of information was omitted in calculations. With this algorithm, the strain resolution was 5μstains with uncertainty of ±30μstrains. Zupan *et al* [76] used Fourier Transforms on the whole optical signal and improved the uncertainty of the technique to ±15μstrains. An advantage of ISDG is that if markers are placed along the width of the specimen, the lateral strains and hence the Poisson's ratio can also be measured with this technique. However, since the markers has to be at least 300μm apart, [77] wide specimens have to be utilized.

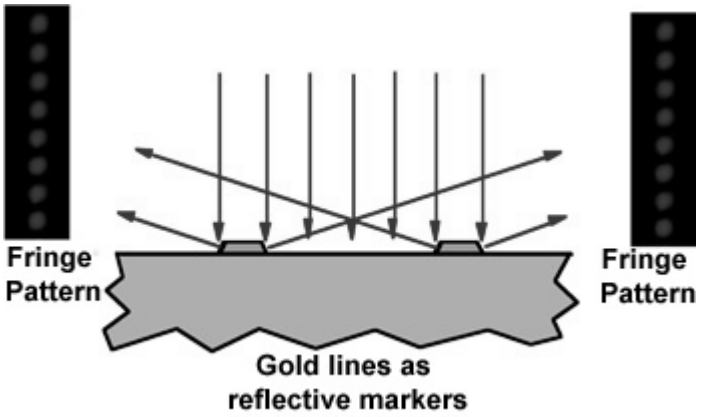

Figure 2-10- Schematic representation of ISDG technique. [40]

In another effort to use interferometric measurement techniques, Read [38] used speckle interferometry to measure in-plane strains in thin film specimens. The main advantage of speckle interferometry is that since it uses the speckles caused by the surface topography, no surface preparation or marker fabrication is required. However, it is usually computationally expensive and has low signal-to-noise ratio. In this technique, instead of the strain, the strain rate was measured in the elastic deformation regime and was used to calculate the modulus of elasticity. The uncertainty of the calculated modulus was reported to be 5%.

The last group of strain measurement methods were those that used advanced microscopy techniques to measure the strain in thin films. The challenges involved in using optical microscopy led researchers to use other microscopy techniques like AFM, SEM, and TEM to measure the deformation of thin films specimens. On the other hand, these techniques provided an insight into the microstructural deformation of thin film materials during loading.

Chasiotis *et al* [56-58] monitored the surface topography changes during loading using Atomic Force Microscopy (AFM). Correlating the AFM images of the deformed and undeformed surface using Digital Image Correlation (DIC), they calculated the strain field. The process of imaging is very time intensive and usually takes about 10 minutes for each scan [56] and is confined to an area of a few microns long. In addition to the time required for each AFM scan, there is also the post-processing time added for DIC. They reported 400 μstrains resolution in their strain measurements for a 512×512 pixel image and 1/8 pixel DIC resolution. However, the main

advantage of this technique is that it provides a whole-field strain data which helped the analysis of the strain field around geometry inclusions and notches [62], as well as cracks. [78,79]. A typical displacement field at the vicinity of a crack in polysilicon that has been measured using AFM/DIC is shown in Figure 2-11.

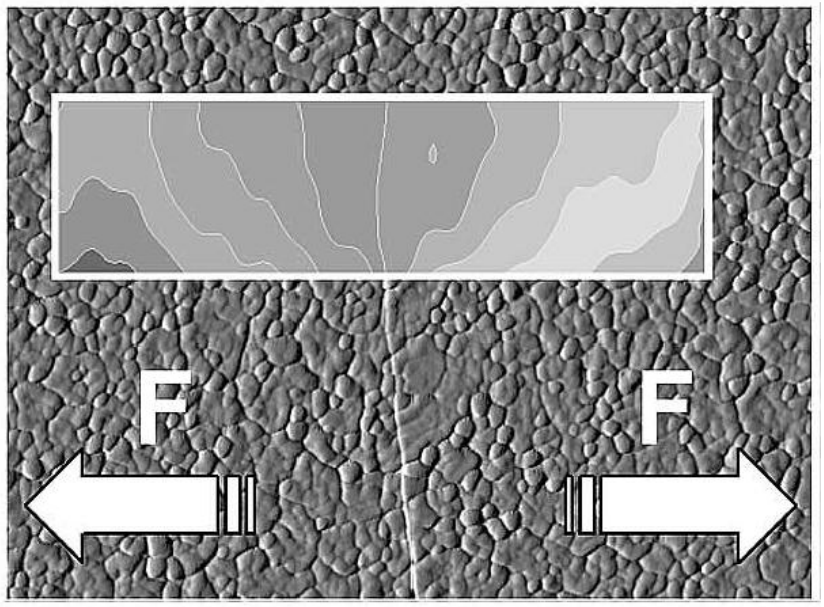

Figure 2-11- Displacement field in the vicinity of a crack in polysilicon film measured by AFM/DIC. [57]

A few researchers used the MEMS based devices that were discussed in section 2.4 to study the mechanical properties of thin films in electron microscopes. If the thin film samples are electron transparent, i.e. have nanometer thickness, *in situ* studies in TEM are also possible which provides more information on the microstructural deformations during loading. Haque and Saif [65-68] used the technique to study the mechanical behavior of Al and Au thin film specimens under SEM and TEM. The resolution of the measured strain and stress depends on the magnification

of the microscope and the size of the specimen. At 100nm microscope resolution, the strain resolution was 0.05% for 200nm thick and 185μm long Al films and was 0.03% for 100nm thick and 275μm long specimens. [66] Rajagopalan *et al* [68] reported lower strain resolutions of 0.005% and 0.01% for Al and Au films, respectively. Although this method of strain measurement has a high resolution and provides extra information on the microstructural deformations, its force and displacement scales are within the limits of nanostructures rather than common thin film materials. A σ-ϵ curve along with respective microstructural observations produced by this method is shown in Figure 2-12.

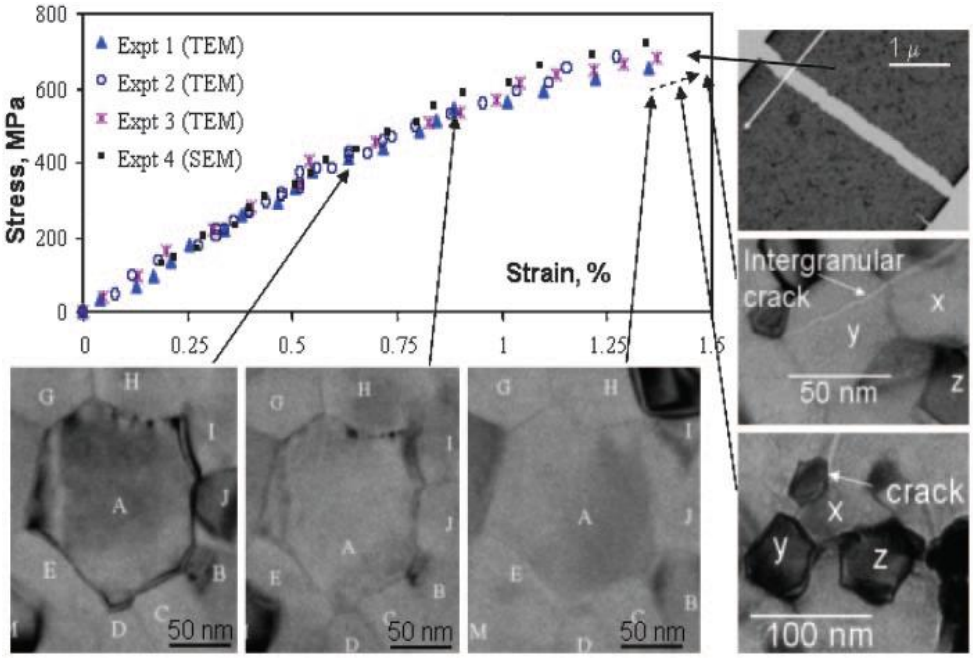

Figure 2-12- *In situ* TEM test results for Al thin film specimens. Microstructural deformations corresponding to the tensile test is also presented. [65]

2.6 Summary

In this chapter, the major research activities that used a tensile testing method to study the mechanical behavior of thin film materials were reviewed. For this purpose, most of the research groups designed and used their custom made test setups. A historical and general overview of these test devices were presented in section 2.1. The tensile testing research was categorized into four major steps, namely sample preparation, gripping, load actuation and measurement, and strain measurement. Each of these steps was discussed in detail in their designated sections.

The information obtain through this review provide a detailed understanding of the challenges involved in tensile testing of thin film materials and different approaches that were used to tackled these issues. The results will help us design and implement a device that can meet these challenges toward a reliable and precise study of the mechanical behavior of thin film materials.

Chapter 3

Experimental Setup

There are many challenges involved in tensile testing of thin film specimens. In this chapter, a novel approach is introduced to tackle these challenges. The design requirements are studied in the four categories, namely sample preparation, gripping, loading, and strain measurement. Various aspects of the design are presented and the elements of the setup are introduced. A novel gripper is designed and fabricated for this application to meet the demanding requirements of gripping a thin film specimen. An interferometry technique has also been developed to measure strain field during the specimen loading. Sample preparation and postprocessing of interferometry data for strain calculation are discussed in more detail in chapters 4 and 5, respectively.

3.1 Design Requirements

The main goal of this thesis was to design and evaluate an experimental technique to study the mechanical behavior of thin film materials in microelectronics and MEMS applications. The ideal information that is usually expected from a device that probes the mechanical behavior of a material is the stress-strain (σ-ϵ) curve that has been measured for different loading conditions, i.e. under monotonic, fatigue, creep, and relaxation loadings. Thin film materials are not excluded from this expectation. This information is vital to scientists and design engineers to design devices that have reliability and mechanical integrity during their life-time.

There had been many different techniques introduced to probe the mechanical behavior of these materials. A brief comparative review of these techniques in section 1.2 showed that tensile testing can be the best choice as an experimental method for this purpose. However, as it was discussed earlier there are many challenging issues that hinder the advantages of this technique over some other techniques. In current thesis these issues are considered and some novel designs are utilized to make use of the tensile testing technique. All of the four categories are separately scrutinized in-detail and depending on the requirements and current state of technology, either a new method is proposed or the past methods are utilized as-is or with minor revisions.

The general requirements for such a tensile testing device are capability of loading thin film specimens in different load conditions, having a μN load resolution, providing sub-nanometer displacement resolution, gripping micro- and nano-scale films, and above all being capable of measuring strains in a very small region.

In contrary to the macro-scale tensile testing devices that a stand-alone testing device is usually purchased and is used to test different materials and geometries, in small scale the scenario is different. The process of designing the test rig and fabricating the sample are not independent and the design of each one should be followed based on the requirements and limitations of the other one. For example, as it was discussed earlier in section 2.2, the sample preparation procedure depends upon the gripping method. On the other hand the sample geometry is to be chosen such that the stresses and strains that are induced during loading are within the resolution of the current load cell and actuation technology.

In the following sections, different parts of the device are introduced and based on the conclusions made from Chapter 2, every single aspect of the design are scrutinized in detail and novel approaches are proposed.

3.2 Loading Setup

The loading subsystem is the part of the device that induces a known state of stress in the specimen under study. As shown in Figure 3-1, it consists of three main parts: the gripper, the load cell, and the actuator. The load-train is closed by mounting the specimen in the grippers. In order to be able to study the monotonic, fatigue, creep, and relaxation behavior of the material, the loading subsystem should be able to provide stress controlled or strain controlled monotonic and cyclic waveforms.

Based on these design criteria, each part is designed and discussed in the following sections.

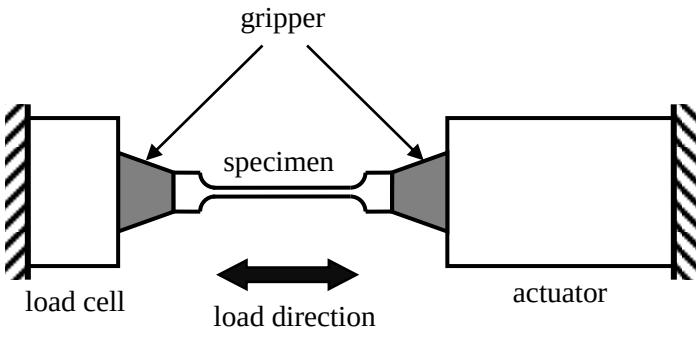

Figure 3-1- Schematic representation of the loading subsystem.

3.2.1 Gripper

The gripper is the part of the device that connects the specimen to the loading system and allows the reliable application of load. It should provide a no-slip condition when specimen is monotonically or cyclically loaded; it should be stiffer than the specimen itself; it should maintain a desirable out-of-plane alignment; and more importantly should not result in stress concentration at the mounting point. Meeting all these requirements for a thin film specimen that is only a few hundred nanometers to a few microns thick is very challenging. The gripping techniques that were discussed in section 2.3 were developed to meet some of these requirements. However, they all have their own limitations; electrostatic gripping is only applicable for static low load applications. The combined UV adhesive/electrostatic gripping, though reliable for static long time tests, does not work in high cycle fatigue tests due to the degradation

of the adhesive layer (debonding) under cyclic loads. The method of sandwiching the grip ends of the specimen between thin foils seems to induce stress concentrations and local warpage at the grip area. The window frame approach, in fact, provides a reliable gripping during tensile loading. Therefore, initially it was chosen as the method to follow in this work. Albeit, due in part to the fabrication complexities, this method was soon abandoned. Therefore, a novel gripper was designed to address the demanding design criteria for gripping a thin film specimen.

The original idea of the new gripper design was borrowed from the grippers that have been used in macro-scale tensile testing devices for decades. As shown in Figure 3-2 , in this scale of tensile testing, specimen's end grip is mounted between the two serrated jaws of a gripper and is then loaded. However, when the specimen is a thin film material, this approach is so challenging that many researchers abandoned this technique and used gripping methods that have been already reviewed in section 2.3. In this thesis, however, this approach was re-investigated and a gripper was developed on that basis.

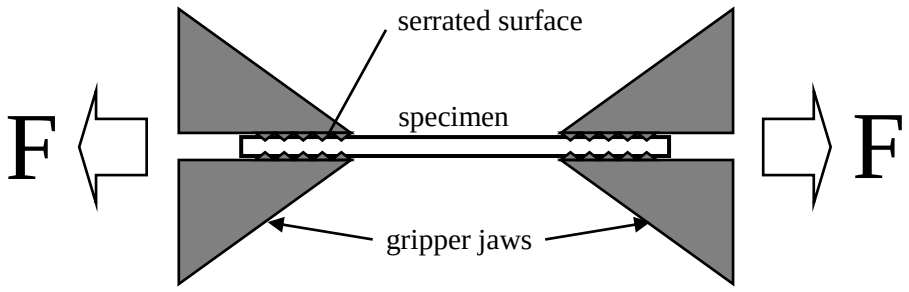

Figure 3-2- Schematic representation of the the gripper with serrated jaws.

Thin film specimens are fabricated on a thick, relatively rigid substrate and are usually anchored to this substrate at one end, as schematically shown in Figure 3-3. Since the adhesion of the film to the substrate at the anchor is high, the specimen can be mounted in the gripper through the substrate at the anchor side. The challenge is the other side of the gripper that requires gripping a very thin specimen.

Figure 3-3- Micro fabricated thin film specimen anchored on the substrated.

The thickness of thin film specimens is in the order of the fabrication tolerances for machined parts. Therefore, when they are mounted in a gripper that is macro-machined, they may not be reliably gripped across the grip area. Hence, when loaded, they slip at the gripper jaws. In order to overcome this issue a double action gripper is designed. As shown in Figure 3-4, due to the rotation of the arm at pivot, when the grip is closed it both pushes the specimen up and pulls it back to make sure that the specimen is well gripped. A fine stage and a coarse stage are used to properly move the gripper. Both stages utilize 200μm pitch adjustable screws (Thorlabs Inc., NJ) and provide 2μm positioning accuracy. In order to be able to grip the top and bottom of the specimen, part of the substrate at the grip end should be cut away to provide space for the attachment of the gripper jaw to specimen.

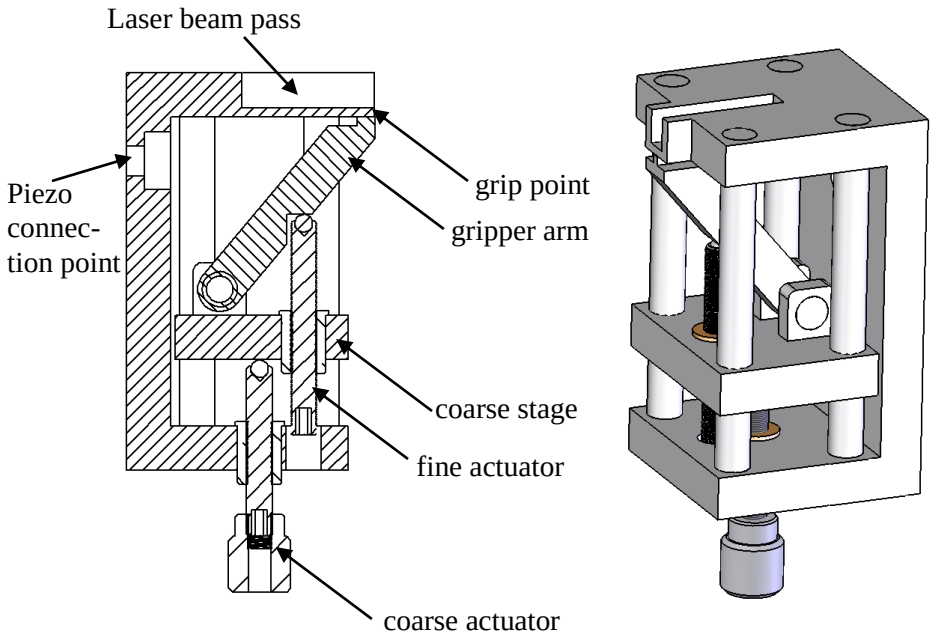

Figure 3-4- The proposed double action gripper.

In order to cut the substrate, the best way was to dice the substrate from back-side using a dicing saw as shown in Figure 3-5. The substrate is mounted from the backside on a holder and is then cut through a slot in the holder using a dicing wheel. However, the dicing machine at G2N lab was designed to work at ~30,000 rpm and hence was being cooled by the flow of a coolant. Since, at this time, the specimens are released and are free-standing, the coolant will damage the film. On the other, the wheel speed was so fast that any interference between the wheel and holder slot side walls will result in wheel damage. Therefore, a low speed dicing machine was designed and fabricated to provide the capability of cutting the backside of the substrate. The dicing machine was designed for a working speed of 200 rpm. A 3" Isomet diamond wafering blade (Buehler Canada Ltd., ON) was used for cutting the substrate.

The specimen was mounted on a precision XYZ stage and the thickness feed was monitored by a digital LVDT indicator (Mitutoyo Corp., ON) with 5 microns displacement accuracy. The low speed dicing machine is shown in Figure 3-6. Substrate is mounted on the holder surface using Kapton® tape. In the very first tries, it was found out that a cutting depth of about half the thickness of the substrate is enough and after that the substrate can be easily broken by hand. The yield of the cutting was low at the beginning. However, it was improved with gaining more expertise and the failure rate is now below 5%.

The final gripper-specimen arrangement is schematically shown in Figure 3-7.

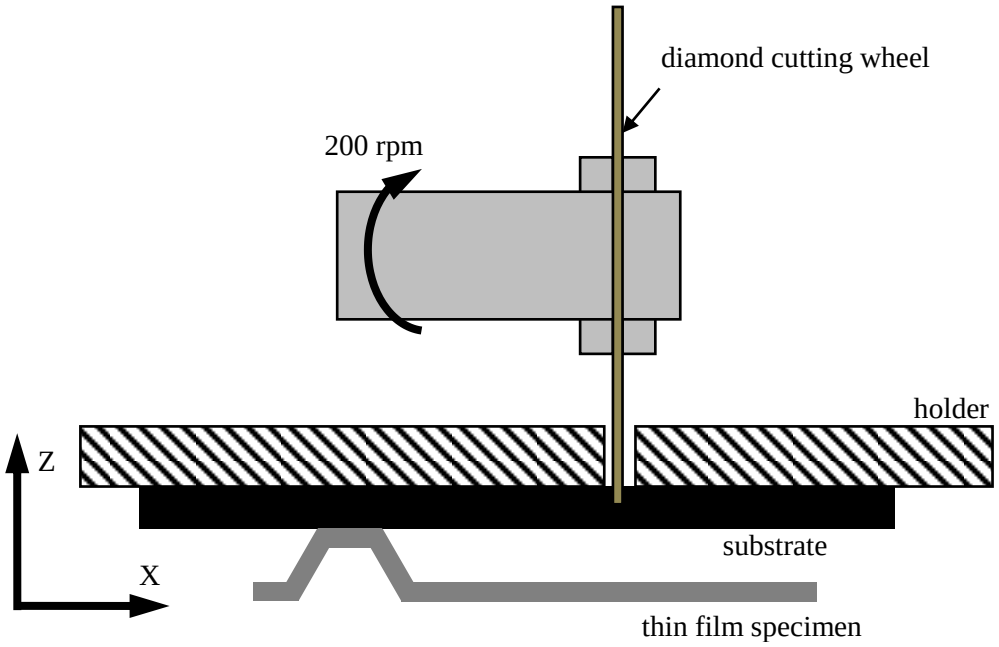

Figure 3-5- Schematic representation of the substrate cutting from the backside.

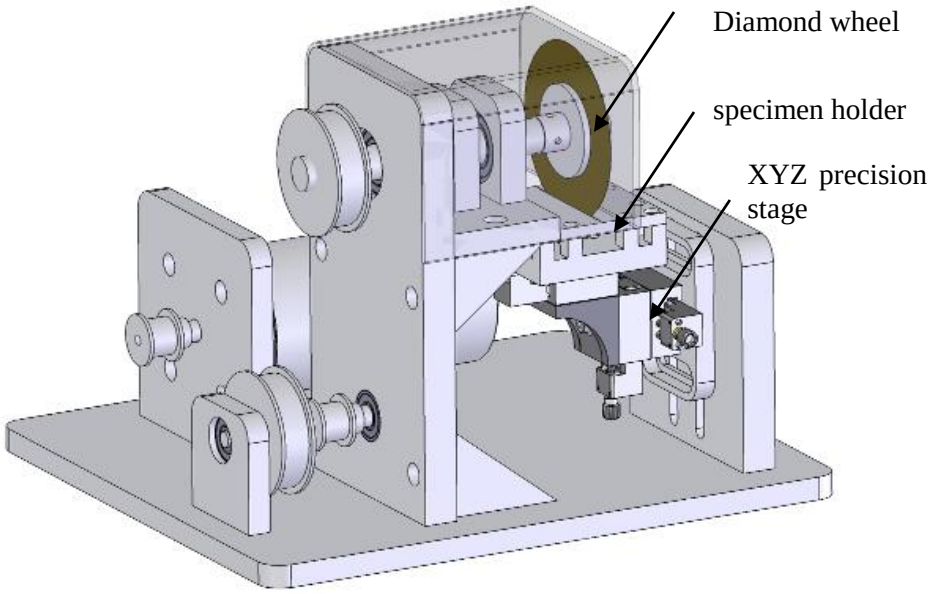

Figure 3-6- The low speed dicer that was designed and fabricated to cut the substrate at grip end.

In order to align the specimen and gripper, past researchers have used optical microscope to monitor the specimen-gripper side view. In this research, however, a technique based on electrical resistance is used. A precision digital multi-meter (Fluke Corp., WA) is used to monitor the resistivity between the specimen and the gripper. As soon as the gripper jaw touches the specimen surface the electrical resistance drops from an open circuit value to a very low value, indicating that they are in contact. At that position the other gripper jaw is tightened and the specimen is ready for loading.

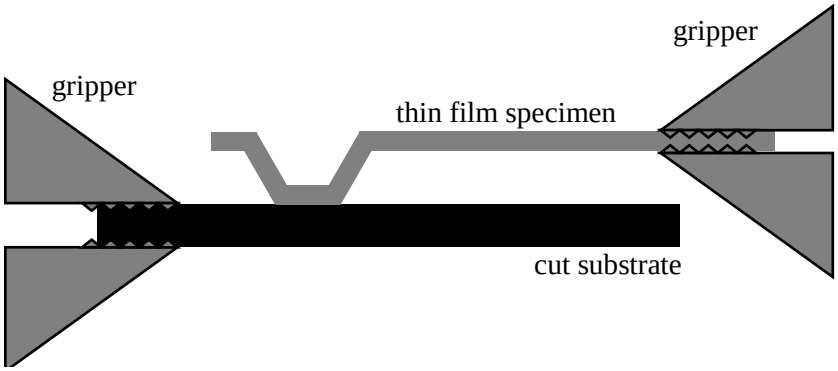

Figure 3-7- The final gripper-specimen arrangement.

The misalignment in gripper causes a bending in the specimen gage section resulting in an inhomogeneous stress in the gage section. The effect of misalignment on the level of stress is studied by finite element method using ANSYS based on the specimen material properties and geometries discussed in section 4.1. The results are shown in Figure 3-8. Based on this simulation, an out-of-plane misalignment of 30μm seems to be an acceptable value resulting in maximum of 2 MPa Mises stress.

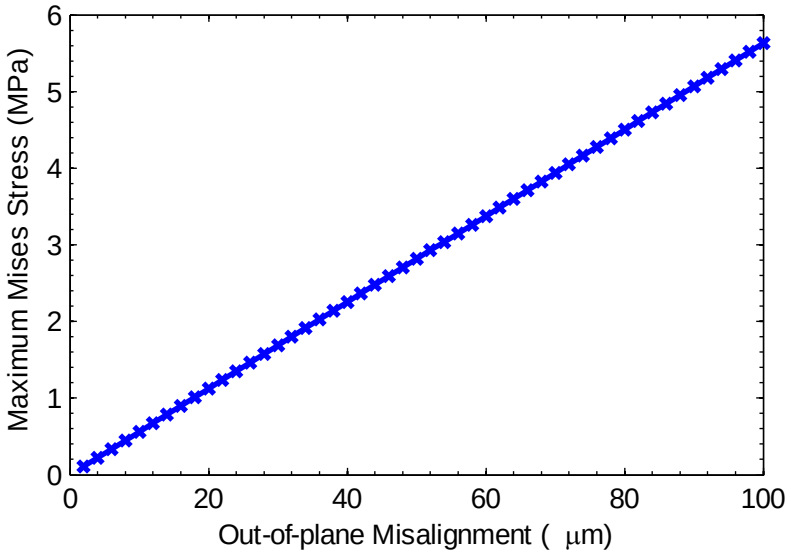

Figure 3-8- Effect of out-of-plane gripper misalignment on maximum Mises stress at gage section.

3.2.2 Piezo Actuator

As it was discussed earlier in this chapter, the loading system had to provide high resolution monotonic and cyclic loadings. Among the actuators that could be used for this purpose, piezo actuators fulfill all of these requirements. The specific choice of piezo actuator depends on the displacement amplitude and resolution, natural frequency, and the maximum load capacity. For this application a low voltage PZT (LVPZT) actuator, P-841.10, (Physik Instrumente (PI) L.P., MA) was used. The actuator is preloaded to provide tensile forces of up to 50 N and provides a 30μm displacement.

Piezo actuators, by themselves, have infinite displacement resolution; however, their resolution is limited by the electrical noise at the amplifier circuitry and the drift and hysteresis in the material. In order to provide high resolution positioning accuracy, a high precision low noise LVPZT amplifier module, E-503, (Physik Instrumente (PI) L.P., MA) was used. The drive voltage is controlled by a -2 to 12 V BNC input. A ten-turn DC bias potentiometer can be used to add a DC bias to the input. The drift and hysteresis was compensated by a servo control module platform, E-509.S3, (Physik Instrumente (PI) L.P., MA) that controls the actuator displacement through a strain gage feedback mounted on the piezo stack. The actuator control voltage is provided by a control signal that will be discussed in section 3.4. The piezo drive module is mounted in a 9.5" chassis with E-530 precision power supply and can drive up to three independent LVPZT actuators.

3.2.3 Load Cell

In order to measure the applied load and hence the stress at gage section of the specimen, a strain gage load cell was used. The load cell is a high precision low load sensor, GSO-10 provided by Transducers Techniques Inc., CA. It has maximum load capacity of 100mN and provides 100μN resolution. Load cell excitation and signal conditioning is provided by TMO-2 conditioner (Transducers Techniques Inc, CA). The load cell and conditioner setup can be calibrated against a pre-calibrated 87.325kΩ shunt resistor. The load cell has a 1mV/V output per excitation voltage. Before each measurement the load cell setup is calibrated for rated output of 8 volts by adjusting the gain and zero balance potentiometers.

Since the load cell capacity is very low and has a threshold of 150% of full-scale range, i.e. 15mN, a load cell mount is designed to secure the load cell's sensing end when mounting the specimen. For this purpose two dwell pins are inserted in a toleranced hole in the mount and the load cell. The pins are removed when loading the specimen.

Typically, the load cell has a voltage drift over time. For long term relaxation and creep tests, load cell drift has to be corrected based on the load level that is used during the test. For load cell calibration, we relied on the certificate of calibration provided by the manufacturer. For reliable measurements, it is necessary to frequently re-calibrate the load cell against a known load. This can be done at vendor's facility or by our lab.

Another important parameter that affects the load readings is temperature fluctuations. The output voltage of the chosen load cell has a temperature sensitivity of 0.005% of the load per ºF. This error is more effective at lower load values. The temperature fluctuation also affects the zero balance of the load cell by the rate of 5μN/ºF. Temperature fluctuations are usually very small for short time test; however, for the case of long lasting fatigue tests, i.e. more than 24 hours, a thermal isolation enclosure might be required for the setup. The thermal fluctuation of the lab area was measured using a Fluke thermometer. The temperature fluctuations were well below 1ºF over an hour which makes the thermal drift negligible.

The final loading setup is shown in Figure 3-9.

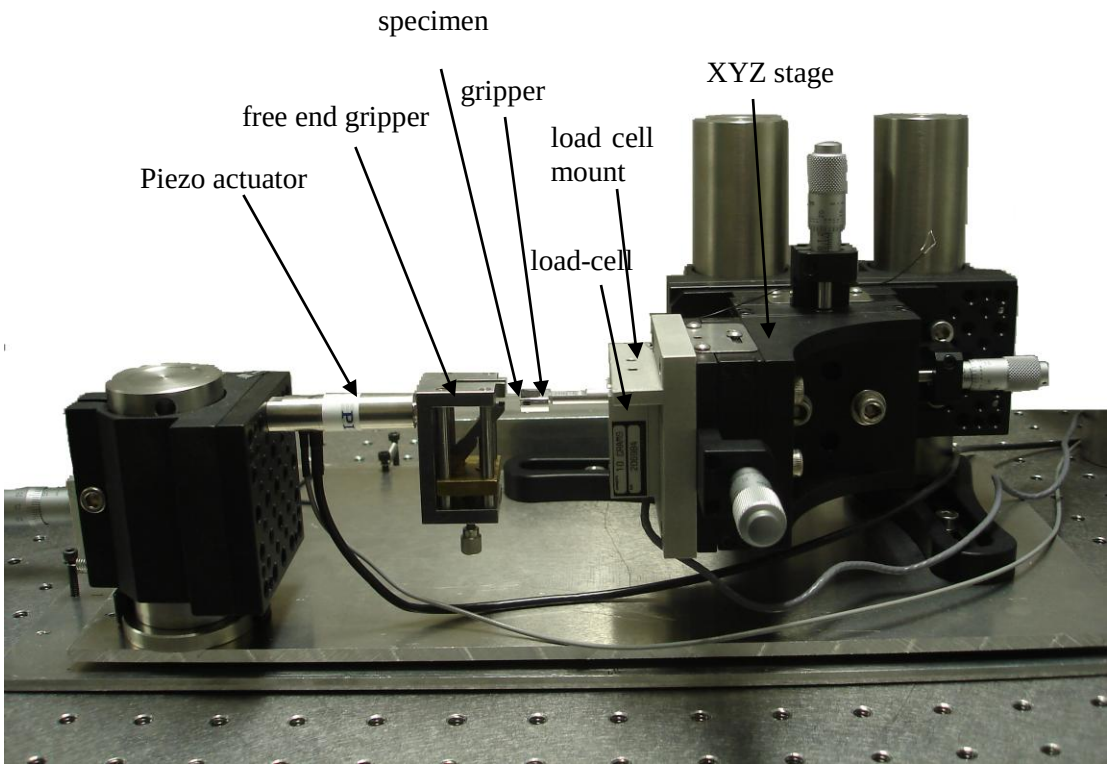

Figure 3-9- Elements of the loading setup.

3.3 Strain Measurement Setup

In order to study the mechanical behavior of a material, the corresponding strains and stresses are to be measured. In the previous section, the loading subsystem and the stress measurement setup were presented. In this section the measurement technique for the other important parameter, i.e. strain will be discussed.

The small scale of the thin film materials makes the strain measurement procedure difficult and challenging. In section 2.5, different techniques for the measurement of strain in thin film materials under tensile loading were reviewed and pros and cons of each were discussed. Based on that discussion the criteria for an efficient strain measurement technique can be categorized as follows; the technique should work in a non-contact mode; it should provide high resolution strain values; it should be capable of measuring strains in static and dynamic monotonic loadings; and it should be simple and easy to implement for scientific and applied applications. Another criterion that was considered as a merit for choosing a technique was the ability to measure in-plane strain field rather just one strain value across the gage length. This criterion is of importance when studying non-uniform geometries and device level measurements. In contrary to stress that is a non-measureable quantity unless for specific simple cases, strain can be measured across a domain. For example, for the case of an actuator arm, the stresses induced in the structure cannot be measured directly; however, the strain field over the arm area is measurable. The ability of strain field measurement is vital when studying thin film specimens with geo-

metric or material non-uniformities or to study the mechanical behavior of components as in the case of device level mechanical reliability tests.

In order to choose a suitable strain measurement technique, alternative techniques were evaluated against the above-mentioned criteria; the AFM/DIC technique though provides high resolution strain field measurement, is a very slow technique and is not suitable to dynamic measurements. On the other hand, the field is usually limited to 10μm×10μm area. ISDG is a versatile tool for strain measurement. It provides accurate strain data and is fast enough for dynamic tests. However, it has limitation on the size of gage section and requires at least 300μm gage length. On the other hand, it does not provide strain field. Imaging techniques, as discussed earlier are limited in resolution. *In situ* SEM and TEM studies provide a detail insight into the material behavior at microstructure level. However, they are too complex for routine applied material behavior studies. The speckle interferometry technique is a very useful tool and can provide strain field data. However, historically due to the low signal to noise ratio levels in this technique it was not so popular among researchers.

In order to choose a suitable strain measurement technique to meet the criteria discussed earlier, almost all of the non-contact strain measurement techniques were reviewed, with an emphasis on interferometry based methods. In the end, moiré interferometry was chosen as the method to be used in this research. This method is discussed in detail in the following sections and was implemented to measure strains in thin film materials. The advantages and disadvantages of the technique is also discussed and compared to the previous strain measurement methods.

3.3.1 Moiré Interferometry

Moiré is an optical phenomenon and is defined as the interference pattern that is caused by overlaying two periodic arrays of lines or dots with slightly different period, rotated axis, or pattern shape. In other words, moiré is the fringe that is observed by looking at a pattern through another pattern. The fringes created as such are not the same as the original one but contain adequate information that, with a few known parameters, the original pattern can be reconstructed from. The phenomenon was introduced in 1874 by Rayleigh [80]; however, it was never fully analyzed until the recent works of Guild [81] in the 1950s. He showed that moiré fringes are the result of optical diffractions followed by a filtering of high frequency information. As shown in Figure 3-10, by looking at pattern B through pattern A, moiré fringes can be visualized. Figure 3-10-a shows the moiré fringes that are caused by a slight difference in the pitch of the two patterns. In Figure 3-10-b, the two patterns have a rigid body rotation and in Figure 3-10-c, they have different patterns. The sensitivity of this phenomenon to the relative in-plane changes of the two patterns was the base of the application of moiré in strain measurement. In the context of moiré, these patterns are called grid or more often grating.

For simplicity, let's consider the case of gratings of different pitch, as shown in Figure 3-10-a. Moreover, let's assume that grating B is the specimen grating fabricated on a tensile specimen and had the same pitch as the reference grating A.

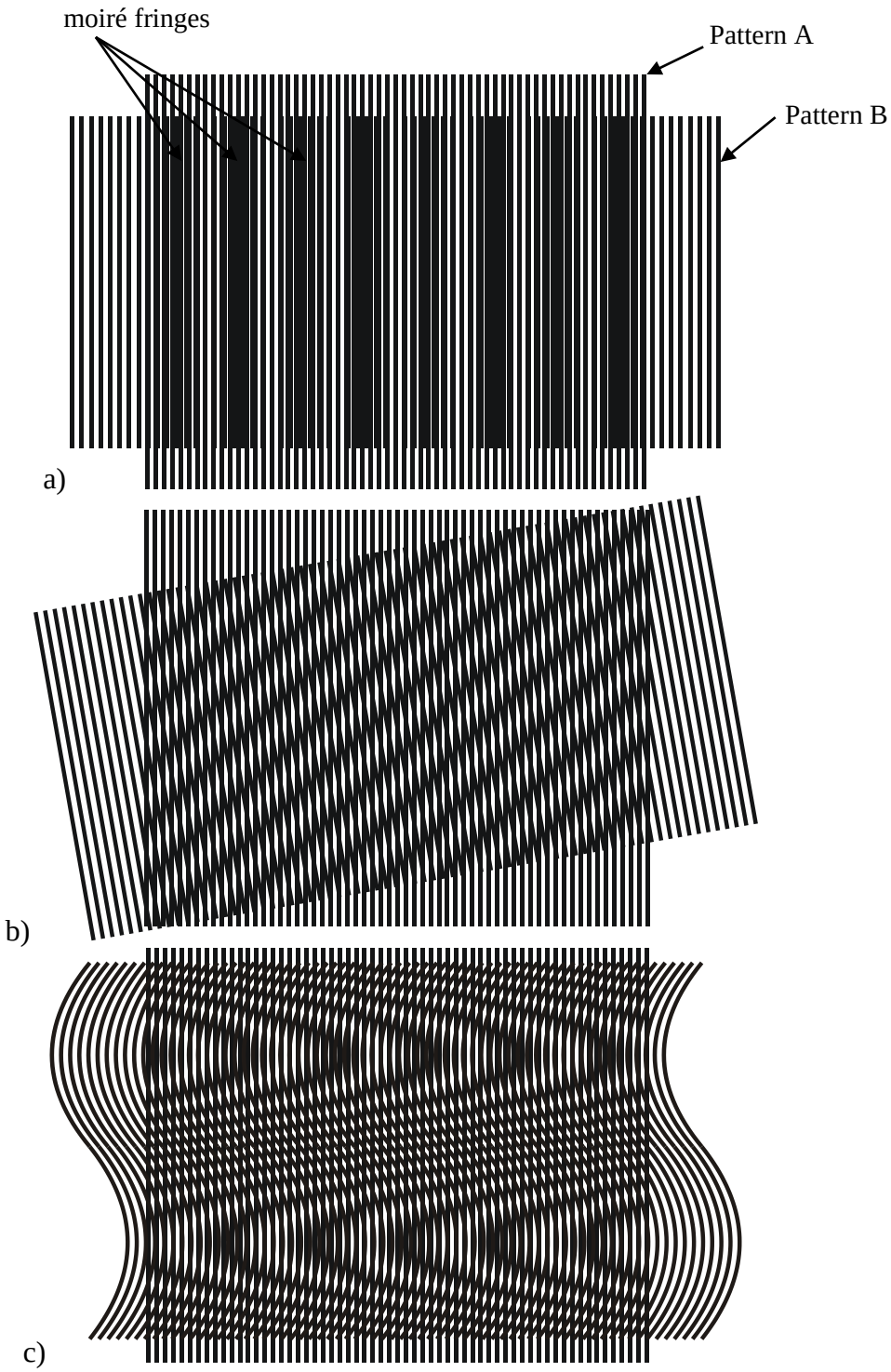

Figure 3-10- Moiré effect by the overlay of two patterns with different pitches (a), different angles (b), and deformed patterns (c).

If the specimen is loaded perpendicular to the axis of the specimen grating, the induced deformations result in a variation to the pitch of the specimen grating. If the deformed specimen grating is observed through the reference grating, moiré fringes will be formed. The relationship [83]

$$N_x = \frac{U_x}{p} \tag{3-1}$$

is the basic relation that correlates the observed moiré fringes to the actual deformation field in the specimen. In this relationship, N_x is the integer fringe number, U_x is the displacement and p is the pitch of the reference grating. In other words, each fringe is the line that is constructed from the iso-displacement points on the specimen. It can be clearly seen that the displacement measured through equation (3-1) is a multiple of the pitch of the reference grating. This important relationship shows that the sensitivity of the method is highly dependent on the pitch of the reference grating; i.e. the smaller the reference grating's pitch, the higher the resolution of the measurements.

The displacement field measured through relation (3-1) is correlated to infinitesimal strains by

$$\epsilon_{xx} = \frac{\partial U_x}{\partial x} \tag{3-2}$$

From equations (3-1) and (3-2), for any consecutive fringe number, the strain value is obtained by

$$\epsilon_{xx} = p \times \frac{1}{\Delta x} \quad \textbf{(3-3)}$$

where Δx is the distance between the two consecutive fringes. This relation is of interest in that it shows the main difference between the common resistive strain gages and the moiré method, if moiré is evaluated by equation (3-1). In fact, in this approach, moiré is a set of strain gages with constant displacement and variable gage lengths in contrary to the variable displacement and constant gage length of resistive strain gages or extensometers. This classic discrete treatment of moiré shows that higher strains, i.e. higher fringe frequencies, have higher spatial localization. However, in a whole-field strain measurement experiment, the strain values in certain spatial coordinates are sought, regardless of the strain magnitude. Therefore, other approaches should be utilized to evaluate moiré fringes obtained from the measurements.

The approach discussed above was historically the base of many strain measurement experiments that utilized the moiré phenomenon. This approach which was later named "Geometric Moiré" was unable to meet challenging requirements for both spatial accuracy and strain precision. The fabrication of high frequency specimen and reference gratings was too complex and, even if they were fabricated, their resolution was limited by diffraction effects and alignment issues. [82]

Moiré Interferometry, on the other hand, can meet many of these requirements. All aspects of this method have been discussed in detail in the literature. [83-86] However, a brief review of the method and its formulation will be presented here for future references throughout the thesis.

Moiré interferometry is based on the diffraction and the consequent interference of two coherent beams of light. As shown in Figure 3-11 , when a parallel beam of light is incident at an angle α to a phase grating[1], it is diffracted in many preferred directions, referred to as diffraction orders. The diffraction pattern is governed by the diffraction equation,

$$\sin\beta_m = \sin\alpha + m\lambda f_s \qquad \textbf{(3-4)}$$

where m is the diffraction order, β_m is the angle of the m^{th} diffraction order, λ is the wavelength of the incident beam, and f_s is the grating frequency. Light is diffracted into these preferred directions, with very small-intensity light emerging in other directions. For a monochrome incident beam, the angular spread of each diffraction order is sufficiently narrow. The intensity of the diffracted beams decreases as

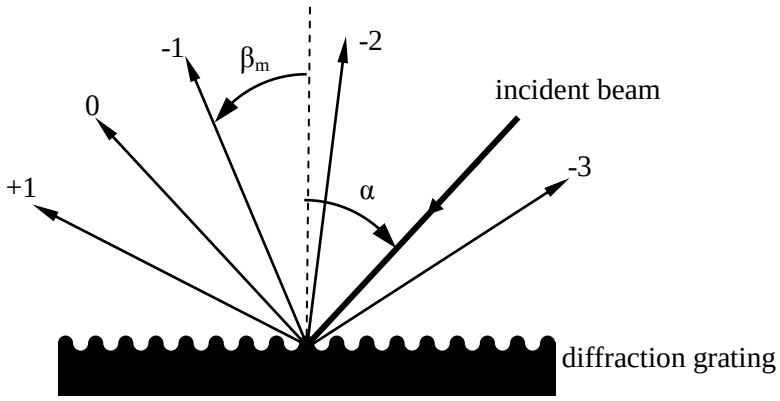

Figure 3-11- Diffraction of an incident beam and the respective diffraction orders.

[1] A phase grating is the type of grating that has a corrugated surface and modulates the frequency of the incident beam. Phase gratings, in contrary to amplitude gratings that consist of opaque bars and transparent spaces, result in extensive diffraction of light.

the diffraction order is increased.

When a coherent beam with planar wavefront, ω, is incident at a conductive diffraction grating, the emerging diffraction patterns may have planar or warped wavefronts. Assuming that the incident beam is in an angle such that the first diffraction order emerges perpendicular to the grating plane, i.e. $\sin\beta_{-1} = 0$, from equation (3-4), the angle of incident beam should be

$$\alpha = \sin^{-1}(\lambda f_s) \quad \textbf{(3-5)}$$

Under these optical conditions, the wavefront of the emerging beam will remain planar, as shown by wavefront ω' in Figure 3-12. If the specimen is deformed, i.e. the frequency of specimen grating, f_s, changes, from equation (3-4), the angle of diffracted beam will be changed. If the deformation is linear and uniform, it can be assumed that the beam is still perpendicular to the grating surface, but has a rotated planar wavefront, as shown by wavefront ω'' in Figure 3-12. This wavefront is perpendicular to the direction of the designated diffraction order in the angle of β_m. However, if the deformation is non-uniform, the changes in diffraction grating spacing result in a warped wavefront, ω'''. Therefore, the wavefront of the diffracted beam, or in other words the phase of individual waves, contains information from the deformation field of the specimen grating, which can be used as a means of strain measurement.

Detecting the phase of an electromagnetic wave that, in the case of visible light, is oscillating at THz frequencies is experimentally impractical. In order to

detect these phase fluctuations, the superposition of two coherent waves has been used for decades. In this technique which is known as interferometry, the interference of the two high frequency waves results in a fringe pattern (interferogram) that is modulated at a lower frequency. This concept is schematically represented in Figure 3-13. Beam 1 and beam 2 are incident at the specimen grating and the superposition of the diffracted beams resulted in an interference pattern that is detected by a camera. As it will be shown later in this thesis, the instantaneous frequency of the pattern is a function the local phase changes in the emerging diffraction orders.

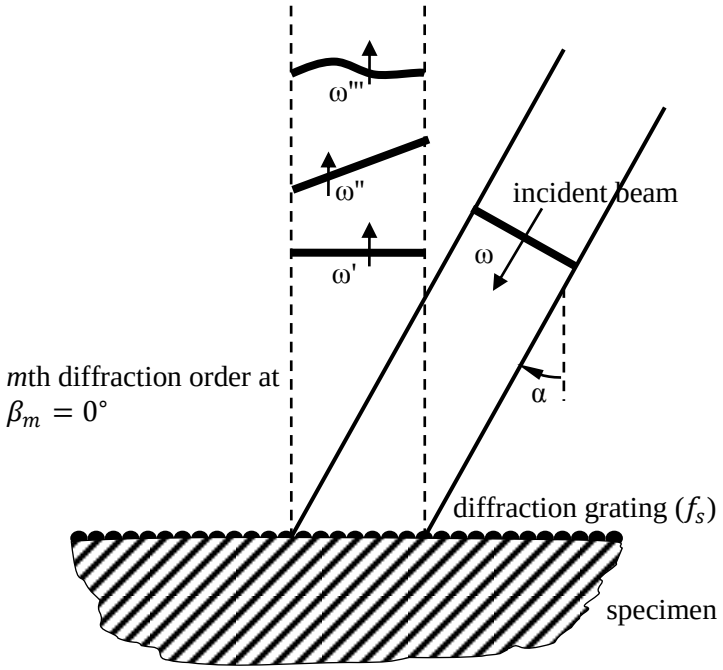

Figure 3-12- Diffraction of an incident beam and the effect of specimen deformation at the difraction grating on the wavefront of the emerging beam.

There have been many different approaches to correlate the observed interferogram to the actual deformation in the specimen grating and all of them result in the same correlation. Approaches based on geometric moiré analogy [84], light obstruction and the bar-and-space concept [82], and those based on the phasor treatment of the diffraction phenomena [83,87] were among the well-known methods that have been used for this correlation.

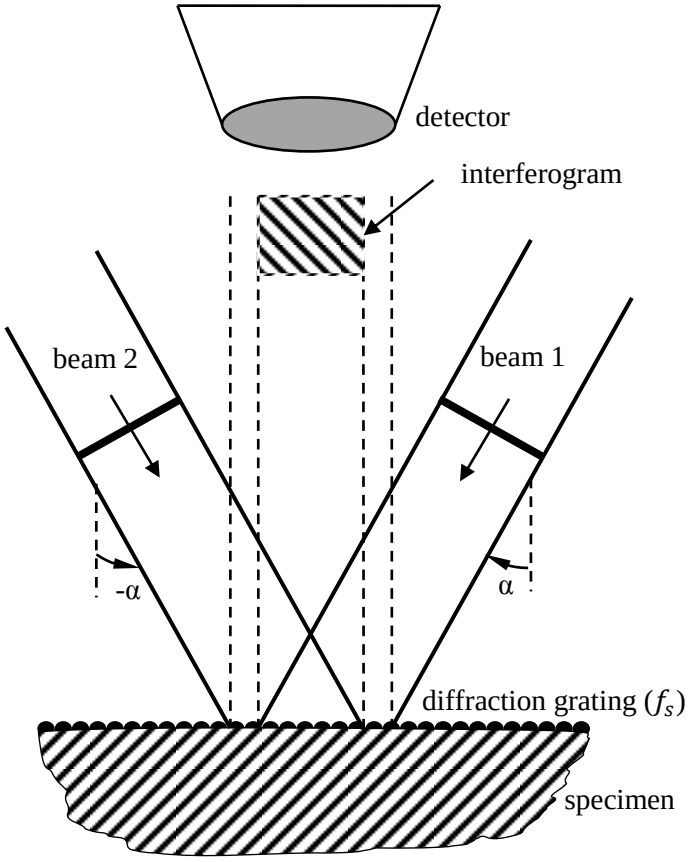

Figure 3-13- Interference of two beams incident at a diffraction grating.

In an analogy to the geometric moiré that was discussed earlier in this section, the phenomenon can be explained by assuming a virtual grating as the reference grating used in geometric moiré. This virtual grating is, in fact, the interference pattern of the two incident beams in the vicinity of the diffraction surface. The interferogram that is detected can be considered as the fringe pattern that is visualized by looking at the specimen grating through the virtual reference grating. The frequency of the virtual grating created as such is two time the frequency of specimen grating and provides a factor of two in fringe multiplication. This approach which was very popular in the early literature of moiré interferometry can completely correlate the moiré patterns to deformation field using the geometric moiré formulations developed earlier; however, this approach is only an analogy in that if the planes of the polarization of the two incident beams were perpendicular to each other, the two beams will not necessarily interfere and such virtual grating will not be formed.

In the present work, the phasor treatment of interference fringes was used due to the usefulness of the information that is provided by this approach. This approach has been rigorously discussed in [83] and [87]. Therefore, only a brief discussion and the necessary formulation will be provided here.

As it was discussed earlier, when there is no deformation in the specimen grating, the diffracted beam has a plane wavefront. From the general wave equation, the emergent wavefronts can be expressed by

$$A_1(x,y,z,t) = a_1 \exp(i[2\pi vt + \psi_1(x,y,z)])$$
$$A_2(x,y,z,t) = a_2 \exp(i[2\pi vt + \psi_2(x,y,z)]) \quad \textbf{(3-6)}$$

where A is the complex amplitude, a is the amplitude, v is the frequency, t is time, and ψ is the phase of the emerging wave. Since temporal variations do not affect the phase of the propagated wave, equation (3-6) is simplified to

$$A_1(x,y,z) = a_1 \exp(i[\psi_1(x,y,z)])$$
$$A_2(x,y,z) = a_2 \exp(i[\psi_2(x,y,z)]) \quad \textbf{(3-7)}$$

When the specimen is deformed, the optical path length of the emergent beam changes and results in variations in the phase of the propagated waves. Assuming a general deformation of $U(x,y)$ and $W(x,y)$, where $U(x,y)$ is the in-plane deformation perpendicular to the grating axis and $W(x,y)$ is the out-of-plane deformation, the resultant phase change in the two emerging beams is

$$\psi_1(x,y) = \frac{2\pi}{\lambda}[-W(x,y)(1+\cos\alpha) + U(x,y)\sin\alpha]$$
$$\psi_2(x,y) = \frac{2\pi}{\lambda}[-W(x,y)(1+\sin\alpha) - U(x,y)\sin\alpha] \quad \textbf{(3-8)}$$

The resultant fringe pattern that is formed by the interference of the two diffracted beams at the image plane has the form of

$$\begin{aligned} I(x,y) &= (A_1(x,y) + A_2(x,y))(A_1(x,y) + A_2(x,y))^* \\ &= a_1^2 + a_2^2 + 2a_1a_2\cos(\psi_2(x,y) - \psi_1(x,y)) \\ &= I_0(x,y) + \gamma(x,y)\cos(2\frac{2\pi}{\lambda}U(x,y)\sin\alpha) \end{aligned} \quad \textbf{(3-9)}$$

where * denotes the conjugate, and $I_0(x,y)$ and $\gamma(x,y)$ are the background intensity and fringe visibility, respectively. This equation also shows the advantage of moiré interferometry in that it is insensitive to out-of-plane deformations, $W(x,y)$.With the assumption of equation (3-5), this equation is simplified to

$$I(x,y) = I_0(x,y) + \gamma(x,y)\cos(2\pi(2f_s)U(x,y)) \quad \textbf{(3-10)}$$

In the past, this equation was used only on the points with maximum intensity, i.e. fringe lines. The result of this approach is

$$N_x(x,y) = \frac{U(x,y)}{2f_s} \quad \textbf{(3-11)}$$

which is, in fact, the general moiré relation of equation (3-1) with fringe multiplication factor of two. This equation shows why moiré interferometry has been treated as the analogy to the geometric moiré for decades. However, in this approach most of the information provided in the interferogram is neglected due to the fact that the equation is only evaluated at points of maximum intensity. Since displacement is evaluated in specific points of constant displacement, this approach suffers from lack of spatial resolution, i.e. the calculated strain is an average of strain in a distance, Δx. As it was discussed earlier, this approach will treat the moiré fringes a set of strain gages with constant displacement and variable gage length.

However, as it is shown in equation (3-10), the displacement information of any point at coordinate *(x,y)* is included in the phase of the interferogram. Therefore, by unwrapping the phase of the recorded interferogram, one can fully calculate the

displacement field across the specimen. This will result in a displacement field with high spatial resolution limited by the magnification and pixel size of the detector. The methods and approaches that can be utilized to extract the phase and correlate it to the strain field will be discussed in detail in Chapter 5.

In the following sections, the implementation of moiré interferometry to measure strain and displacement field in tensile specimens will be discussed.

3.3.2 Optical Setup

In order to implement the moiré interferometry concept for the measurement of strain, an optical setup was designed and evaluated. The optical setup is schematically shown in Figure 3-14. A polarized HeNe laser (Thorlabs Inc., NJ) is used as the light source. The laser beam diameter is 0.8 mm and provides 2mW power at 632.8nm wavelength. The beam intensity is controlled by a neutral density filter. Usually lower intensity is used during beam alignment and higher intensities are used during the actual measurements. Higher laser source intensities provide higher counts at CCD and increase the signal to noise ratio.

Since the moiré interferometry is a two-beam interferometer, the laser source is divided into two coherent beam arms via a pellicle beamsplitter. Due to their relatively thin thickness, the application of this type of beamsplitters introduces less wavefront error and reduces ghosting effects compared to the common beamsplitter cubes.

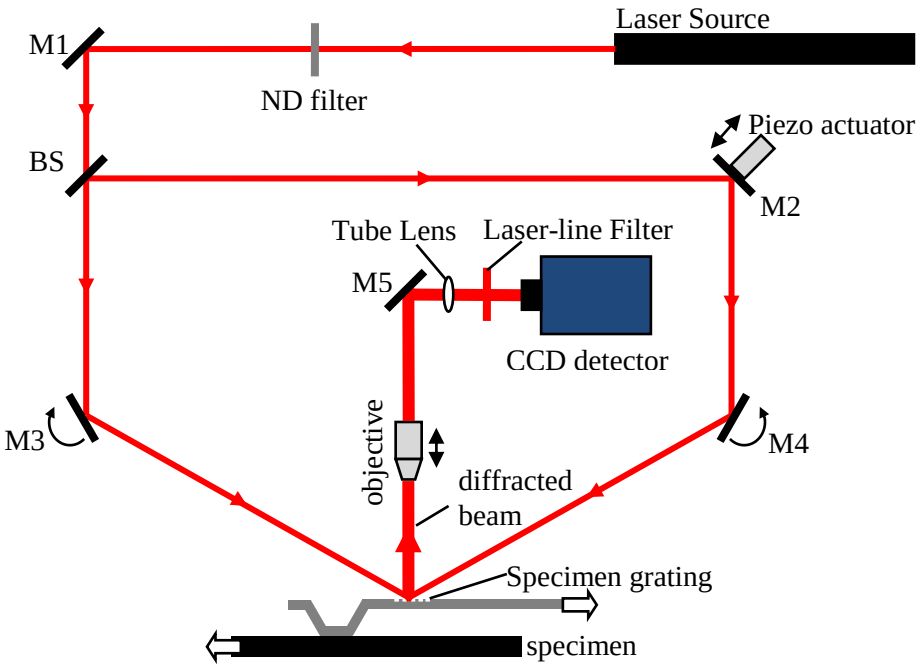

Figure 3-14- Schematic representation of the optical setup for moire interferometry.

The two beams are directed to the specimen grating via two prism mirrors mounted on a precision rotation stage. The rotation stage provides 360º coarse rotations with ±7º micrometer driven fine rotation with 0.1º resolution. This part of the setup adjusts the angle of the incident beam, α as shown in Figure 3-11. When the beam is incident at the specimen surface with diffraction gratings on it, diffraction orders emerge as discussed in section 3.3.1. This setup is designed such that the first order diffraction beams emerge perpendicular to the grating plane. The diffracted beam is collected by a 20X Nikon CFI60 infinity-corrected objective. This objective provides high working distance of 13 mm with numerical aperture of 0.4. The objective is chosen based on its ability to provide the combination of the highest numerical

aperture and longest working distance. It also has the minimum chromatic aberration possible. On the other hand, the 200mm tube length provides the easy installation of optical elements between the objective and the tube lens. The objective is mounted on a precision translation stage with micro-meter accuracy to provide precise focusing of the interference fringes on the CCD image plane.

The interferogram is detected by CoolSNAP HQ2 CCD camera (Roper Scientific Inc.). This high-end interline CCD camera is a high resolution cooled camera that provides low dark current and CCD readout noise. It has 1392×1040 imaging array with 6.45μm×6.45μm pixel size. It provides a quantum efficiency of above 60% for the working light source of 632nm. The 14-bit 20 MHz A/D converter on this camera provides a precise digital output which is transferred to computer via IEEE-1394 connection. In order to reduce the dark current of the camera, the CCD is thermoelectrically cooled to -30ºC. The heat generated from thermoelectric cooling is dissipated via forced convection by a fan mounted on the camera. This fan causes an excessive vibration on the optical setup. Therefore, the thermoelectric cooler is turned off during interferometry measurements and the camera is used at room temperature. The effect of dark current is minimized by using shorter exposure times and higher light intensity. At full frame, the frame rate of the camera is 11 fps. However, for our application only a part of the CCD array was used which by choosing a specific region-of-interest the amount of transferred data was reduced and the frame rate was increased to above 40 fps which makes it good choice for dynamic strain measurement applications. The camera is triggered by an external trigger and the image is

captured by LabVIEW® and a specific driver which will be discussed in detail in section 3.4. In order to reduce the amount of ambient light that reaches the CCD detector a narrow band laser line filter is mounted at the aperture of the CCD camera. The filter is technically a band-pass filter with central frequency of 632.8nm and FWHM[1] of ±3nm. This filter is very helpful in that it filters the entire light spectrum except the laser line and therefore, no light enclosure is required to stop the ambient scattered light when working with the setup. The optical elements after the diffraction grating are mounted on a cage assembly system and connected to the camera. This part of the setup is fixed on a two axis translation stage that provides the ability to align the detection setup axis to the axis of the diffracted beams.

Since usually the axis of the specimen grating is not in the plane created by the two incident beams, the loading setup which includes the specimen itself is mounted on a 3-axis aligning platform. The platform was designed to provide in-plane X-Y translation and yaw rotation using three micrometer actuators.

In order to extract the phase of the interferogram of equation (3-10) it is possible to used phase stepping method. In this method a known series of changes in the optical path and hence the phase of one the interferometer arms is applied to the optical setup and the interferograms thus obtained will then be used for phase extraction. For this purpose one of the reflecting mirrors was mounted on a precision piezo actuator. The piezo has 15μm total travel with sub nanometer resolution and uses one of

[1] Full Width at Half Maximum

the channels of the piezo amplifier discussed in section 3.2.2. The phase stepping method and this part of the optical setup are discussed in more detail in Chapter 5.

For an incident beam of 632.8nm wavelength, from equation (3-4), the maximum possible specimen grating frequency that results in first diffraction order emerge perpendicular to the grating plane is 1580 line/mm corresponding to the grating pitch of 632.8nm. However, to work at this value the incident beam should be at glancing angle to the specimen surface which is technically impractical. For the current study, a grating pitch of 760 nm was chosen. This value results in 83% of the ultimate resolution limit for the optical setup. It should be note that this resolution is the initial resolution limit of the setup without any postprocessing on the interferogram data and is the result of treating the fringe pattern through equation (3-11). This resolution is improved to higher accuracies with alternative approaches introduced in Chapter 5. The chosen specimen grating pitch requires an incident beam angle of 56.4º. This angle is set by the two prism mirrors mounted on precision rotation stage.

In order to align the optical path such that the incident angle could be adjusted with a high accuracy, the rotation stages were mounted on two 14” long posts. Another optical rail was used to align the beam path within 0.2º parallel to post axis (1 mm in 350 mm). The zero point of the precision stage was found by reflecting back the incident beam such that it coincides with the aperture of the laser source, i.e. the beam is reflected back on its own path. These tolerances result in less than 0.5% error in estimated phase of equation (3-10).

As it was discussed earlier, when the specimen is loaded, the frequency of the specimen grating changes resulting in a variation in the angle of emergent of the diffraction orders. From equation (3-4), the relationship between the angle of the diffraction pattern and the strain value is

$$\sin\beta_m = \lambda f_s\left(\frac{\epsilon}{1+\epsilon}\right) \qquad \textbf{(3-12)}$$

This relation is shown in Figure 3-15, for the typical strain range of 10^{-6} to 5×10^{-1}. As shown in this figure, the maximum divergence value for 50% strains is within the half angle defined by the numerical aperture of the objective. This means that the full state of deformation can be tracked with constant setup parameters and no specific change is required during the course of deformation.

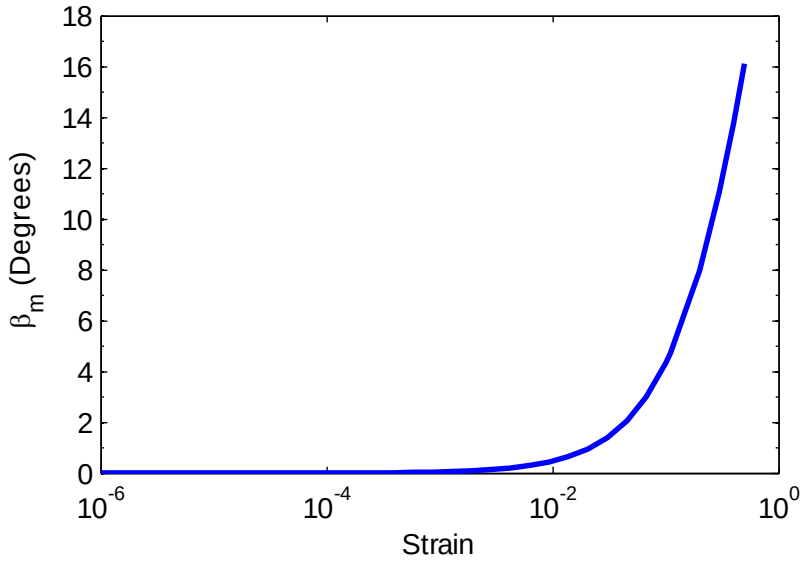

Figure 3-15- Divergence of the diffracted beam due to specimen deformation.

Interferometric optical setups are very sensitive to mechanical and acoustic vibrations. The reason is that any movement along the propagation axis of the beam even in the order of nanometers is a large fraction of the wavelength. For example 10nm vibration amplitude in one of the reflecting mirrors will result in 6^{o} phase change in light wave which affects the fringe location and results in vibration of the fringe lines. Therefore, the setup should be isolated from vibrations. The vibration is much more critical when phase stepping method is used to extract the phase of the interferogram data which is discussed in Chapter 5.

In order to avoid unwanted mechanical vibrations that are usually transmitted from the floor, the setup was assembled on a vibration isolation ST-UT2 optical table with I-2000 isolators. (Newport Inc., CA) This type of isolation provides passive isolation to the mechanical floor vibrations. The table was upgradable to active dampers that actively control the vibrations on the table. However, the vibration level before and after turning on the active dampers was about the same and no significant change in the vibration level in lower frequencies were detected. Therefore, the active dampers were returned to the vendor.

In order to prevent the acoustic vibrations from reaching the optical setup, an acoustic isolation enclosure was made from a layer of PVC sheets covered by 1" thick polyurethane-based acoustic absorber with Noise Reduction Coefficient (NRC) value of 76%. (McMaster Carr, OH) However, it turned out that the enclosure setup increases the vibration level on the table and was, therefore, removed.

The final optical setup is shown in Figure 3-16.

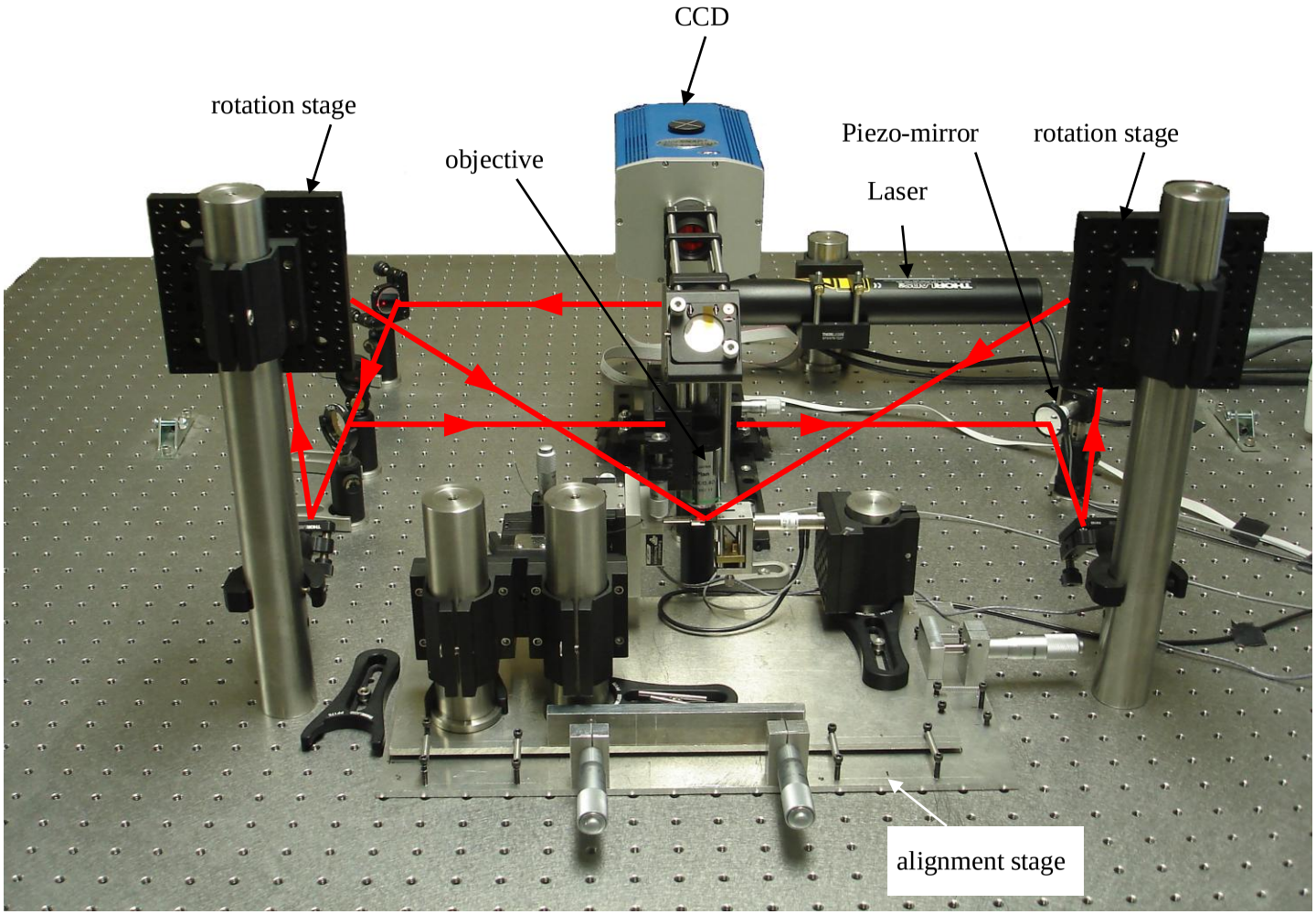

Figure 3-16- The optical setup for moiré interferometry. The beam path is shown in red.

3.4 Software and Control Setup

The control setup is schematically shown in Figure 3-17. A real-time target PC was used to control the piezo actuator, the phase stepping piezo/mirror, and to trigger the CCD camera. A precision data acquisition card (PCI-6289, National Instruments, TX) was used to communicate with individual devices. The card provides an 18 bit analog input resolution and four channels of analog output with 16 bit resolution. The piezo actuators were controlled by a -2 to +10V analog waveform and were driven by the servo-controller and the amplifier setup. Due to the ground loop that was formed between the piezo amplifier circuit and the D/A circuit, an isolating circuit was designed. Precision instrumentation amplifier (AD524, Analog Devices) was used in the isolating circuit to avoid the ground loop formation. The circuit decreased the electrical noise level from $4mV_{pk\text{-}pk}$ to $0.1mV_{pk\text{-}pk}$, resulting in an increase in the displacement accuracy of the piezo actuator to sub-nanometer resolution.

One of the digital output channels of the A/D card was used to trigger the camera. The camera, then, transfers the captured interferogram image to the host computer through an IEEE 1394 firewire connection.

The host PC provides an interface between user and the setup. The raw data is transferred between the host and target PC through an Ethernet connection. The post-processing and computation is done in the host PC. LabVIEW and LabVIEW Real-Time module (National Instruments, TX) were used for control and data acquisition on both computers.

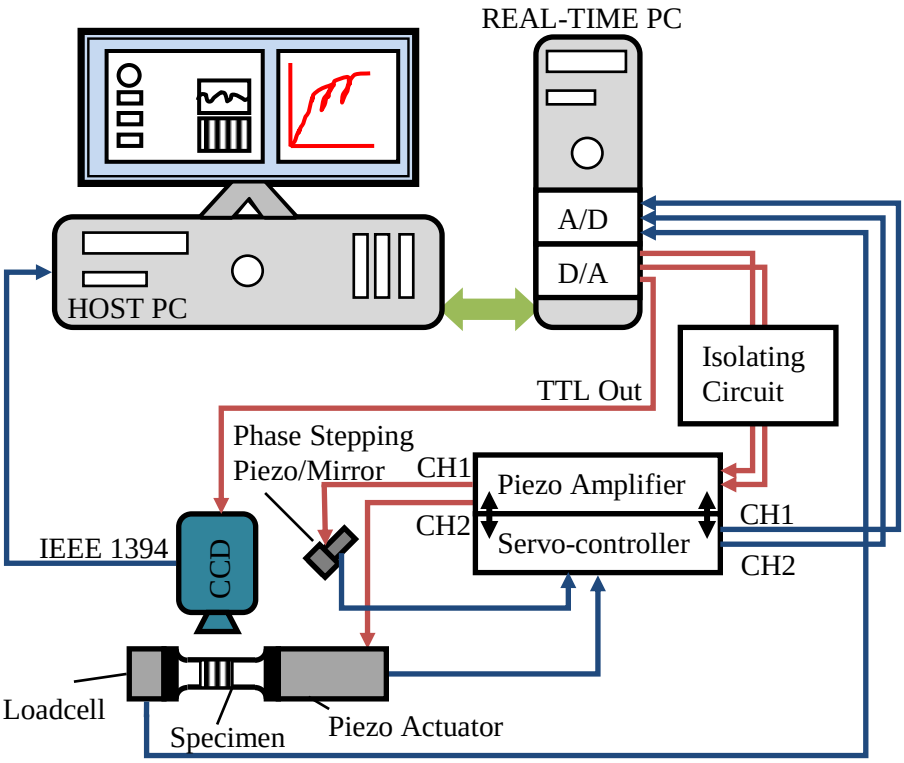

Figure 3-17- The control diagram of the experimental setup.

3.5 Summary

In this chapter, the design and fabrication process for the experimental setup was introduced. The loading setup and the novel gripper were discussed. The moiré interferometry technique and the respective optical setup were reviewed and finally, the software and control setup were presented.

Chapter 4

Sample Preparation

In the tensile testing of freestanding thin film specimens, sample design and fabrication is one of the main challenges of the experimental work. These samples need to be fabricated through a process that is clean room compatible and that is versatile enough to provide the capability of testing any material with minimum process development.

This chapter presents the results of developing a microfabrication process to make free- standing “dog-bone” thin film specimens for tensile testing. An efficient process is developed based on Aluminum metallization layer. Although Aluminum has been used as the model material, other metals like copper, gold, titanium, and their alloys can be used as the metallization layer. The fabrication results and the re-

lated characterizations are also discussed in this chapter. Also presented are the process development procedure and the related characterizations that were used to fabricate diffraction gratings on the thin film specimen through a Focused Ion Beam (FIB) milling process.

4.1 Sample Design

As it was discussed in section 2.2, sample preparation is one of the main challenges of the experimental work and is directly affected by the choice of other elements of the setup. On the other hand, since the specimens had to be fabricated through the microfabrication processes, the availability of the equipment is also another limiting parameter. The fabrication procedure was conducted at the MEMS facility of the Centre for Integrated RF Engineering (CIRFE) at the University of Waterloo and therefore the sample design was followed based on the available equipment and processes at this facility.

Initially, the window frame concept that was introduced earlier in section 2.2 was considered as the choice of sample preparation technique for this research. However, it turned out that the process is too complex and requires special fabrication equipment. Therefore, this method was abandoned and other fabrication procedures were sought. Among other sample preparation procedures that were discussed in section 2.2, the process that was used by Chasiotis *et al* [63] (Figure 2-3) has a relatively straight-forward procedure and requires less development. On the other hand, the ex-

perience of using photoresist as the sacrificial layer was available at the CIRFE group and therefore, this process was used as the sample preparation procedure.

The main three steps of the process are schematically shown in Figure 4-1. In this process, the substrate is first coated with the sacrificial layer material and the layer is then patterned to open anchors and dimples. Then the metallization layer is deposited and subsequently patterned to the dog-bone specimen shape. Finally, the sacrificial layer is etched and the metal film is released. The details of the procedure of implementing this process are presented in section 4.2.

The specimen geometry was designed based on the recommendation by ASTM standard. Although the standard is proposed for the tensile testing of macro-scale specimens, the geometry recommendations can still be used for micro-specimens to assure uniform stress across the gage section and to avoid stress concentration.

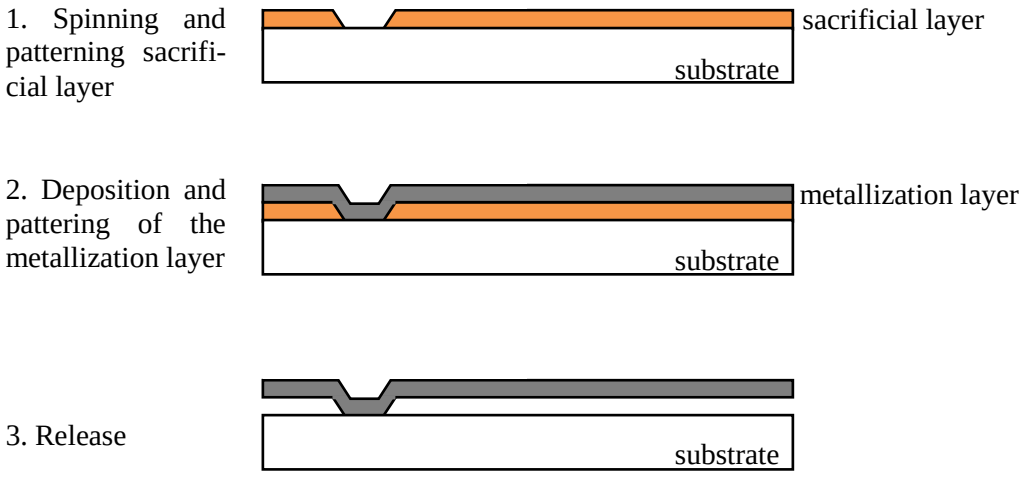

Figure 4-1- The main three steps of fabricating the thin film specimen.

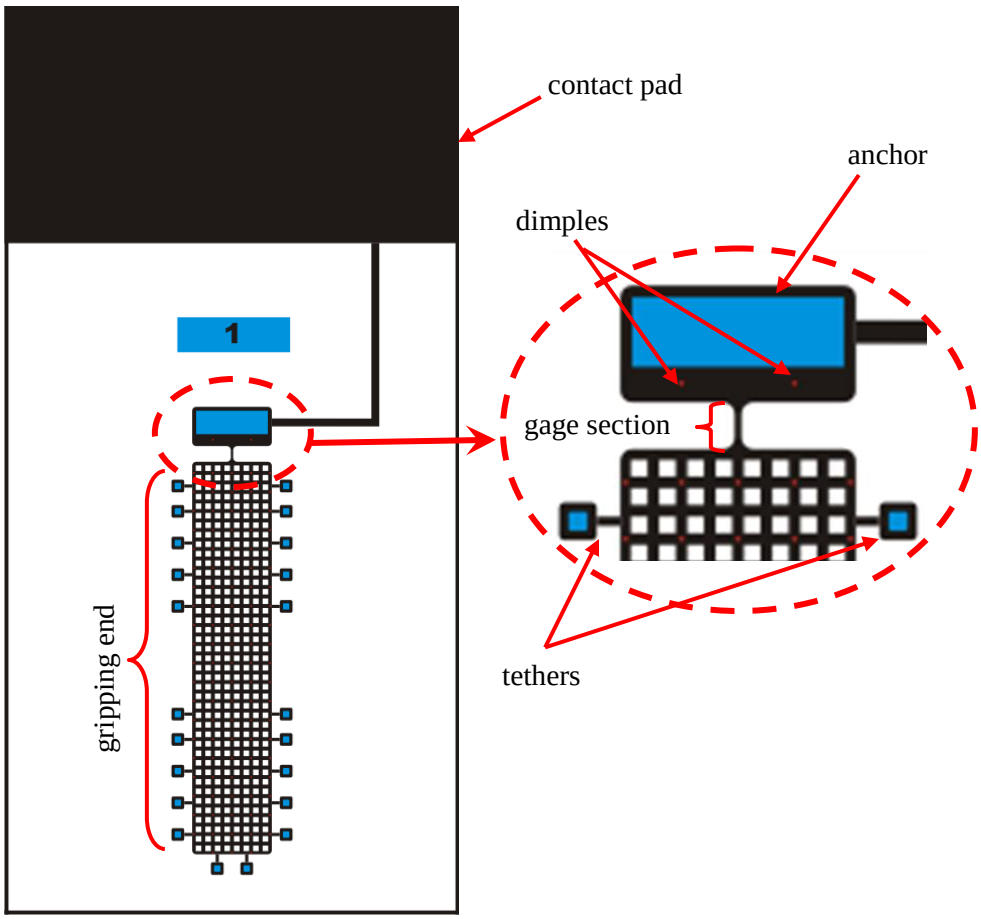

Figure 4-2- The final design of the thin film specimen. The metallization layer is shown in black, the anchors are shown in blue and the dimples are shown in red.

Figure 4-2 shows the specimen geometry that was achieved after a few design and fabrication iterations and revisions. The gage section is 30µm wide by 100µm long and is connected to the grip ends through 50µm radius fillets to reduce stress concentration. The film is anchored at one side on the glass substrate and is free at the other end. The free gripping end is about 3mm long and is griped at the first 1mm and the rest is left as a clearance to avoid the interference of the laser beam and the griper's side walls. The free end is tethered to the substrate to avoid any damage during

handling. Tethers are cut using a micro-needle at the time of tensile testing. Dimples were also added to prevent the film from stiction after the tethers are cut. The contact pad was added for two reasons. First, as it was discussed earlier, Focused Ion Beam (FIB) was used as the method to fabricate the specimen gratings. This method requires that the specimen be conductive and be grounded to avoid charge accumulation. In the very first tests the specimen was coated with a very thin layer of gold to serve as a conductive medium. However, after the FIB milling, when trying to remove the gold, the etchant have attacked the Al film and the film was delaminated. Therefore, the contact pad idea was used. The metallic film was connected to the contact pad and the pad was grounded in the FIB's specimen holder. Second, the contact pad was used to connect the ohm-meter that was used to align the specimen at the gripper.

4.2 Sample Fabrication

Having designed the sample, the main challenge is how to fabricate it. Over the past few decades, microfabrication processes have been widely used in industry; however, there is no single procedure that can be followed for fabrication and every design needs its own specifically-developed fabrication process. In this section the process development and the related results are presented. The development procedure took the better part of two terms and extensive time and effort was put into it and during this process invaluable experiences were achieved.

4.2.1 Substrate

The fabrication process starts with the choice of substrate material. In this application, substrate was not a part of the device. Therefore, the common substrate properties like electrical insulation, orientation, resistivity, and dopant material were not of importance. Therefore, silicon, as the cheapest and most available substrate material, could be used for this purpose. However, due to the high optical reflectivity of polished silicon substrate which resulted in higher stray beam intensity and hence more noise during the strain measurement, glass substrate was preferred over silicon. Glass, in contrary to polished silicon, transmits most of the incident beam and will help reduce the unwanted reflections and scattering.

During the process development runs, 1"×1" Emulsion masks were used for pattering. For these experiments, 3" glass wafers were initially diced into five 1"×1" chips which were used as substrate.

The first step in fabrication is substrate cleaning. In order to achieve high quality films, contaminants that have been accumulated on the substrate should be removed before processing. RCA clean has been the industry standard since the late 1960's. [88] In this procedure three steps are followed to remove organic residues, to strip the native oxide layer on silicon substrate, and to remove metal ions and inorganic contaminants. However, since in our application the effect of inorganic materials was negligible and we didn't use silicon as the substrate material, only the fist step, known as "RCA 1 Clean" was used for wafer cleaning. In this step a 5:1:1 $H_2O/H_2O_2/NH_4OH$ solution at 75-80^oC is used. The RCA 1 procedure is as follows:

- Add 100mL NH_4OH to 500mL DI Water in the designated RCA beaker;
- Heat to ~70ºC;
- Add 100mL Hydrogen Peroxide;
- Heat and stir to 75-80ºC;
- Submerge the wafers in the solution for 15 minutes;
- Rinse the beaker under running DI water to dilute and cool down the solution;
- Submerge the wafers in hot water beaker (~80-90ºC) for 15 minutes;
- Rinse the wafers with DI water and blow dry with nitrogen gun.

The "RCA 1" solution and more specifically the peroxide degrades after 24 hours in room temperature and after 30 minutes at 70ºC. Therefore, a fresh solution should be prepared for each wafer cleaning process.

4.2.2 Mask

During the process development steps, emulsion masks were used for patterning. This type of masks was cheaper than chrome masks and the fabrication equipment was available at UW. However, features smaller that 20μm are hard to pattern with these masks and edges are not as sharp. In fact the opaque material in emulsion has a gray-scale spectrum at the edges rather than a "black" and "white" pattern as in the case of chrome mask. This defect results in uneven edges in the specimen and will negatively affect the tensile test results. However, the price and availability of this

type of masks made them a good choice for process development. For this design three different masks were used. One mask was used to pattern the anchors, one was used to expose the dimples, and one mask was used to pattern the metallization layer.

Original pattern was plotted 10X on Mylar sheet which was then used to expose #206 AGHD high definition photoplates (Microchrome Technology, CA). The exposure time was experimentally found to be 12 seconds for bright-field mask and 14 seconds for dark-field masks. Exposed masks were then developed and fixed using 4:1 D-5/DI water developer and 4:1 F-4/DI water fixer solution, respectively. (Both from Microchrome Technology, CA) Originally, the developing process was 6.5 minutes develop time with 5 seconds dry every 15 seconds; however, it was found that this procedure over develops the masks and a 3.5 minute submerge in developer is sufficient. The developing process is highly sensitive to temperature, time, and agitation and controlled procedure should be followed for consistent results. During the fabrication of the dark-field emulsion masks for the dimples it was found out that on dark-field masks due to the gray spectrum at the edges, below a certain diameter the feature size on the mask is smaller than the one that was on the original pattern, regardless of the exposure time and developing conditions. Therefore, a calibration curve was found for a range of feature dimensions and the original pattern was designed such that the feature size of interest is obtained on the emulsion masks. The calibration curve is shown in Figure 4-3. For bright field masks there was no such problem observed.

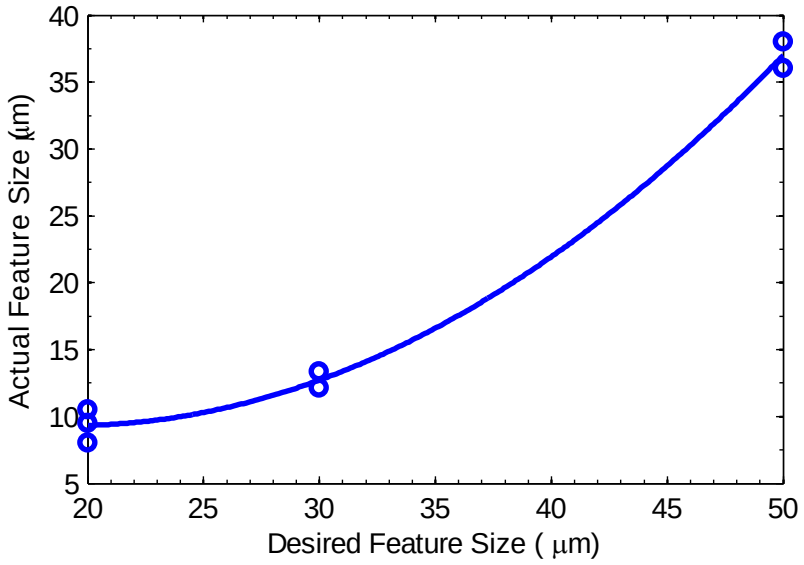

Figure 4-3- The calibration curve that was used to modify the size of the features on dark field emulsion mask.

Finally, the emulsion mask procedure is as follows:

- Expose the photoplate for 12 seconds for bright-field and 14 seconds for dark field mask;
- Develop in 4:1 D-5/DI water solution for 3':30" with slight agitation and 5 seconds dry every 25 seconds;
- Rinse the masks in DI water for 2 minutes;
- Submerge in fixer for 3 minutes and agitate lightly for 5 seconds every 25 seconds;
- Rinse the masks in DI water and leave them under flow bench to dry.

The mask usually gets contaminated by photoresist and dust over time. In order to clean them they were placed under running DI water and cleaned by Acetone to remove the photoresist residues.

4.2.3 Sacrificial Layer

AZ 3330 positive photoresist (AZ Electronic Materials, NJ) was used as the sacrificial layer. This resist is thermally stable to 125ºC which is well below the deposition temperature of most of metals. The resist was spin coated at 4000 rpm for 45 seconds to realize 2.3μm thickness and was soft-baked at 90ºC on vacuum hotplate for 5 minutes. The resist has to be first exposed by the anchor mask to open anchors and then by the dimple mask to make the dimples. However, since this layer was the first layer on the substrate there was no fixed alignment marks so that the two masks can be aligned against. In the very first fabrications, aluminum alignment marks were fabricated on the substrate and the sacrificial layer was then added and patterned. However, making those alignment marks added three more steps to the fabrication process which was unnecessary. In order to overcome this issue the photoresist was first exposed by the anchor mask and was then developed for a couple of seconds to etch away a small portion of the photoresist and to make the alignment marks visible under the aligner. It was then briefly blow dried and then exposed by the dimple mask. The aligner has a 500W unfiltered mercury lamp with a nominal 41mW/cm^2 power density. Since the photoresist was coated on glass and glass transmits most of the incident UV, longer exposure time was required comparing to the case of exposing resist on silicon, metal, or other reflective substrates. The exposure time was found experimentally to be 20 seconds in vacuum contact mode at 41mW/cm^2 power density for the anchor mask and was 10 seconds for the dimple mask. Resist was then post-exposure baked at 110ºC on vacuum hotplate for 60 seconds. AZ 300 MIF de-

veloper (AZ Electronic Materials, NJ) was used to develop the resist. The developing time was also found through a trial and error process. Although a 60 second develop time is sufficient for fresh developer solution, it was found that developing times of up to 90 seconds might be necessary depending on the age of developer solution.

The very first experiments showed that in order to avoid bubbling and delamination, the resist had to be hard-baked before the deposition of the metal layer. The resist was hard-baked at 110, 115, and 120ºC on a hotplate for 3-45 minutes and it was concluded that regardless of the bake time a minimum hard-bake temperature of 120ºC is required. The hard-bake step improves the process for two main reasons; first, the resist reflows during the hard-bake which helps better step coverage during metal deposition, and second, the solvent which is added to the resist to decrease its viscosity and hence to improve the spin coating process, will evaporate. This will prevent the delamination and bubbling during metal deposition. On the other hand, the hard bake process facilitates the cross-linking of the photoresist which makes the resist more resistance to flow at higher temperatures. The higher the hard-bake time the better the quality of the resist will be as an underlayer. However, higher bake times makes the resist harder to remove and more flow happens at the edges. Therefore, based on the observations on the optical microscope, a 20 minute hard-bake was used. The final process flow for sacrificial layer is as follows:

- Clean the mask using the procedure discussed in section 4.2.2;
- Dehydration bake at 120ºC for 180 seconds;
- Coat and spin AZ 3330 at 4000rpm for 45 seconds at acceleration of 5;

- Soft bake on hotplate at 90ºC for 5 minutes;
- Expose using the anchor mask for 20 seconds at 41mW/cm^2 density;
- Develop the photoresist for 2-5 seconds to realize the alignment marks;
- Briefly blow dry the substrate;
- Expose the dimple mask for 10 seconds;
- Post-exposure bake on vacuum hotplate at 110ºC for 60 seconds;
- Develop in AZ 300 MIF developer for 70 seconds (developing time depends on the age of the developer);
- Rinse in DI water and blow dry the wafer;
- Hard-bake on vacuum hotplate at 120ºC for 20 minutes.

This process recipe depends on many factors and has to be modified to some extent, based on the condition of developer, resist, aligner, and etc to achieve consistent results.

4.2.4 Metallization Layer

Aluminum is the material that was used in this thesis; however, any other metal can replace Aluminum in order to study its mechanical properties. The metallization layer is made through three steps, namely deposition, patterning, and etching. In what follows these processes will be discussed.

4.2.4.1 Deposition

Aluminum films were sputter deposited using Nanochrome DC sputtering system (Intelvc, Canada). The system has a sputtering-up configuration with one 6" sputtering target. Wafers were mounted on a carousal rotating at 7.5 rpm and were secured using Kapton® tape. The normal base pressure set point was at 5×10^{-6} torr; however, for the main and final batch of the specimens, the chamber was left under vacuum over night to obtain a base pressure of 2×10^{-7} torr. This low base pressure will help reduce the contaminating gases, and specifically reduces the amount of water molecules in the chamber which results in higher film quality. The recipe that was originally being used in the CIRFE lab was

Power	500Watts
Argon Flow	50sccm
Deposition Rate	140Å/min

The deposition pressure was 3.7mtorr and was being controlled by the argon flow. The system has a substrate heating setup; however, it was not in operational condition and therefore there was no control on the substrate temperature. During these depositions, the substrate temperature was measured using non-reversible temperature labels (OMEGA Engineering, CT) on the backside of the carousel and it was 60±5ºC for 56 minutes deposition.

4.2.4.2 Patterning

AZ 3312 (AZ Electronic Materials, CA) positive photoresist was used to pattern Aluminum films through the following procedure

- Coat and spin AZ 3312 at 3000 rpm for 30 seconds;
- Soft bake at 90ºC on vacuum hotplate for 60 seconds;
- Align the beam mask and expose for 12 seconds at 41 W/cm^2;
- Post exposure bake at 110ºC for 60 seconds;
- Develop in AZ 300 MIF developer for 60 seconds;
- Rinse in DI water and blow dry the wafer.

Same precautions as those discussed in section 4.2.3 should be followed in this step.

4.2.4.3 Etching

In order to etch aluminum films, the standard aluminums etchant was used. This etchant is a 16:2:1:1 solution of $H_3PO_4/H_2O/HNO_3/CH_3COOH$. The etchant is also known as PAN Etchant because of the three acids, namely Phosphoric, Acetic, and Nitric Acid. The solution was first heated to ~40ºC and wafers were then sub-merged in the solution. A slight agitation was used during etching. The etch rate of the solution was found to be 210nm/min. Wafers were rinsed with DI water and blow dried using the nitrogen gun after the etching process. The wet etching process causes an undercut in the specimens which results in a slightly trapezoidal cross-section in the gage section of the specimens. The solution to this problem was to use chlorine RIE etching. However, this equipment was not available in CIRFE and the double chamber RIE system of G2N clean-room that was capable of doing this etching was down during the course of this research. Therefore, the idea of dry etching of the beams was abandoned and aluminum films were etched using the PAN solution.

After the patterning, chips were prepared for the fabrication of diffraction gratings which is discussed in section 4.3. In preparation for that, chips were first flood exposed and the excessive photoresist were removed in developer. The remained photoresist residues on the Al film were then ashed using RIE. The ashing was done using oxygen plasma at 350mtorr, 50sccm Oxygen flow, 200W ICP power and 50W RF power for 600 seconds. After this process specimen were taken for FIB milling. Having done the milling, the chip was coated with protective photoresist layer and was diced into individual chips with one tensile specimen on each chip.

4.2.5 Release

A critical part of the fabrication process is the release step. In this step, the sacrificial underlayer is etched and the metal film becomes frees-standing. This process affects the final quality of the film in terms of stresses, warpage, and also the fabrication yield. Therefore, three different methods of release were tested in this thesis.

In the first set of specimens, the release was done using RIE.[1] Oxygen plasma was first used in releasing the specimens. However, it turned out that it takes a long RIE time for each release (after 3 hours the film was only partially released) and if high ICP powers were used, the metal film would have dramatically heated up. In another attempt, 2/50sccm CF_4/O_2 mixture was tested. The chemistry resulted in highly corrosive species and the high ion energies caused an extensive sputtering of the Al film during etching. The sputtered Al film was visibly re-deposited on the

[1] This part of the RIE work was conducted at the G2N clean room facility.

glass substrate. On the other hand, due to the high cost of RIE and the need for extensive process development, this process was abandoned.

In the second method, the ability of etching an exposed positive photoresist in the developer solution was used. The sacrificial layer was flood exposed from the backside of the glass substrate for 30 seconds and was then developed in the developer solution for 3 minutes. The film was checked under optical microscope and visually it was fully released. However, during the IPA dip process for the proceeding CO_2 dry, it turned out that there are still residues of photoresist left under the Al film that were attacked by the IPA. Even longer develop times did not removed the residues. On the other hand, the TMAH-based developer that was used for this purpose tends to attack the Al film.

In the third attempt, films were released using the AZ Kwik strip remover. (AZ Electronic Materials, CA) It is convenient and faster to strip the resist in elevated temperatures. Initially, the resist underlayer was etched in the stripper at 60ºC. However, it turned out that due to the flow of the photoresist at this temperature, the released films were more wrinkled. Therefore, the release was done at room temperature. To make sure that the resist is completely removed and that there are no residues left, chips were left in the stripper for a minimum of 48 hours and usually over the weekend. The specimens prepared with this process were wrinkle free and had high yield. After the release, samples were dried using CO_2 critical point drier to avoid the stiction of the released film to the substrate. For this purpose, released specimens were directly moved from stripper solution into pure IPA Petri dish. After two IPA

dips for 7.5 minutes each, specimens were moved into the critical point CO_2 dryer chamber (Tousimis, MD) for drying. At this point specimens are ready for tensile testing.

4.2.6 Fabrication Results

In order to fabricate the specimens through the process that was developed and discussed in the previous sections about 7 different batches were fabricated. Figure 4-4 shows the SEM image of the final revision of the fabricated sample. The gage section of the specimen is shown at higher magnification in Figure 4-5. The thickness of the specimen film was by average 660nm.

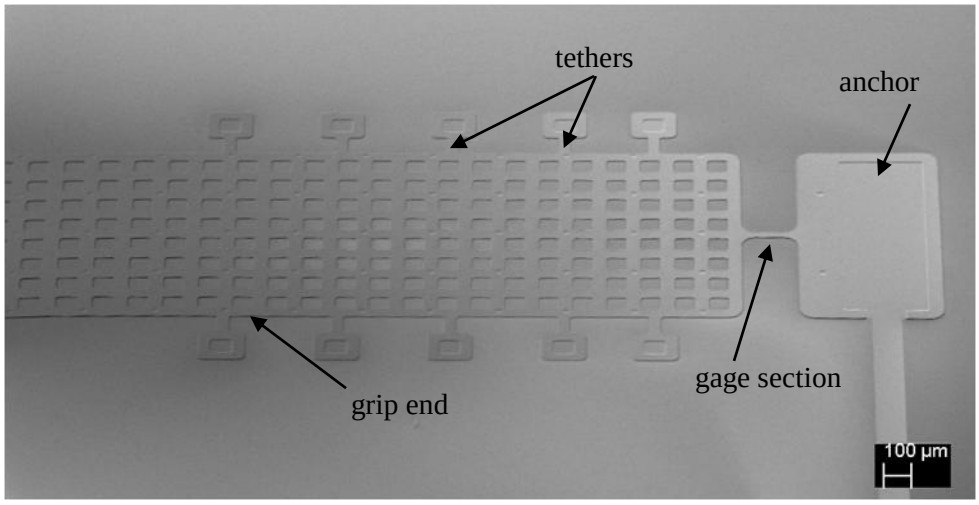

Figure 4-4- SEM image of the fabricated Aluminum thin film specimen.

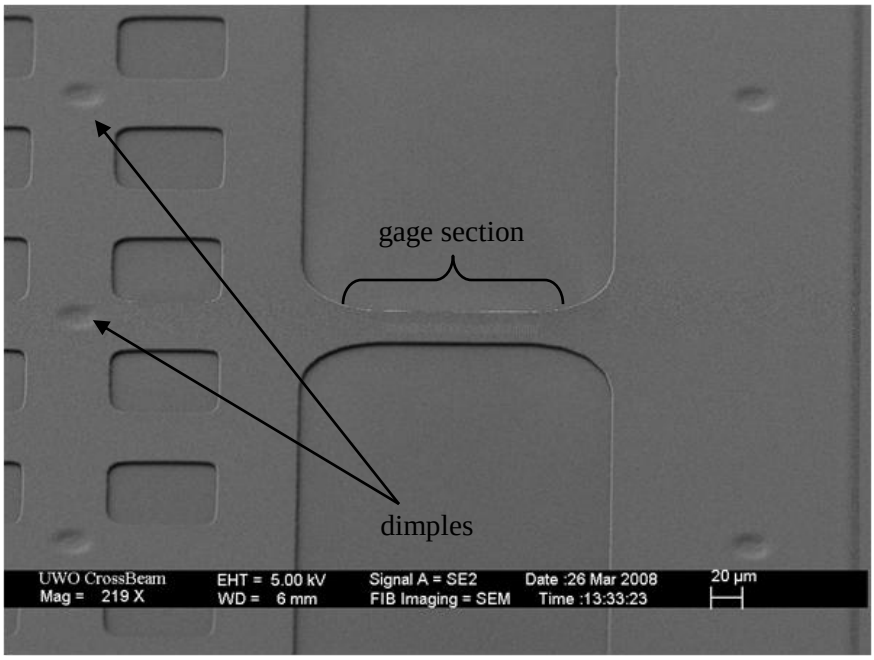

Figure 4-5- SEM image of the gage section of the fabricated thin film specimen.

One of the main issues that was investigated on the fabricated thin film specimens was the surface roughness of the Al film. The roughness affects the test results in two ways. First, since the films are very thin the surface roughness may cause stress concentrations at the surface. However, the roughness is an intrinsic characteristic of the film and cannot be avoided if a certain film under certain process conditions had to be studied. In other words, in order to change the film roughness, the fabrication parameters for the film has to be tuned which in turn results in a new film that may have different mechanical properties from the original film. On the other hand, the rough "hillocks" on the surface of the specimen give rise to scattering of the laser beam and introduce some noise in the strain measurement setup. Figure 4-6 shows the AFM image of the surface of four different specimens from four different

batches. The AFM images were obtained using an AFM (Digital Instruments, NY) in contact mode. The scanned area was 5μm×5μm and the scan frequency was 1Hz. As it can be seen from these images, although all films had been sputtered using the same deposition conditions, they have different surface morphology. The reason can be sought in inconsistency in the deposition pressure of the different batches, lack of control on the deposition temperature, and also the availability of different contaminants in the chamber. Figure 4-7 shows the SEM image of the corresponding AFM images of Figure 4-6.

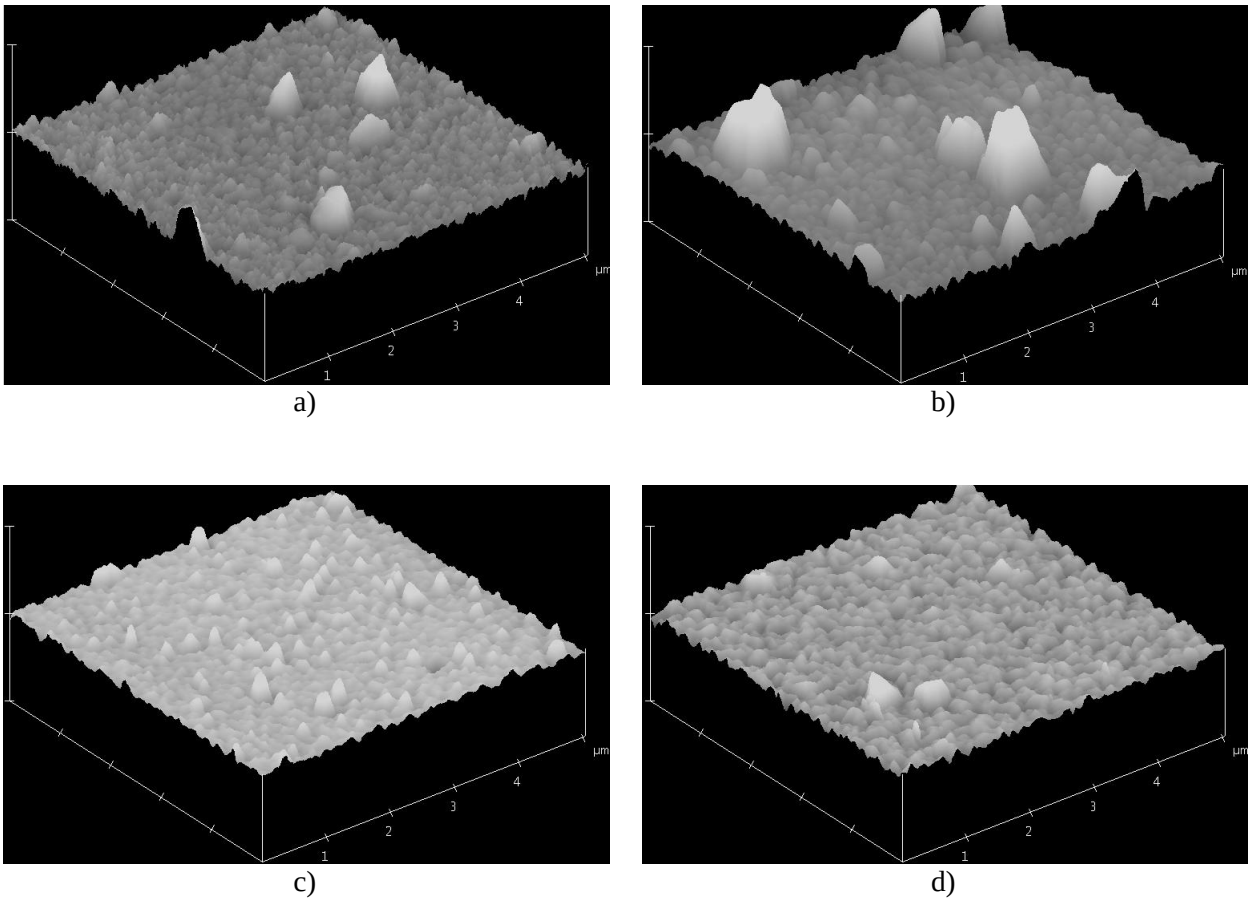

Figure 4-6- AFM image of the Aluminum surface from four different specimens from four different batches with same sputtering conditions. The height scale is 500nm/div.

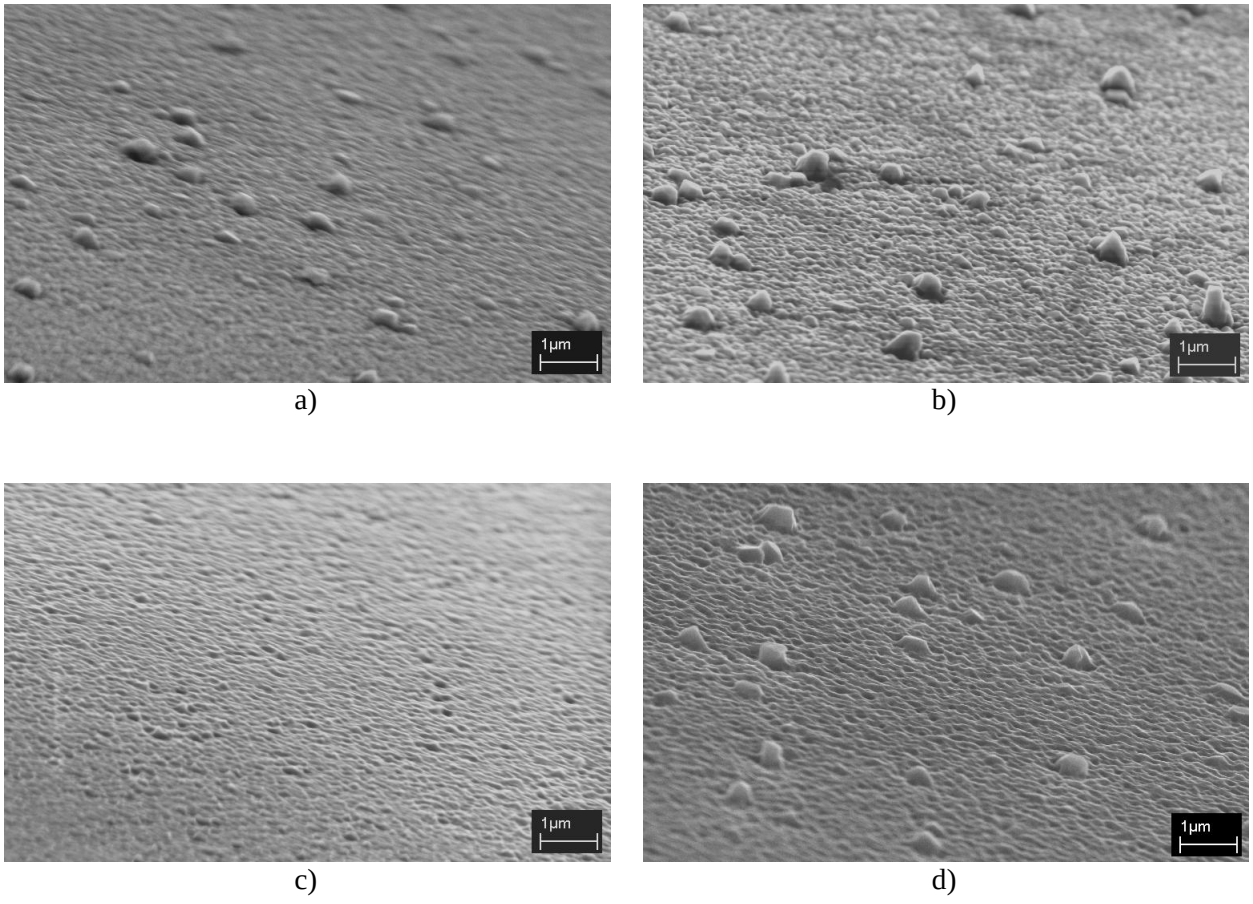

a) b)

c) d)

Figure 4-7- SEM image of the Aluminum surface from four different specimens from four different batches with same sputtering conditions. The magnification is 14,000X.

In order to study the microstructure of the thin film specimens, TEM analysis was preformed. Cross-sectional TEM samples were prepared by ultra-microtome.[1] Gage sections of the specimens were cut. Pieces were then placed on flat embedding molds and the molds were filled with LR White resin (Polysciences, Inc., PA). The resin was polymerized under UV light exposure for 48 hours at the temperature of -20ºC. Electron transparent thin longitudinal sections of the specimens were cut with a

[1] TEM samples were prepared by Marcia Reid at the Health Sciences Centre, McMaster University.

diamond knife mounted on Leica Ultracut UCT ultramicrotome (Leica Mikrosysteme, Austria). The sections were placed into Formvar-coated grids. The sections were analyzed in JEOL 2010 HR-TEM/STEM at the Canadian Centre for Electron Microscopy at McMaster University.

Figure 4-8 shows the cross-sectional TEM image of the as-deposited specimen at gage section. Grains are almost columnar across the section. The surface roughness of the film caused by the microstructure of the film can be clearly seen at the top of the image. The roughness is comparable to the smooth structure at the bottom of the film which was deposited on photoresist.

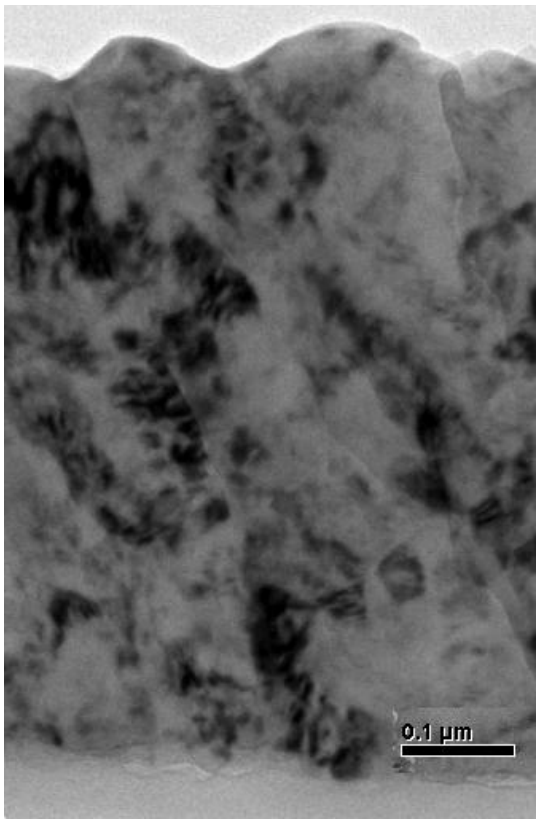

Figure 4-8- Bright-field TEM image of the cross-section of thin film specimens.

Since the ribbons that were prepared by ultramicrotome were relatively long (about 200μm long), the cutting line has passed through a few hillocks across the section. Figure 4-9 show the abnormal growth of these hillocks out of the surface of the film. These samples were in the same batch as the samples of Figure 4-6-b and Figure 4-7-b.

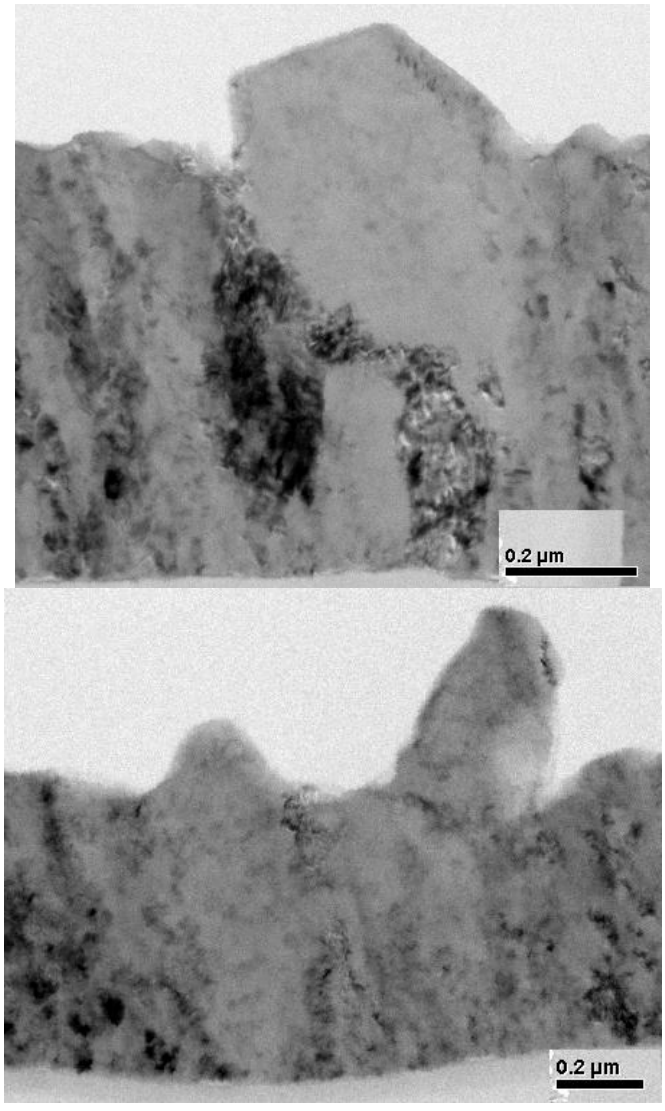

Figure 4-9- Bright-field TEM images of hillocks on the surface of the specimen.

4.3 Fabrication of the Specimen Grating

In order to efficiently use the moiré interferometry technique to measure the strain field, a dense specimen grating has to be fabricated on the surface of the thin film specimen. The fabrication of the specimen grating was one of the limiting factors in the spatial resolution and accuracy of the moiré interferometry. On the other hand, gratings fabricated through the classic replication techniques were prone to fracture and could not be exploited in large deformation measurements. With the advent of nanofabrication equipment, different techniques were used to fabricate high quality diffraction gratings on optical waveguides, switches, and other optical elements. Focused Ion Beam (FIB) milling [89-91] and UV holography [92,93] were among the most popular techniques in the fabrication of high frequency diffraction gratings. In this thesis the FIB milling was used to directly write the specimen grating on the surface of the specimens. In the following sections the FIB instrument is briefly introduced, and the fabrication results are presented. Since in FIB high energy beam of Ga ion is utilized to sputter off the material and mill the grating, the probable damage to the specimen is also discussed.

4.3.1 Focused Ion Beam Instrument

A basic focused ion beam (FIB) system is very similar to a scanning electron microscope (SEM) with a major difference in that FIB makes use of an ion beam for analysis instead of an electron beam. Accordingly, it consists of a vacuum chamber, a

liquid metal ion source (LMIS), an ion chamber, a sample stage, detectors, and gas delivery system as shown in Figure 4-10. A brief discussion of the main subsections of a typical FIB instrument will be covered in this section.

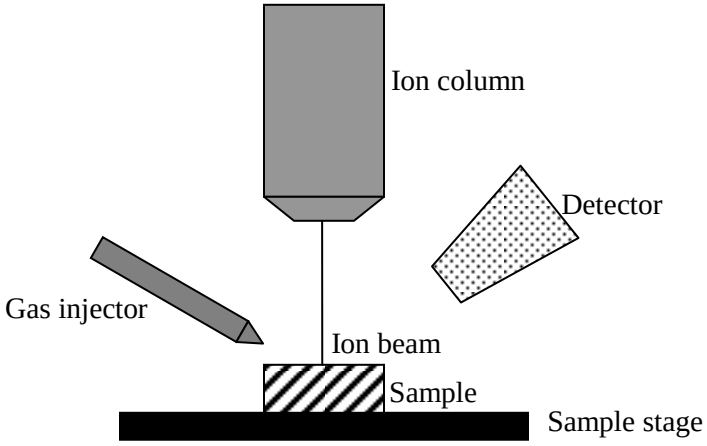

Figure 4-10- Basic FIB Instrument

The main part of a FIB system includes the liquid metal ion source (LMIS) and the ion column. LMIS consists of a tungsten needle attached to a metal source reservoir. There are a number of metals that can be used in LMIS. However, Gallium (Ga) is the most widely used metallic element in the commercial instruments for several reasons: i) it has a low melting point (29.8ºC); ii) liquid Ga has low volatility which helps the reservoir last longer; iii) it has low free surface tension which promotes its viscous behavior on the tungsten needle; iv) since Ga has a low vapor pressure, it can be used in pure form rather than in an alloyed compound.

Ga ions are emitted through a two step process; the heated molten Ga wets a W needle with a typical tip radius of ~2-5μm. Application of an electric field of 108 V/cm at the Ga wetted tip causes Ga to form a 2-5nm diameter point source in the shape of a 'Taylor Cone'. Once a balance between electrostatic and surface tension forces was achieved in the cone, the extraction voltage can pull Ga off the needle and ionize it by field evaporation of the metal at the cone end. Ga continuously wets and leaves the tip, giving rise to current density of $108A/cm^2$. Once the Ga ions left the tip, they are accelerated through a potential down the ion column. Typical FIB accelerating voltages are 5-50kV. Beam currents from a few pA to 20-30nA can then be obtained by using a set of different diameter apertures in the ion column. Similar to SEM, condenser and objective lenses are used for focusing and beam shaping.

FIB instruments are also used for micromachining applications. These applications include milling the sample and deposition of thin films on the sample. For this purpose, FIB systems are equipped with a gas injection subsystem that delivers the required gases for CVD of materials on the sample and adds the ability of etching and deposition to this instrument. Further details are beyond the scope of this report. (For more information cf. [94])

Today's commercial FIB systems are mostly integrated with other analytical equipment to increase the analysis capabilities. The most common dual platform is FIB/SEM. An energy dispersive spectrometry (EDS) detector may also be added for quantitative analysis. Integrating electron backscatter diffraction (EBSD) detectors

provides crystallographic information of the sample, while adding a secondary ion mass spectrometer (SIMS) will help elemental analysis.

4.3.2 Grating Fabrication Using Focused Ion Beam (FIB)

To fabricate the specimen grating the LEO/Zeiss 1540XB SEM/FIB Cross-beam at the Nanofabrication Laboratory of the University of Western Ontario was used. There are a number of parameters that can be adjusted for fabrication optimization. The ion dose, expressed in $\mu C/cm^2$, controls the amount of sputtering. Higher the dose of the beam, the sample will be irradiated with larger number of high energy ions and more ions are sputtered from the material resulting in deeper mill. The ion current on the other hand, controls the rate a required dose of ions is delivered to the specimen. Higher currents give faster milling and therefore require less amount of time and cost. However, higher beam current causes less focus in the beam and adds a "tail" to the beam, deteriorating the precision of the milled area. With precautions features as small as 5nm can be micromachined by focused ion beams. There are other parameters like accelerating voltage and beam angle that were used based on the previous experience of the lab and were not changed. The accelerating voltage of 30kV and beam angle of about 90^o was used throughout the thesis.

In the following sections, the results of fabricating specimen gratings with different beam parameters are presented.

4.3.3 Fabrication Results

As it was discussed earlier, diffraction gratings with 760nm pitch were used in this research. For the fabrication of these gratings, different beam parameters were used to develop a suitable process that provides efficient diffraction grating in a cost-effective process. For this purpose, two different beam currents namely 1nA and 200pA with three different ion doses, 2500, 5000, and 10000μC/cm^2 were used. Figure 4-11 shows the diffraction gratings made with these beam parameters. The 1nA gratings were milled on a 40μm×100μm area, while the 200pA gratings were milled on a 40μm×50μm area to minimize the milling time. As it can be seen from this figure, the 200pA gratings are more recognizable on the surface of the specimen. The reason was that the in the 1nA case, the beam could not be focused as fine as the 200pA case and the beam had a tail which rounded off the grating edges. As the ion dose is increased the depth of the diffraction gratings were increased. The depth of the grating has to be in such a way that it provides enough intensity in the diffracted beam and yet should be not too deep to induce stress concentration at the specimen surface. On the other for the case of the Al films that were used in this thesis, the grating depth should be high enough to give rise to an intensity that is higher than the intensity of the scattered beam from the rough hillocks on the specimen surface. Figure 4-12 shows an in-lens image of the grating milled with 200pA beam current and 5000μC/cm^2 ion dose. The cross-sectional view of this grating is shown in Figure 4-13. The cross-section was cut using FIB. In order to avoid unwanted sputtering during the FIB cutting, the specimen surface was capped by a thin layer of Platinum

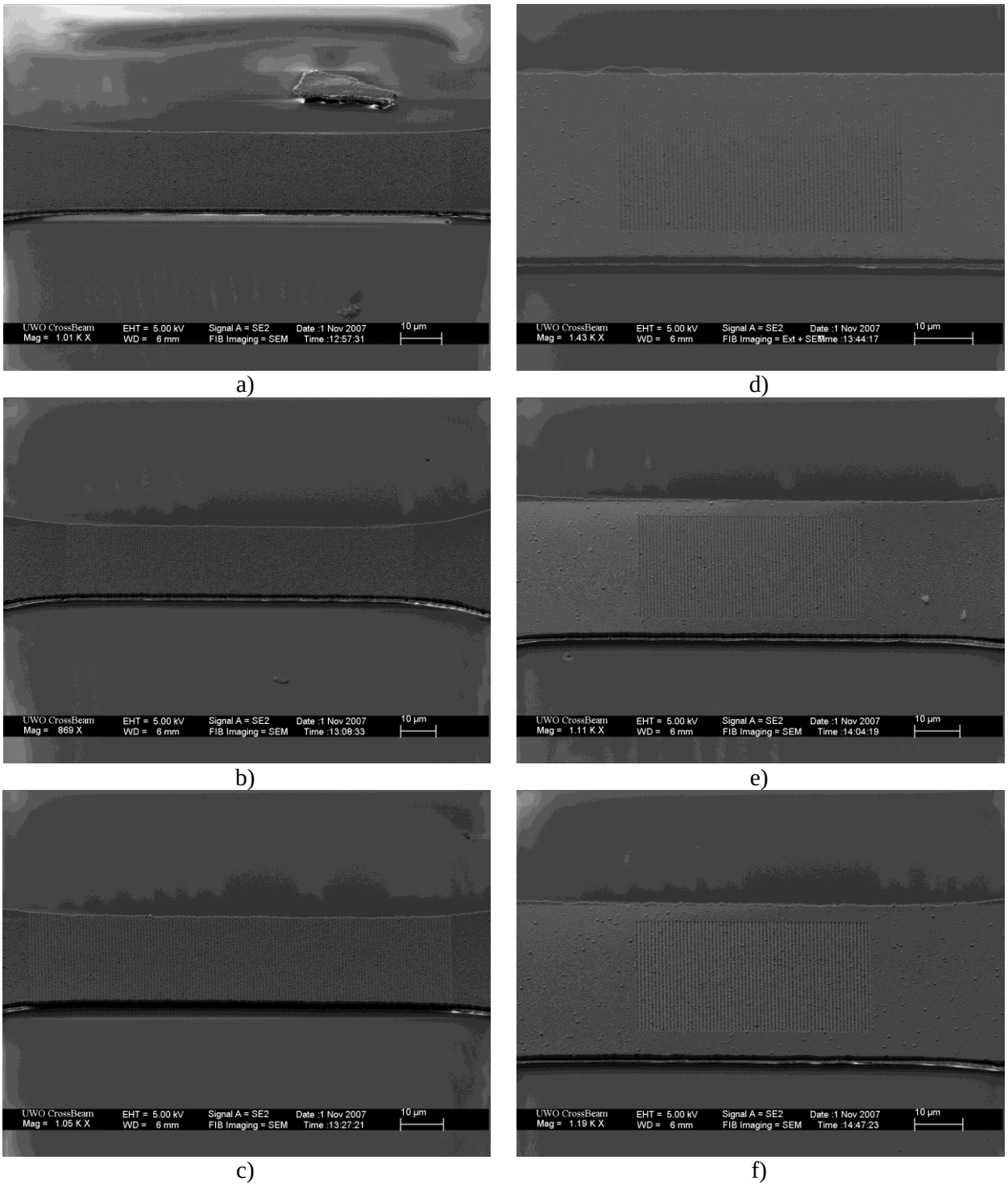

Figure 4-11- SEM images of FIB fabricated gratings, with beam current 1nA (a-c) and 200pA (d-f) and ion dose 2500µC/cm^2 (a,d), 5000µC/cm^2 (b,e), and 10000µC/cm^2 (c,f).

deposited from a metal organic gas in the FIB chamber. The depth of this grating was measured by SEM and was 130nm by average.

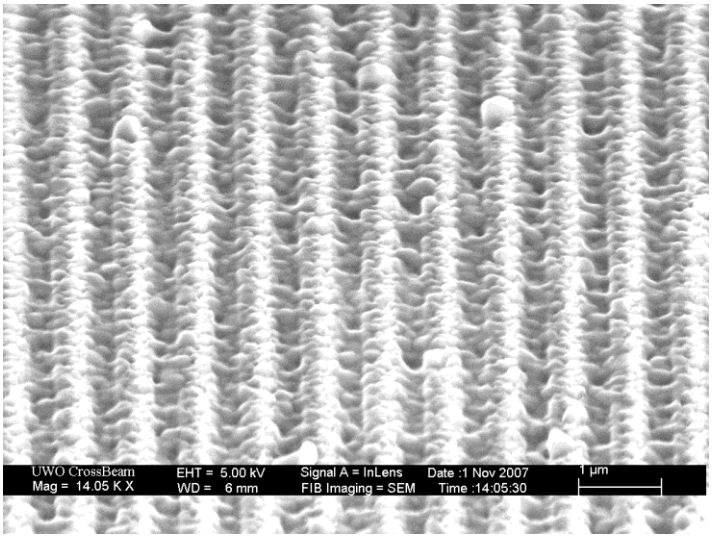

Figure 4-12- In-lens image of the grating milled with 200pA and 5000µC/cm^2.

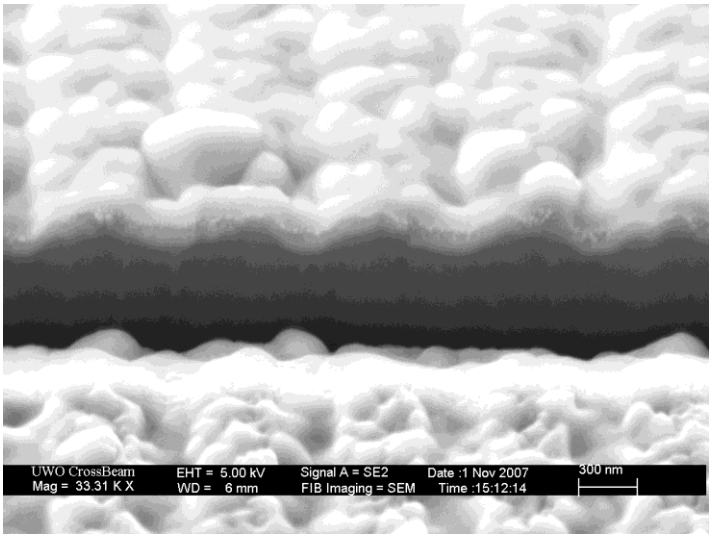

Figure 4-13- Cross-sectional view of the grating of Figure 4-12.

Due to the fine grating geometry that was fabricated by the 200pA beam current, this current was utilized for the rest of the grating fabrications. In order to compare the efficiency of the fabricated gratings with different ion doses in diffraction of light, three gratings were fabricated on the same specimen so that they are illuminated at the same spot by the laser beam and the difference in intensities recorded by the CCD is only because of the difference in grating efficiency. The grating areas are 10μm×30μm and are separate by a 20μm distance. (Figure 4-14) The measured intensities are shown in Figure 4-15 and Figure 4-16. As it can be seen from these images deeper gratings resulted in higher diffraction intensity. The noise in the intensity plots is resulted from scattering of light from the hillocks on the surface of the specimen.

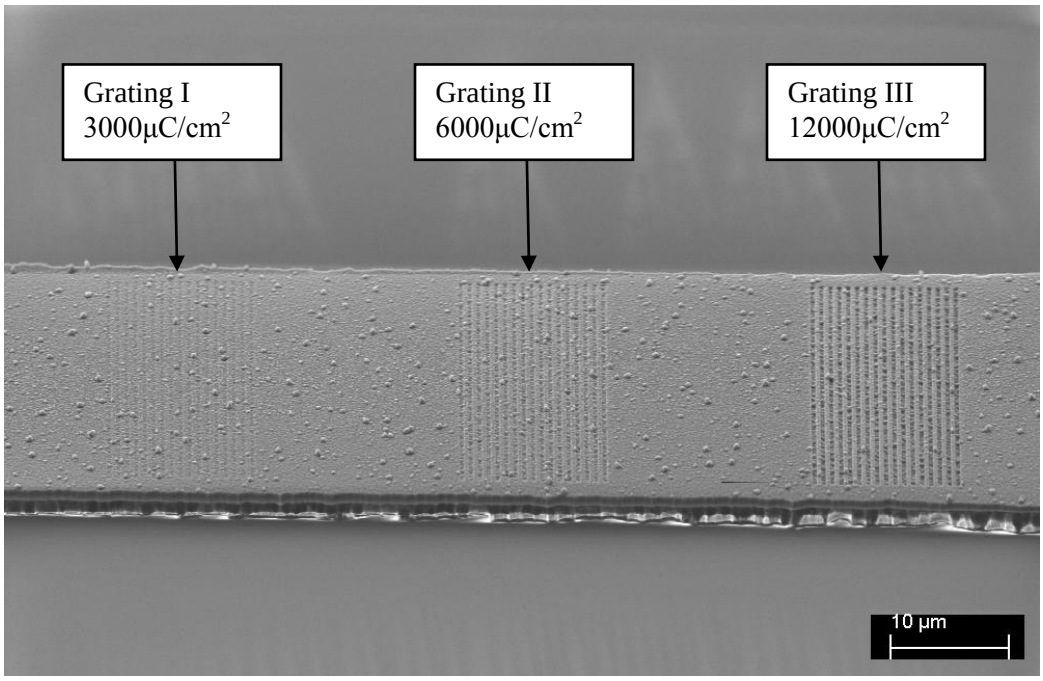

Figure 4-14- The specimen with three gratings that was used to compare diffracted intensities.

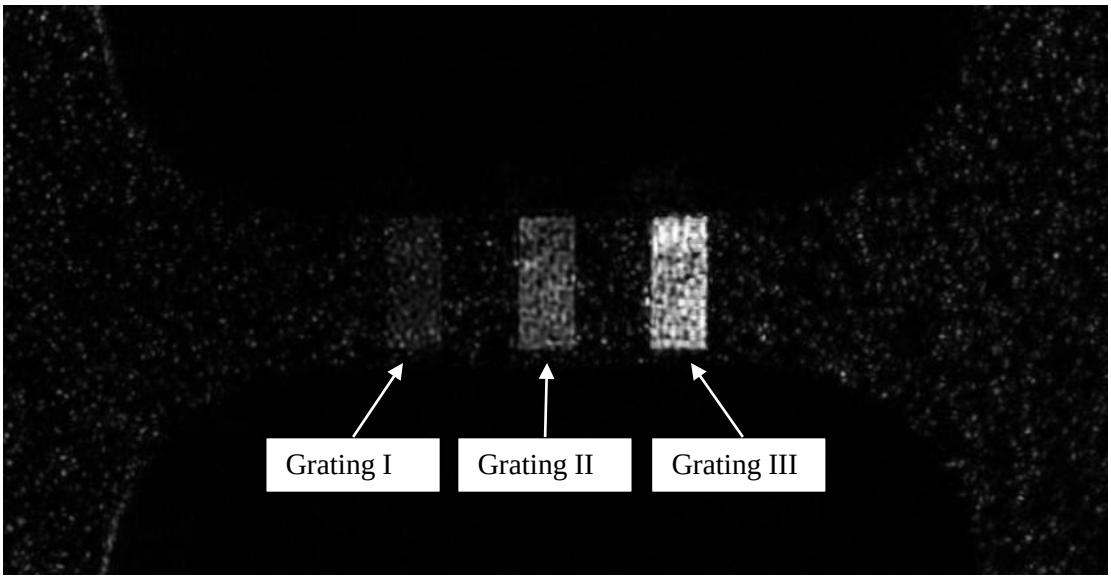

Figure 4-15- The intensity of the diffracted beam from the three gratings recorded by CCD camera.

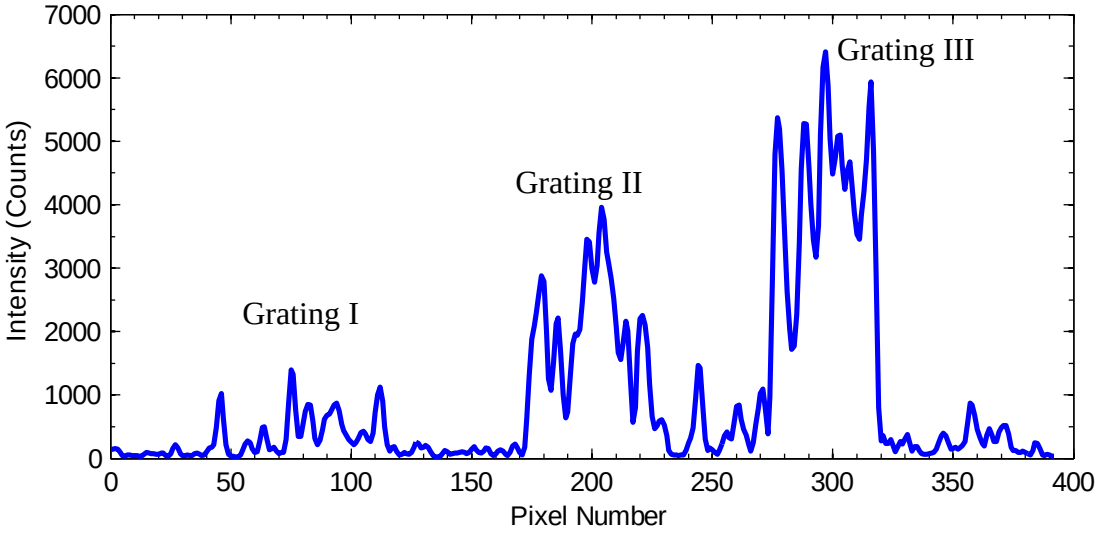

Figure 4-16- The intensity of the diffracted beam along the central line of Figure 4-15.

For the case of current specimen with the high roughness that was discussed in previous sections, the beam parameters of the grating of Figure 4-11-b was chosen, resulting in diffraction order that has higher intensity than the scattered light while the depth of grating is still smaller than the maximum peak to valley of the specimen roughness. For uniform monotonic tensile tests the grating area was set to 10μm×100μm (Figure 4-17) and for specimens with geometry inclusion the area was set to 30μm×50μm. (Figure 4-18) The hole in this figure is also fabricated by FIB milling with diameter of 5μm.

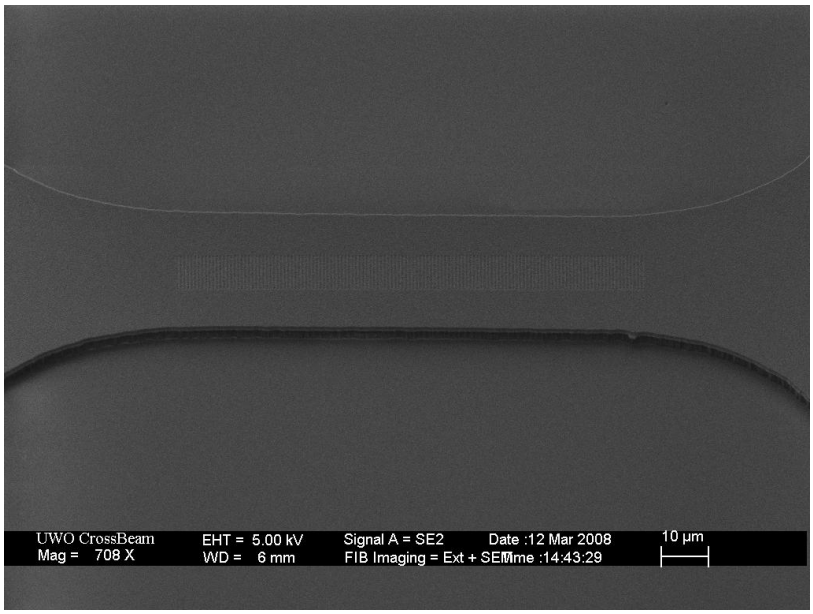

Figure 4-17- The specimen grating on the specimen for monotonic tensile test.

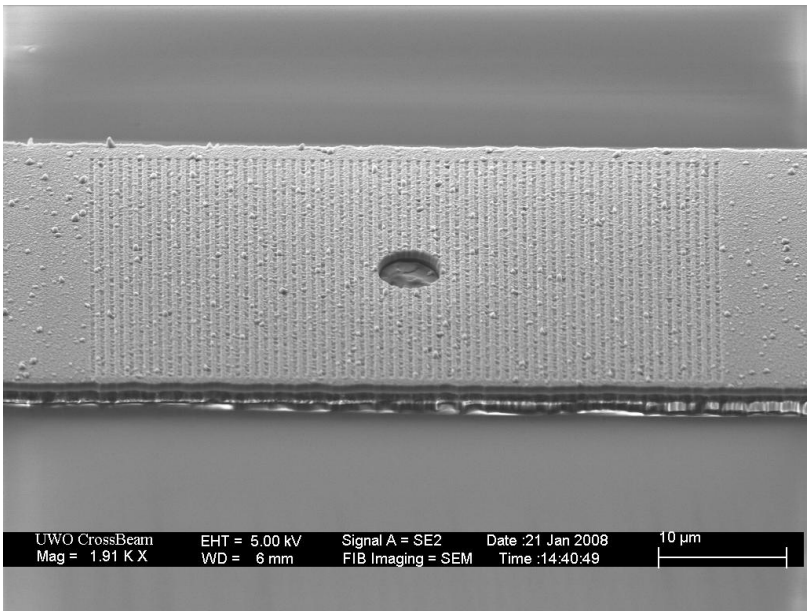

Figure 4-18- The specimen grating for measurement of strain field around a geometry inclusion.

4.3.4 Ion Damage to the Sample

When the ion beam strikes the sample, various particles and radiations are emitted from the sample through the interaction cascade. During this process, there are a number of unwanted phenomena that happen, leading to damage or anomalies in the sample. These damages are in the form of unwanted sputtering during imaging, Ga implantation, anomalous Ga phase formation, material redeposition, amorphization, ion beam heating, and beam induced grain growth.

Sputtering of sample surface is a consequence of ion beam interaction with the sample. This phenomenon even happens when low beam currents and energies are used for imaging. Typically, since imaging is performed in a normal beam angle comparing to the glancing angle of beam during milling, it can cause more severe

damage to the sample though lower beam currents and energies are used. In certain FIB conditions, the sputtered material can be redeposited on the target, forming an amorphous layer on the sample surface. Amorphization is perhaps one of the earliest FIB induced damages that was systematically studied. This phenomenon was extensively studied for Si samples. [95] Amorphization has also been reported in metallic materials. [96] Depending on the FIB configuration, the thickness of this layer can vary from a few nanometers to couple of hundreds of nanometers.

On the other hand, the ion beam that strikes the sample will penetrate deep into the crystal and rests in the sample. The Auger Electron Spectroscopy (AES) depth profile of Ga incorporated into single crystalline copper showed that high Ga concentrations of about 15% exist near the surface. [97] The implanted Ga may cause anomalous Ga phase formation or as in case of Al it may cause Ga enrichment at grain boundaries. [98] Ga phase formation was observed for a number of FCC materials. [99] The Cu_3Ga phase in FIB milled single crystalline copper samples has been reported. [100] The low melting point of Ga may result in Ga phases that have melting temperatures below room temperature. [96] Grain growth has been also reported in magnetic materials during FIB cutting of NiFe and FeCoN recording heads. This anomaly has been related to momentum transfer during FIB milling rather than local heating due to ion beam. [101]

In spite of these observations, evidence shows that this phase formation only happens when near normal beams are used and the glancing-angle approach as used in FIB milling can be less problematic. [94]

In order to study the possible ion damage to the sample, TEM studies were conducted on a specimen with gratings. Figure 4-19 shows the cut lines that were used to section specimens with ultramicrotome. Using this specimen, all three gratings were on the same TEM ribbon which makes the sample preparation and TEM analysis easier and more cost-effective. The initial TEM studies on the ion damage that was induced by the beam parameters of grating II, i.e. beam current 200pA and ion dose 6000μC/cm^2 are presented in this thesis.

Figure 4-20 shows the cross-sectional view of grating II. It can be clearly seen that depending on the initial surface roughness of the specimen, the same beam parameters result in different depth and geometry in each grating line.

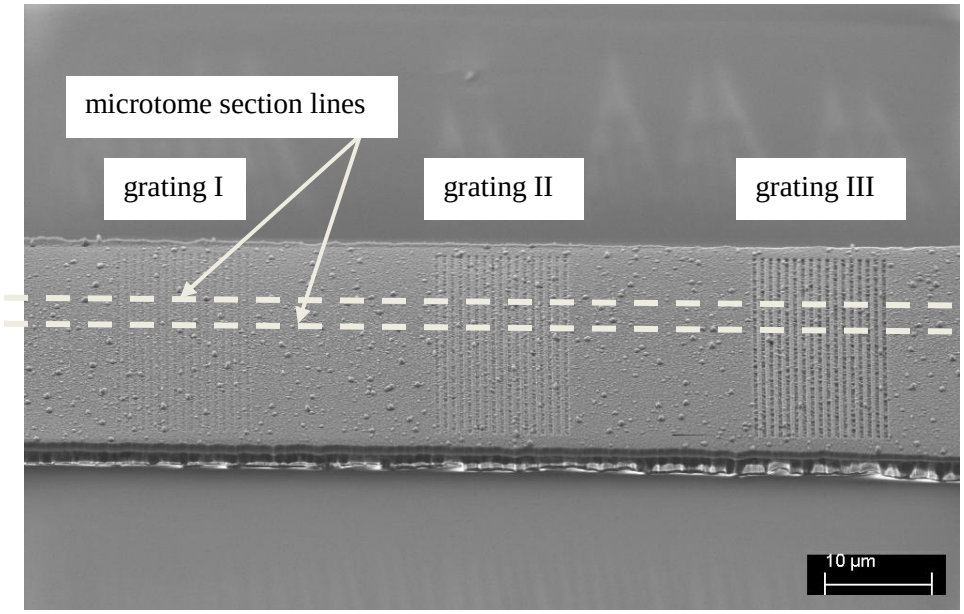

Figure 4-19- The microtome section lines for TEM sample preparation to study the ion damage to specimen.

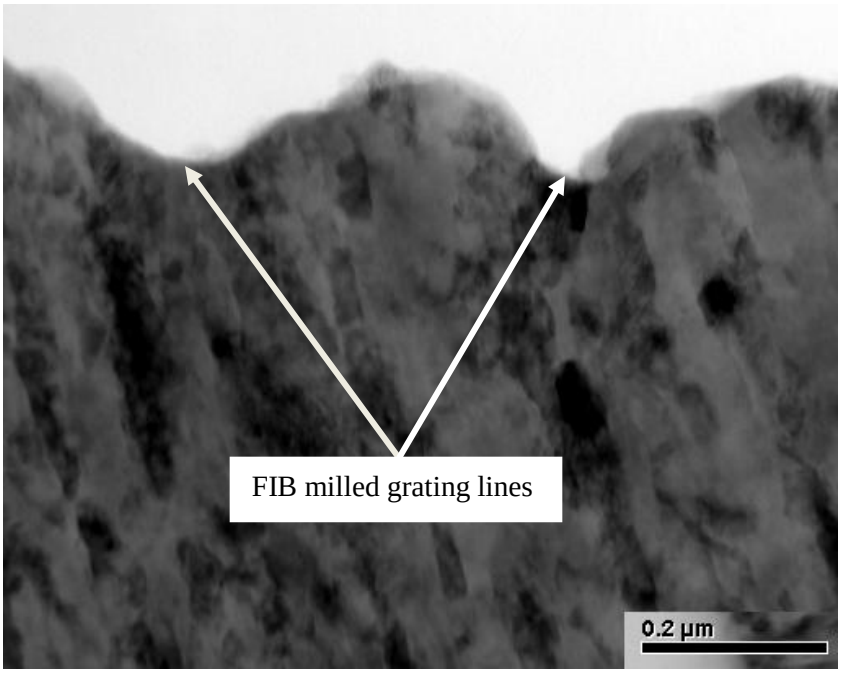

Figure 4-20- Cross-sectional TEM of the grating fabricated by FIB milling beam current 200pA and ion dose 6000µC/cm^2.

The amount of implanted Ga was measured using EDS in STEM mode. Initially, the depth profile of the implanted Ga was measured point-by-point across the section. However, it turned out that due to the electron energy the sample is heated and moves during the data acquisition, negatively affecting the accuracy of the method. Therefore, samples were coated with carbon which resulted in much less expansions during the data acquisition. EDS measurements were made using the data points shown in Figure 4-21. The points are in an average distance of 6nm. However, it turned out that although the specimen is fixed during the acquisition from one data point, after the measurement on 13 points, the specimen has drastically moved. Ga concentration of up to 5.8 at% was recorded. However, due to the movement of the sample it cannot be reliably assigned to a specific point.

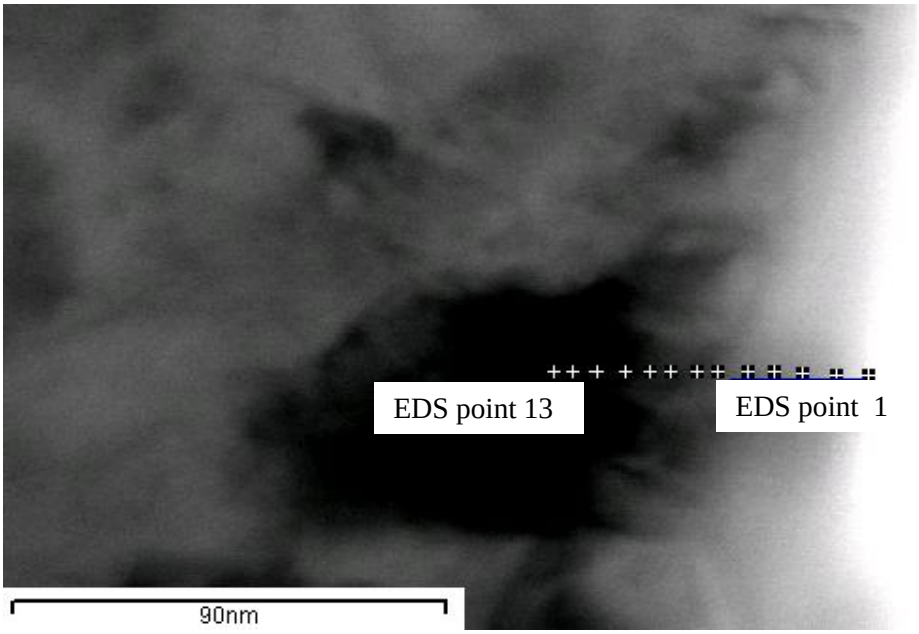

Figure 4-21- The point-by-point EDS measurement across the section of the specimen in the middle of a grating line.

In order to overcome the sample movement issue, the line-scan capability of STEM was used to map the elements across a line. In this way since the scan speed is much faster the total movement in the specimen was below 15nm during the data acquisition. Figure 4-22 shows the scan line that was used in these measurements. Figure 4-23 shows intensity count for Oxygen, Gallium, and Aluminum Kα1 line across the scan line. The data are normalized based on the maximum intensity of each element. Software was not capable of applying EDS corrections to the recorded intensities and therefore, the data does not reveal the concentration of the material. However, as it can be seen from this figure, initially the aluminum concentration is low at the native oxide layer on the film and it is then increased to a constant value. The high concentration of oxygen at the surface shows the existence of the oxide layer.

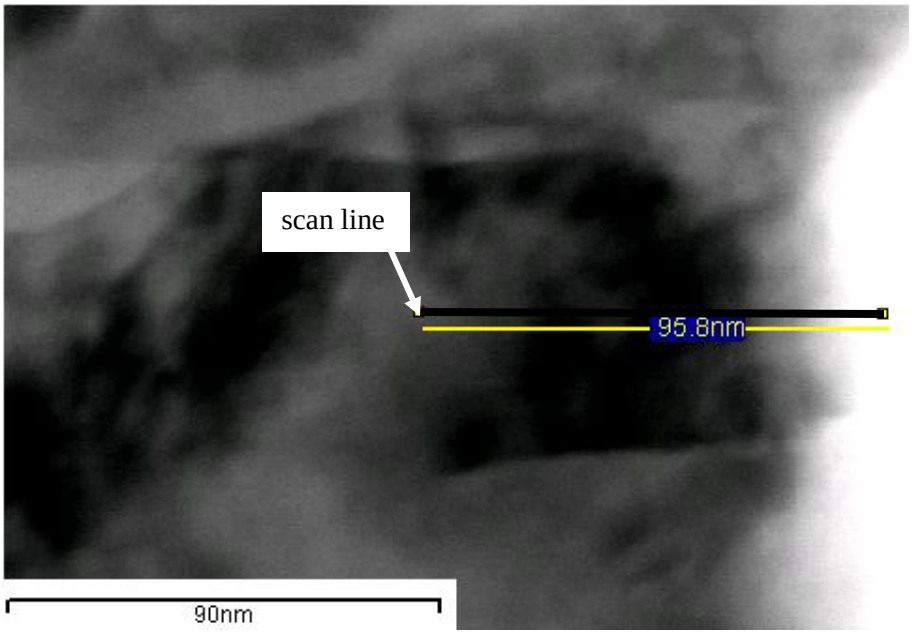

Figure 4-22- The cross sectional image of EDS line scan measurements.

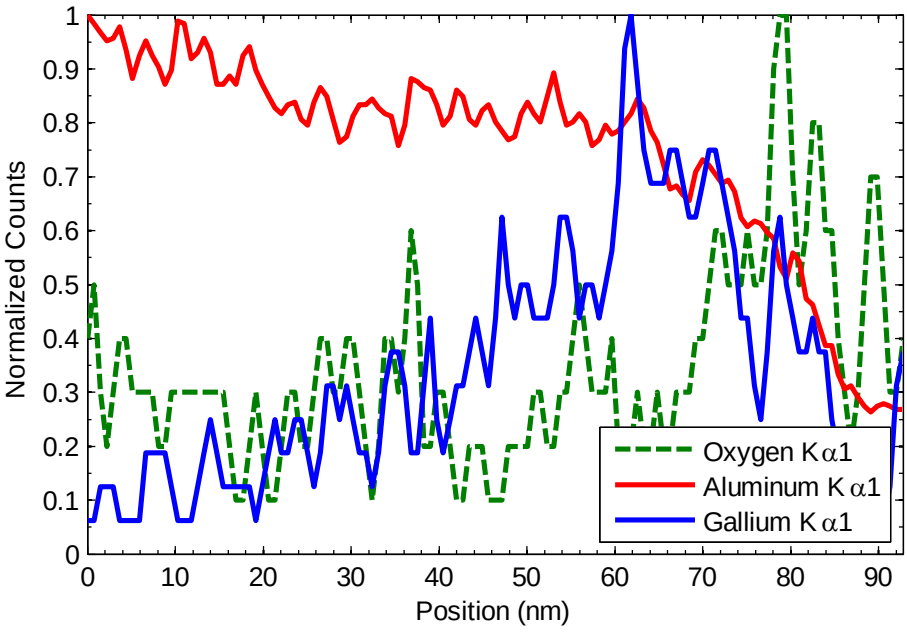

Figure 4-23- The normalized EDS count for Gallium, Aluminum, and Oxygen Kα1 line across the line shown in Figure 4-22.

The gallium concentration increases to a maximum below the surface and then decreases. This result is in good agreement with the AES depth profile measured by [97].

The Ga concentration is also studied in the area below the FIB milled grating lines. Figure 4-24 shows the EDS scan line and Figure 4-25 shows the Ga concentration along this line. It can be clearly seen that the Ga has been implanted in the milled area. The Ga concentration is maximum at the middle of the grating line and is decreased in distance.

The other microstructural damage that could provide a better understanding of the level of damage was amorphization. One method to find amorphous layer is to do selective area diffraction (SAD) on the area of interest and check the diffraction patterns. However, the smallest beam size that was achieved was visually much larger than the size of the areas that were to analyze. Therefore, this method was abandoned. Since the TEM was capable of taking high resolution images, high resolution imaging was tried. However, it turned out that the polymer that was used to embed the samples is interfering and the captured images were not reliable. Therefore, in the initial TEM analysis we were unable to study the amorphization layer.

In conclusion, since ion damage to the sample is not yet fully understood, FIB should be used with more caution and further microstructural studies had to be conducted to evaluate the level of micro-structural damage to the sample.

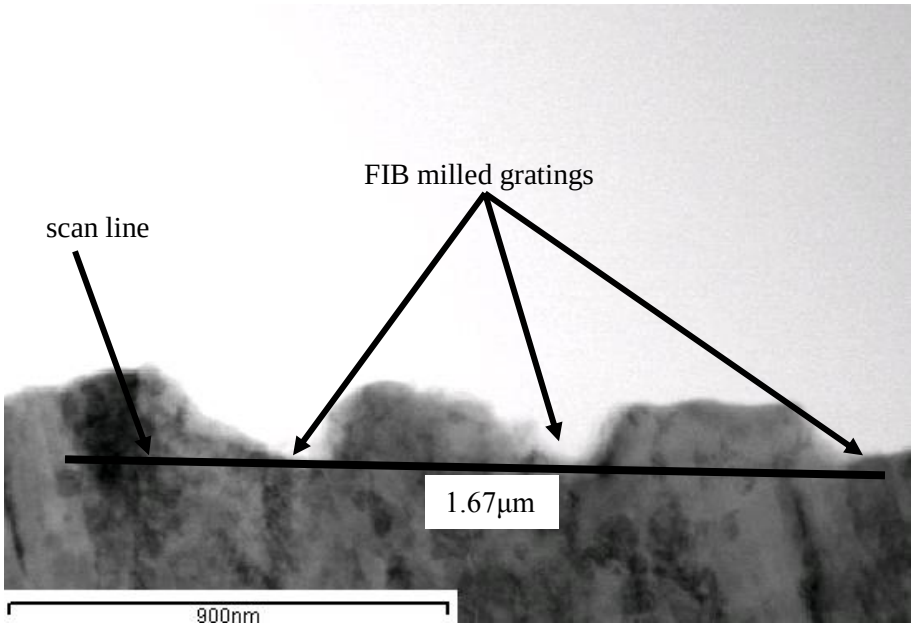

Figure 4-24- The EDS scan line across the gratings.

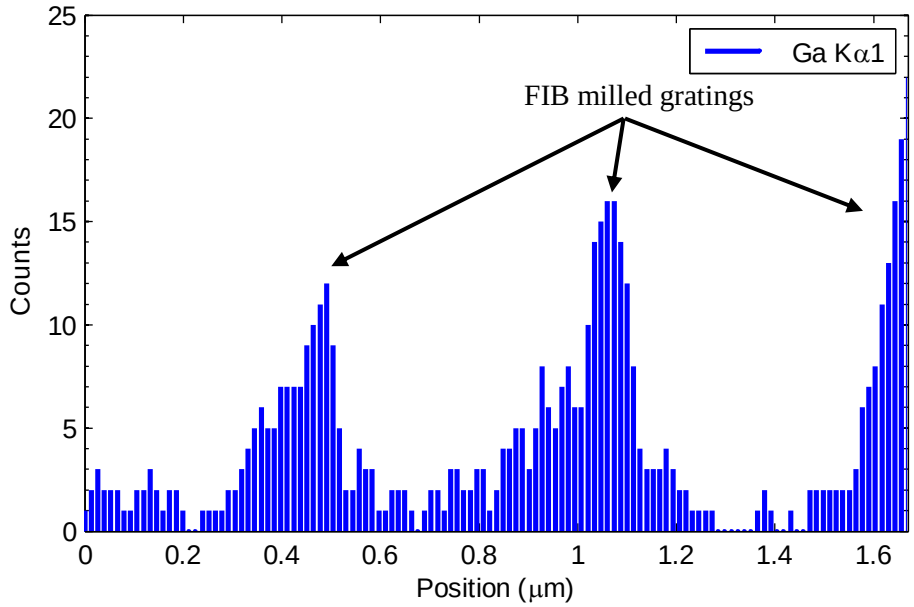

Figure 4-25- Ga concentration below the FIB milled area.

4.4 Summary

The microfabrication process was discussed in this chapter. A versatile process was developed to fabricate thin film dog-bone specimens. Aluminum was used as the metallization layer; however, any other metal can be used to probe its mechanical behavior. The films were characterized by AFM and TEM. The AFM measurements show that the main source of surface roughness is the hillocks that are formed during sputtering process, and that the size of these hillocks is process dependant. The TEM analysis revealed that hillocks are formed from the very beginning of the deposition process and form abnormal large grains.

The process of fabricating the specimen with FIB instrument was discussed. Different gratings were milled on the specimen and their diffraction efficiency was studied. The ion damage to the sample was briefly probed using STEM and EDS. The results showed that the Ga element has been implanted in the film during the FIB milling of the gratings. The microstructural damage need to be investigated in more detail to make sure that the process of grating fabrication does not alter the mechanical and microstructural characteristics of the specimen.

Chapter 5
Phase Extraction and Calculation of Strain Field

As it was discussed in section 3.3.1, for accurate extraction of the displacement or strain field from the moiré interferogram data, the phase of the interferogram should be extracted. In this chapter, two different methods namely phase stepping and continuous wavelet transformation (CWT) are presented. The CWT method is discussed in more details and is evaluated against simulated and experimental interferograms. The accuracy and feasibility of this technique in phase extraction and strain calculation is also discussed.

5.1 Introduction

In section 3.3, it was discussed that the resultant moiré interferogram is in the general form of a cosine waveform,

$$I(x,y) = I_0(x,y) + \gamma(x,y)\cos\phi(x,y) \quad \textbf{(5-1)}$$

where $\phi(x,y)$ is the phase of the interferogram. From equation (3-10), the phase of the interferogram is correlated to the displacement field by

$$\phi(x,y) = 4\pi f_s U(x,y) \quad \textbf{(5-2)}$$

Combining equations (3-2) and (5-2), the strain field is correlated to the local frequency of the interferogram. In other words, strain field is the instantaneous frequency of the interferogram, i.e.

$$\frac{\partial\phi(x,y)}{\partial x} = 4\pi f_s \epsilon_{xx}(x,y) \quad \textbf{(5-3)}$$

The same correlation applies to ϵ_{yy} and ϵ_{xy}. The calculation of displacement or strain field depends on the choice of the phase extraction method. Some techniques directly provide the phase of the interferogram while some other provide the instantaneous frequency of the interferogram. Regardless of which one is calculated directly from the interferogram data, either one can trivially be obtained through a process of either integration or derivation.

Many methods have been used to extract the phase or instantaneous frequency of the interferogram, and most of them were derived from general signal processing

techniques. Phase stepping [102], Fourier Transform [76], Windowed Fourier Transform [103], and Wavelet Transformations [104-116] were among the methods that have been widely used to extract the phase information. Except for phase stepping, other methods are numerical postprocessing methods and among them, Wavelet Transformations have better localization and accuracy. In phase stepping, however, the optical setup is adjusted for different phase shifts to find the phase map of the interferogram. Therefore, for the current research, phase stepping and Wavelet Transformations were used to evaluate the phase information and calculate the strain and displacement field.

5.2 Phase Stepping

Phase stepping is, perhaps, one of the oldest techniques that was used in extracting the phase information from an interferogram. The concept and different techniques of this method has been introduced in classic literature. [102]

Recalling equation (5-1) for any recorded interferogram intensity, there are three unknowns included in it. These unknowns are background intensity $I_0(x,y)$, visibility $\gamma(x,y)$, and the phase $\phi(x,y)$. The purpose of phase stepping is to increase the information data to three equations so that all unknowns are calculated and albeit the phase information can be retrieved.

In phase stepping, three or more images of the same displacement field are recorded and in each image a known phase change is applied to the optical path. In

order to apply this phase change, one of the mirrors was mounted on a piezo actuator, as shown in Figure 3-14. If in each stepping, the optical path is changed by a known distance δ_i, for three phase steps, the recorded interferograms are

$$I_1(x,y) = I_0(x,y) + \gamma(x,y)\cos(\phi(x,y) + \frac{2\pi}{\lambda}\delta_1)$$

$$I_2(x,y) = I_0(x,y) + \gamma(x,y)\cos(\phi(x,y) + \frac{2\pi}{\lambda}\delta_2) \quad \textbf{(5-4)}$$

$$I_3(x,y) = I_0(x,y) + \gamma(x,y)\cos(\phi(x,y) + \frac{2\pi}{\lambda}\delta_3)$$

and therefore, the phase information can be extracted by solving the set of equations. There are many different implementations for this concept and each has its own advantages toward a more reliable phase extraction. This method requires that while the images are recorded and the phase stepping is in progress the interferogram freezes at a fixed location. Therefore, the method is very sensitive to mechanical and acoustic vibrations in the optical setup. As it can be seen from equation (5-4), the tolerable vibrations are within a fraction of the wavelength of the laser beam. This method on the other hand is sensitive to CCD non-linearity, piezoelectric displacement resolution, and in fact requires at least three times the capturing time which reduces the strain measurement speed. However, if the phase steps δ_i are chosen in a specific arrangement, the phase information can be extracted by a relatively simple arithmetic manipulation.

Due to the high vibration level of the lab that these tests were conducted in, the phase stepping method was abandoned. Figure 5-1 shows consecutive images of the same interferogram over time. As it can be seen in this figure, although all images represent

the same interferogram, due to mechanical vibrations, the fringe lines have moved from their position inducing unwanted phase change in the interferogram data.

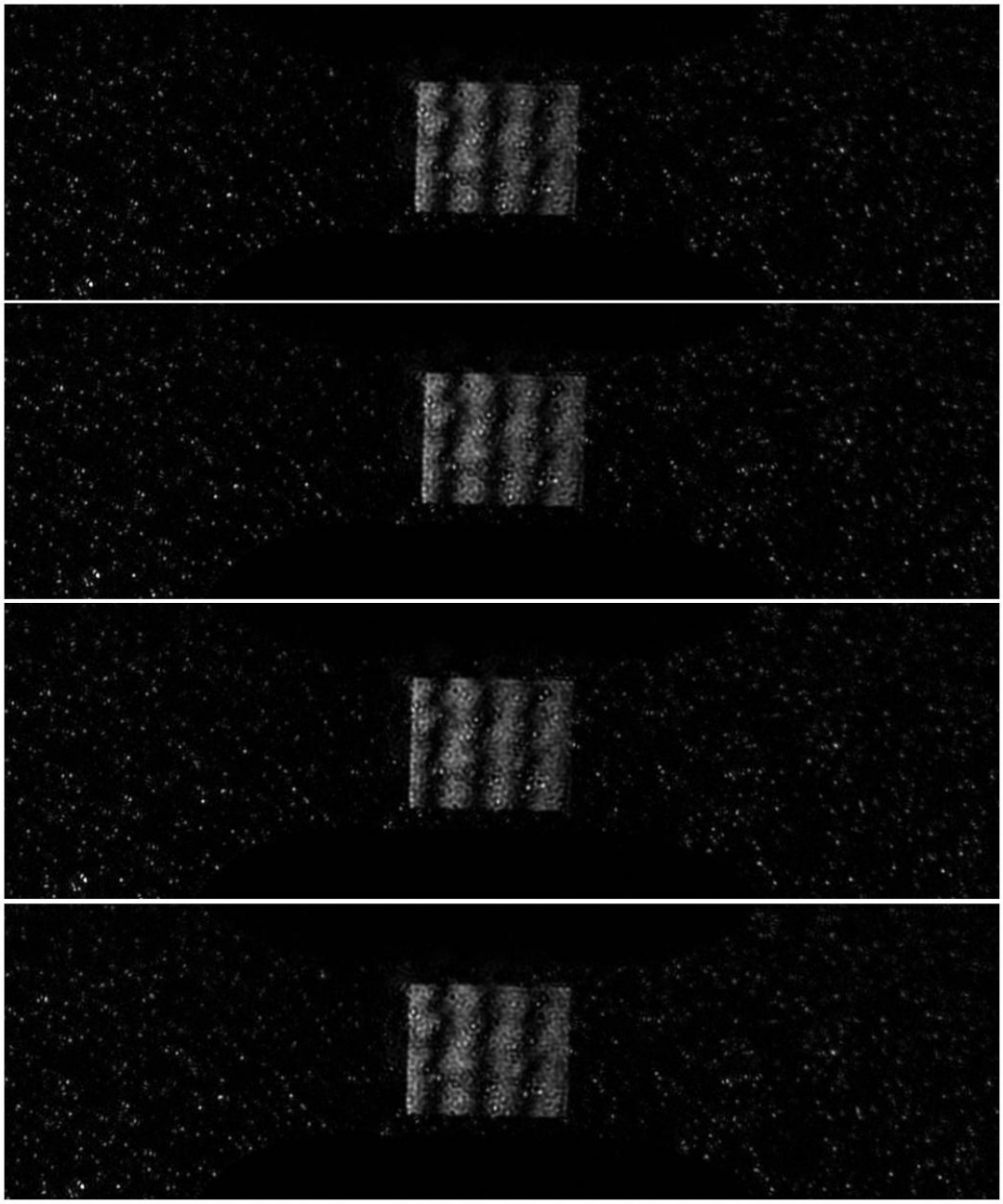

Figure 5-1- The vibration of interference fringes over time.

5.3 Continuous Wavelet Transformation

In contrary to the phase stepping method that requires three or more images of the same deformation field, wavelet transformations only need a single image. Therefore, they are not sensitive to mechanical vibrations or acoustic noise. Although they are more complex and computationally more expensive than Fourier transforms, wavelet transformations are better suited for phase extraction, especially in cases that the deformation field is nonuniform. In transforming the interferogram signal to frequency domain by Fourier transform, the time information is lost. In other words, the Fourier spectrum does not show where or when a frequency happened. However, in strain field measurements, it is necessary to know the exact coordinate of each frequency and hence the locations of each strain value. Wavelet Transforms have been developed to address this issue. In the following sections, the theory and background of the method is presented and the method is applied to simulated interferograms for uniform and nonuniform strain fields.

5.3.1 Theory

A wavelet is a function $\psi(x)$ that satisfies the admissibility condition such that [117]

$$\int_{-\infty}^{+\infty} \psi(x)dx = 0. \qquad \textbf{(5-5)}$$

This condition requires that the wavelet function to oscillate over a finite extent of time with zero mean and decays to zero. Therefore, the sine and cosine functions cannot be suitable for a wavelet function. In some well-known wavelets the admissibility condition is not completely satisfied but is sufficiently close to zero and result in negligible consequences. In the context of wavelet transformations, the function $\psi(x)$ that is obtained as such is called the mother wavelet. A family of wavelets is created by dilation and translation of the mother wavelet,

$$\psi_{a,b}(x) = \frac{1}{\sqrt{a}}\psi(\frac{x-b}{a}) \quad \textbf{(5-6)}$$

where $a > 0$ is the dilation parameter, also called the scale parameter, and b is the translation parameter and the factor $\frac{1}{\sqrt{a}}$ is added to equalize the energy of the dilated wavelet family. The choice of scale parameter depends on the range of the frequencies in the signal and translation parameter is in fact the spatial extent of the signal.

The Continuous Wavelet Transformation (CWT) of a function $f(x)$ is defined as [117]

$$\mathcal{W}_f(a,b) = \int_{-\infty}^{+\infty} f(x)\psi^*_{a,b}(x)dx \quad \textbf{(5-7)}$$

where * denoted the complex conjugate. From equation (5-6), it is trivial that the wavelet transform is the convolution integral of the function $f(x)$ and the wavelet function $\psi_{a,b}(x)$ over every scale parameter. This property enables the fast calculation of the wavelet transformation in Fourier domain and takes advantage of the sim-

plicity and efficiency of this procedure. A plot of the magnitude of $\mathcal{W}_f(a,b)$ is usually called the scalogram.

The wavelet that have found frequent application is the Morlet Wavelet,

$$\psi(x) = \frac{1}{\sqrt{\pi f_b}} \exp(2\pi i f_c x) \exp(-\frac{x^2}{f_b}) \quad \textbf{(5-8)}$$

where f_c is the center frequency and f_b is the bandwidth parameter of the mother wavelet. In order to satisfy the admissibility condition of equation (5-5), f_c should be set in the range of [0.80-0.95]. In this thesis the value of $f_c = 0.875$ is used with spatial variable x in μm. The wavelet is a combination of an oscillating term at center frequency of f_c and a Gaussian window with zero mean and variance of $\frac{f_b}{2}$. Figure 5-2 shows the real and imaginary parts of the complex mother Morlet wavelet.

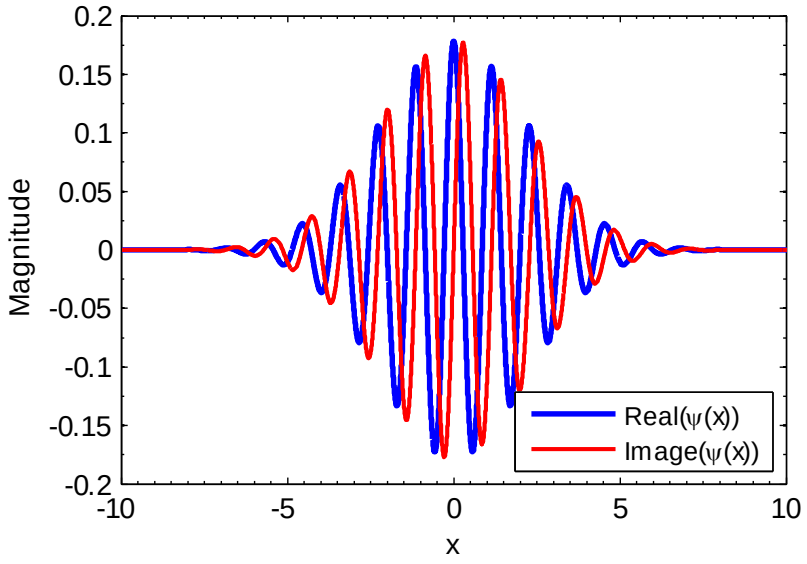

Figure 5-2- Morlet mother wavelet with $f_c = 0.875$ and $f_b = 10$.

From equations (5-6) and (5-8), the Morlet wavelet family can be re-written as

$$\psi_{a,b}(x) = \frac{1}{\sqrt{\pi a f_b}} \exp\left(2\pi i \frac{f_c}{a}(x-b)\right) \exp\left(-\frac{(x-b)^2}{a^2 f_b}\right). \quad \textbf{(5-9)}$$

This equation shows that the wavelet family is in fact a filter bank with different center frequencies of f_c/a and bandwidth governed by the scale parameter a. Wavelet filter bank is a constant-Q filter with constant energy spread at all scales. [117] The wavelet modulus is thus a measure of the energy density of the function $f(x)$ at each spatial position and frequency value. Figure 5-3 shows the magnitude of a few of these wavelets in the frequency domain.

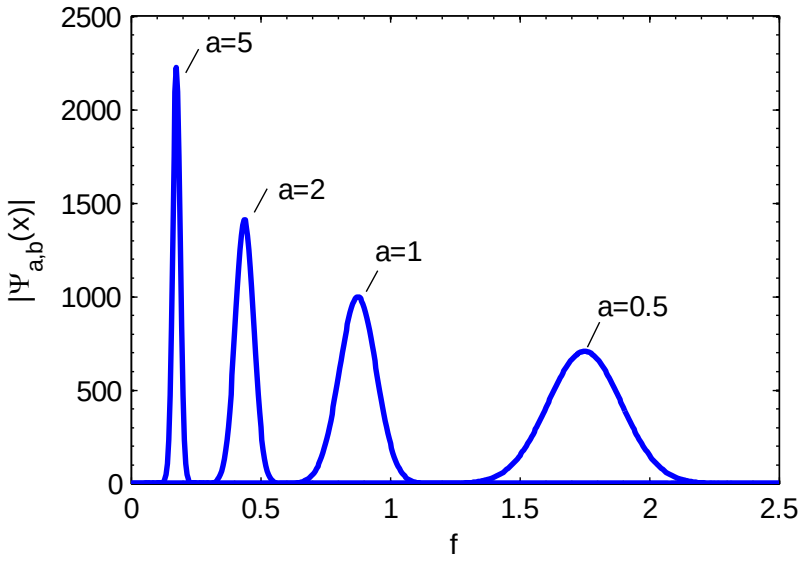

Figure 5-3- Frequency domain representation of Morlet wavelet family with different scale paramters *a* and *b=0*.

Delpart *et al* [118] showed that the instantaneous frequency of any signal is the corresponding frequency along the line of maximum wavelet modulus for every

spatial position in the scalogram of the signal. The line of maximum modulus is called the ridge of the signal. Their proof for this property of the wavelet ridge was mathematically complicated. Therefore, in this thesis a relatively simpler proof for the case of Morlet wavelet was provided and was used to better understand the affecting parameters on the accuracy and performance of the method. To prove this property, let $f(x) = \gamma(x)\cos\phi(x)$ be the oscillating component of intensity along a raw or a column of 2D interferogram and have a wavelet transform of

$$\mathcal{W}_f(a,b) = \int_{-\infty}^{+\infty} \gamma(x)\cos\phi(x)\,\psi^*_{a,b}(x)dx. \qquad \textbf{(5-10)}$$

For simplicity, let's assume

$$\psi^*_{a,b}(x) = h_a(x-b)\exp(-i\eta[x-b]) \qquad \textbf{(5-11)}$$

where for Morlet wavelet $h_a(x-b) = \frac{1}{\sqrt{\pi a f_b}}\exp(\frac{-(x-b)^2}{a^2 f_b})$ and $\eta = \frac{2\pi f_c}{a}$.

Equation (5-10) is then simplified to

$$\mathcal{W}_f(a,b) = \int_{-\infty}^{+\infty} \gamma(x)\cos\phi(x)h_a(x-b)\exp(-i\eta[x-b])dx. \qquad \textbf{(5-12)}$$

Substituting $\cos\phi(x) = \frac{1}{2}[\exp(i\phi(x)) + \exp(-i\phi(x))]$ into equation (5-12), and a subsequent change of variable $x \to x+b$ yields,

$$\begin{aligned}\mathcal{W}_f(a,b) = &\frac{1}{2}\int_{-\infty}^{+\infty} \gamma(x+b)h_a(x)\exp[i(\phi(x+b)-\eta x)]dx \\ &+\frac{1}{2}\int_{-\infty}^{+\infty} \gamma(x+b)h_a(x)\exp[i(-\phi(x+b)-\eta x)]dx\end{aligned} \qquad \textbf{(5-13)}$$

If γ and ϕ have small variations over the support of the wavelet, they can be expanded by the first order Taylor expansion,

$$\begin{aligned}\gamma(x+b) &\approx \gamma(b) + x\gamma'(b)\\ \phi(x+b) &\approx \phi(b) + x\phi'(b)\end{aligned} \tag{5-14}$$

Substituting equation (5-14) into equation (5-13) yields

$$\begin{aligned}\mathcal{W}_f(a,b) = \frac{1}{2}\ \exp(i\phi(b)) \int_{-\infty}^{+\infty} \gamma(b) h_a(x) \exp[ix(\phi'(b) - \eta)]dx \\ + \frac{1}{2}\exp\big(i\phi(b)\big) \int_{-\infty}^{+\infty} x\gamma'(b) h_a(x) \exp[ix(\phi'(b) - \ \eta)]dx \\ + \frac{1}{2}\exp\big(-i\phi(b)\big) \int_{-\infty}^{+\infty} \gamma(b) h_a(x) \exp[-ix(\phi'(b) + \ \eta)]dx \\ + \frac{1}{2}\exp\big(-i\phi(b)\big) \int_{-\infty}^{+\infty} x\gamma'(b) h_a(x) \exp[-ix(\phi'(b) + \ \eta)]dx\end{aligned} \tag{5-15}$$

Now, let's evaluate the terms of equation (5-15). By definition,

$$\int_{-\infty}^{+\infty} h_a(x) \exp[-ix(\phi'(b) + \eta)]dx = \sqrt{a}\, H[a(\phi'(b) + \eta)] \tag{5-16}$$

where $H(\omega)$ is the Fourier transform of $h_a(x)$. If $\Delta\omega$ is the bandwidth of $H(\omega)$ and $\eta \geq \frac{\Delta\omega}{a}$, for $\phi'(b) \geq \frac{\Delta\omega}{a}$

$$H[a(\phi'(b) + \eta)] \ll 1. \tag{5-17}$$

Therefore, terms three and four of equation (5-15) become negligible. On the other hand,

$$\int_{-\infty}^{+\infty} h_a(x)\exp[ix(\phi'(b)-\eta)]dx = \sqrt{a}\,H[-a(\phi'(b)-\eta)]. \quad \textbf{(5-18)}$$

Since $|H(\omega)|$ is maximum at $\omega = 0$, the modulus of the wavelet transform $|\mathcal{W}_f(a,b)|$ will be maximum at points $\phi'(b) = \eta(b)$. These points for which wavelet modulus is maximum are called wavelet ridge and the instantaneous frequency at each point $\phi'(b)$ is equal to the corresponding frequency $\eta(b) = \frac{2\pi f_c}{a_r(b)}$. Therefore, from equation (5-3)

$$\begin{aligned}\epsilon_{xx}(x) &= \frac{1}{4\pi f_s}\frac{\partial\phi(x)}{\partial x} \\ &= \frac{1}{2f_s}\frac{f_c}{a_r(x)}\end{aligned} \quad \textbf{(5-19)}$$

where $a_r(x)$ is the scale value on the ridge of the wavelet for any coordinate x. From equation (3-2), the displacement field can be calculated by

$$U(x) = \int_0^x \epsilon_{xx}(x)dx. \quad \textbf{(5-20)}$$

However, by integration the error is accumulated causing larger deviation in displacement field as the gage length is increased. Zhong *et al* [119] showed that the phase of an interferogram, and hence the displacement field in our application, can be directly retrieved from the phase of the wavelet transform at its ridge points. Therefore,

$$U(x) = \angle\mathcal{W}_f(a_r(x),x) \quad \textbf{(5-21)}$$

where

$$\angle \mathcal{W}_f(a_r(x), x) = \arctan \frac{image\left(\mathcal{W}_f(a_r(x), x)\right)}{real\left(\mathcal{W}_f(a_r(x), x)\right)}. \quad \textbf{(5-22)}$$

Although, the above formulation has been developed for a one-dimensional signal, it can be extended for two dimensional displacement field $U(x, y)$ and strain field $\epsilon_{xx}(x, y)$ by analyzing every row or column of the interferogram data.

In order to evaluate the accuracy of the wavelet transformation for strain measurement, this method was tested on simulated deformation fields. Uniform and non-uniform fields were simulated and the results are presented in the following sections. With uniform fields, the strain resolution of the method can be evaluated, while on nonuniform deformation field the spatial resolution can be investigated.

5.3.2 Uniform Deformation

In the case of tensile testing, the deformation field in the specimen is uniform, i.e. the strain value across the gage length is constant and the deformation field is a linear function of gage length except for the necking and post-necking part of the test that the deformation becomes localized and nonuniform. Therefore, for the uniform part of the tensile test, the displacement along the loading axis and perpendicular to grating axis is

$$U(x, y) = \epsilon_{xx} x \quad \textbf{(5-23)}$$

where ϵ_{xx} is constant. From equations (5-1) and (5-2), the 2D interferogram is

$$I(x,y) = I_0(x,y) + \gamma\,(x,y)\cos[\,2\pi(2f_s\epsilon_{xx} + m)\,x] \quad \textbf{(5-24)}$$

where m is the carrier fringe frequency and in this simulation $I_0(x,y) = 1$, $\gamma(x,y) = 1$, $f_s = \frac{1}{0.760}\frac{l}{\mu m}$ and $m = 0.08\frac{1}{\mu m}$. These values were chosen based on or close to the real experiments and specimen geometries in the current thesis to better simulate the process. The gage length x was 100μm long and was discretized based on the CCD pixel size and magnification with step size $\Delta x = 0.3\ \mu m$.

The range of strain that usually happens in tensile testing of metallic materials is 10^{-5} to 2×10^{-1} strains. Figure 5-4 shows the corresponding simulated interferograms for six strain values in this range. It is obvious that up to a strain value of about 0.1%, the frequency of the fringe lines is almost visually constant and equals the frequency of the carrier fringes. There are many reasons to use carrier fringes in the moiré interferometry measurements. First, a slight misalignment in the optical setup or a discrepancy between the required angle of incident beam and the actual angle may result in carrier fringes. Second, when carrier fringes are added to the interferogram, from equation (5-24), it can be seen that the frequency content of the interferogram data increases. This increase in the frequency value, increases the accuracy of the Fourier transform and hence the accuracy of the wavelet transformation in finding the local strains. Third, regardless of the sign of the strain, the equation (5-24) results in the same interferogram if the carrier frequency is zero, i.e. the compressive and tensile strains have the same interferogram data. An *a priori* knowledge of the fringe carrier frequency *m* can help to solve this sign ambiguity. If the carrier frequency is

positive, positive strains will increase the total frequency while negative strains will decrease. On the other hand, presence of carrier fringes helps the alignment of the fringe image before loading the specimen. Therefore, a known carrier fringe is intentionally added to the interferogram by changing the angle of incident of the laser beams to a value other than the one required by equation (3-5). The chosen carrier frequency should be high enough to provide enough oscillations over the spatial extent of the interferogram and should be low enough not to violate the Nyquist sampling criterion. Since in this thesis, a carrier fringe frequency of 8 to 10 lines per 100μm was usually adjusted visually by tuning the setup, in the current simulations a carrier frequency *m* of 0.08 was used.

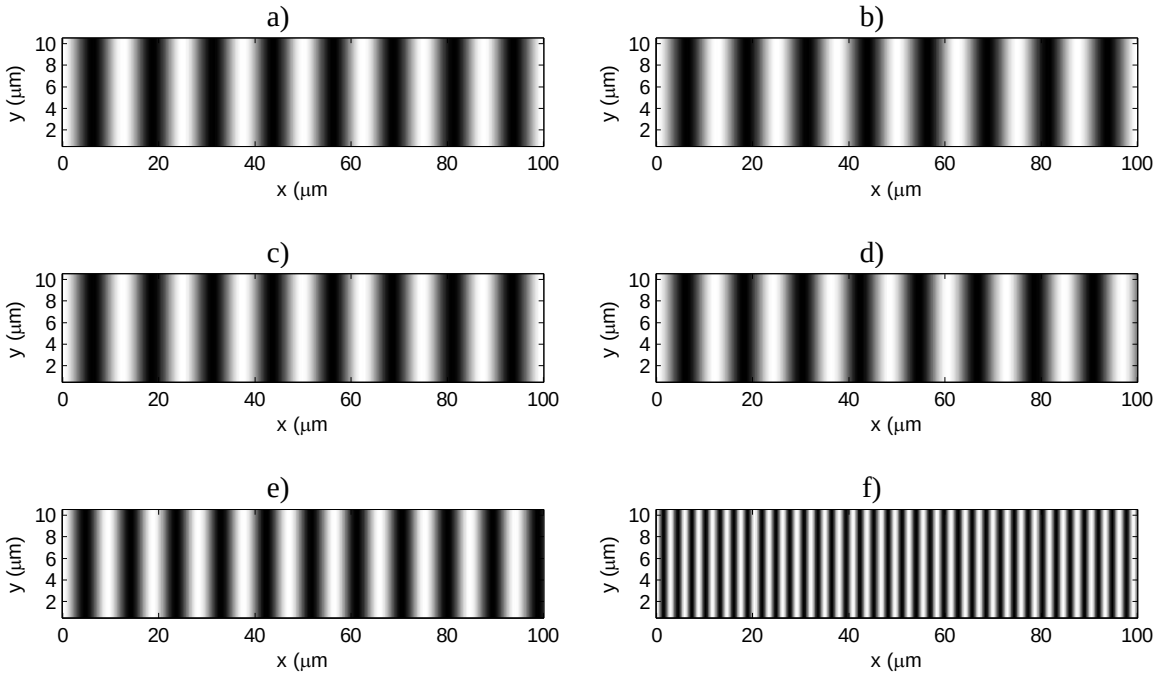

Figure 5-4- Simulated interferograms for the strain values a) 0, b) 10^{-5}, c) 10^{-4},d) 10^{-3}, e) 10^{-2}, f) 10^{-1} for *m*=0.08.

The simulated data were used to adjust the wavelet parameters. Center frequency f_c, bandwidth parameter f_b, and range and step size of the scale *a* have to be adjusted. On the other, some other parameters like the extent of *x* for the calculation of wavelet family, number of points required for Fast Fourier Transform, and the effect of noise level on the accuracy of the method were investigated through the simulated interferograms.

The main four steps that have to be followed to extract the strain information from the interferogram data are shown in Figure 5-5. In the first step, the frequency of the carrier fringes is estimated visually by counting the number of fringe lines in the gage length. From equations (5-19) and (5-20), the corresponding scale to a strain value and a carrier frequency is

$$a = \frac{f_c}{2f_s\epsilon_{xx} + m}. \tag{5-25}$$

Knowing that the strain value is zero in the first interferogram image, a range of *a* can be set by choosing an arbitrary domain with central value of $\frac{f_c}{m}$. The domain has to be discretized to a fine step size in order to be able to precisely calculate the exact carrier frequency. In step 2, the wavelet transform of the carrier fringe is found by the convolution integral equation (5-7) and the exact value for the carrier frequency is found. In order to discretize the scale parameter, a new discretization scheme has been proposed to accurately control the level of the required strain error. In step 3, the strain range is discretized such that

$$\epsilon_{xx}(i+1) = \epsilon_{xx}(i) \times (1 + \frac{\Delta\epsilon}{\epsilon}) \quad \textbf{(5-26)}$$

for the strain range -1×10^{-4} to 5×10^{-1}. This strain range can also be adjusted from *a priori* knowledge of the range of strain in the experiment. From equation (5-25), the corresponding scale parameters to the strain range obtained from equation (5-26) is reconstructed. Scale parameters obtained as such will assure that the extracted scales on the ridge of the wavelet will result in strains that have $\frac{\Delta\epsilon}{\epsilon}$ relative error. For a strain range that extends for a four order of magnitude, this method of discretization makes the number of scales within a reasonable limit. Depending on the importance of the accuracy or computation speed the relative error $\frac{\Delta\epsilon}{\epsilon}$ can be adjusted. For most of the calculations in this thesis $\frac{\Delta\epsilon}{\epsilon} = 10\%$.

Based on the new range for scale parameter, the wavelet transformation of each interferogram data is calculated and the strain information is extracted. By calculating the carrier interferogram first and subtracting it from strained interferograms, the effect of phase error is also reduced.

The above process flow for interferogram simulation and the proceeding strain extraction calculations was implemented in MATLAB. In order to choose the best post-processing parameters, the effect of each parameter is discussed in detail as follows.

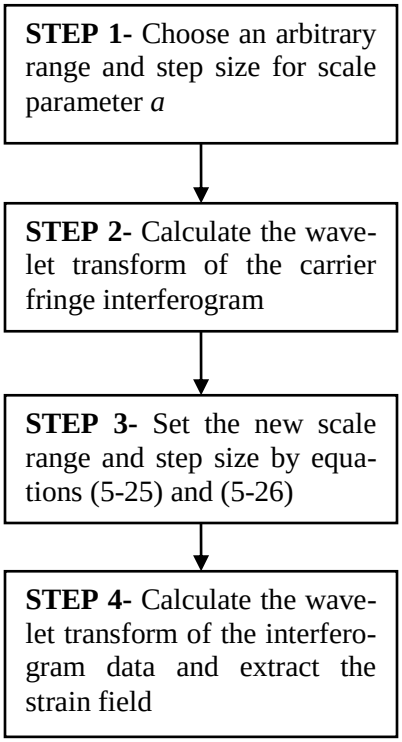

Figure 5-5- Calculation steps for extracting the strain field from interferogram data by wavelet transform.

The first parameter to choose is the center frequency f_c of the wavelet transform. This parameter, as it was discussed earlier, is bounded and, therefore, the value of $f_c = 0.875$ was used throughout this thesis.[1]

The effect of bandwidth parameter f_b on the accuracy of the method is shown in Figure 5-6 and Figure 5-7. It can be clearly seen that by increasing the bandwidth para-

[1] The original Morlet wavelet that was introduced in [120] has a few more terms that with the assumption of $2\pi f_c > 5$ those terms can be neglected and the Morlet wavelet is simplified to the form presented in equation (5-8). However, in most of the contemporary literature, the form of equation (5-8) is presented as the Morlet wavelet with a bound on the central frequency. Therefore, the bound of $0.8 < f_c < 0.95$ does not necessarily comes from only the admissibility condition and other values of f_c may satisfy the admissibility condition of equation (5-5) for the Morlet wavelet presented in this thesis.

meter, the relative error of the calculated strain falls below 5%. f_b is in fact the parameter that controls the spatial and frequency spread of the wavelet family. In other words, it controls the spatial resolution and strain resolution of the post-processing. The higher values for f_b result in a more spatial spread, which based on the Fourier uncertainty principle, it results in a higher strain resolution. In other words, strain accuracy and spatial localization cannot be obtained at the same time. On the other hand, for higher values of scale parameter *a*, the wavelet spread over time is increased. Since the scale parameter is inversely proportional to the strain values, it implies that lower strain values have lower spatial resolution, while they have higher strain accuracy. The effect of f_b on spatial resolution is discussed in more details in section 5.3.3.

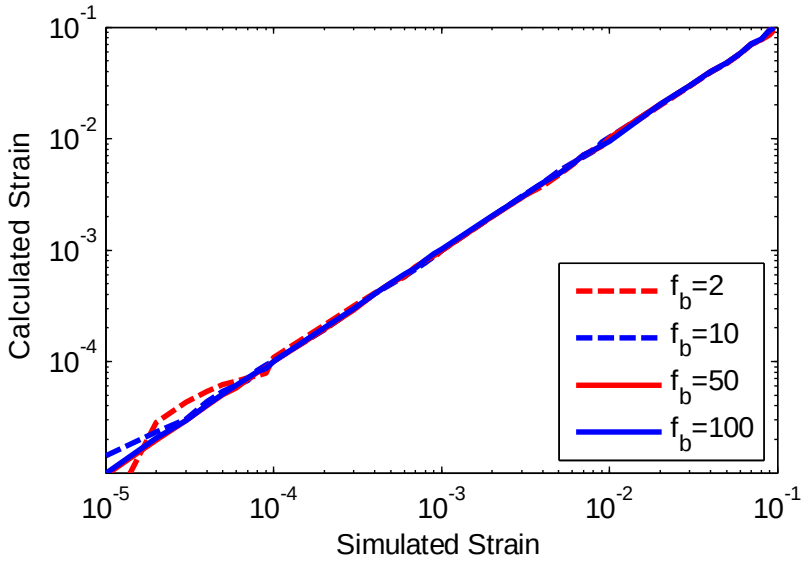

Figure 5-6- Effect of f_b on the accurcy of the calculated strain values.

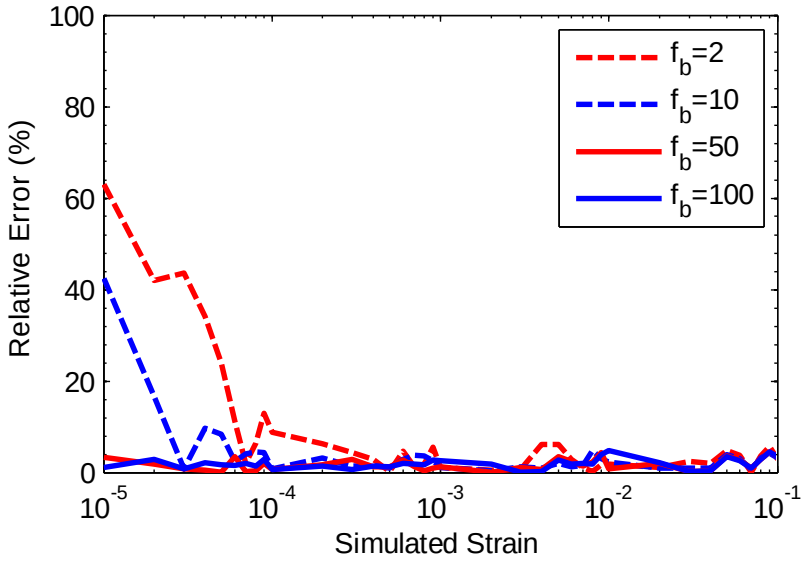

Figure 5-7- Effect of f_b on the relative error in calculated strain values.

Another important parameter is the $\frac{\Delta\epsilon}{\epsilon}$ parameter that was used to discretize the scale parameter *a*. As it is shown in Figure 5-10, the relative error in the simulated strain value is substantially decreased from 5% to less than 1% by changing this parameter from 0.1 to 0.01. However, at the same time, the computation time was increased by almost 12 folds. Depending on the required accuracy and the tolerable computation cost, the parameter $\frac{\Delta\epsilon}{\epsilon}$ can be adjusted. For most of the simulations in this thesis and specifically for comparative simulations, the value of 0.1 was used and the reported relative errors in strain calculations are based on this assumption. Figure 5-8 shows the wavelet modulus that was achieved by the arbitrary choice of scale parameter in step 1 and Figure 5-9 shows the modulus that is calculated based on the proposed discretization scheme.

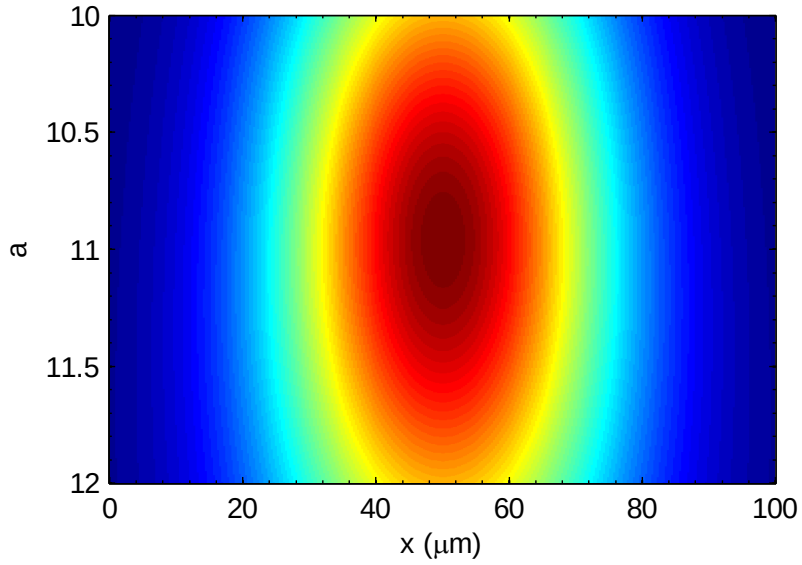

Figure 5-8- The wavelet modulus based on the arbitrary choice of scale parameter *a*.

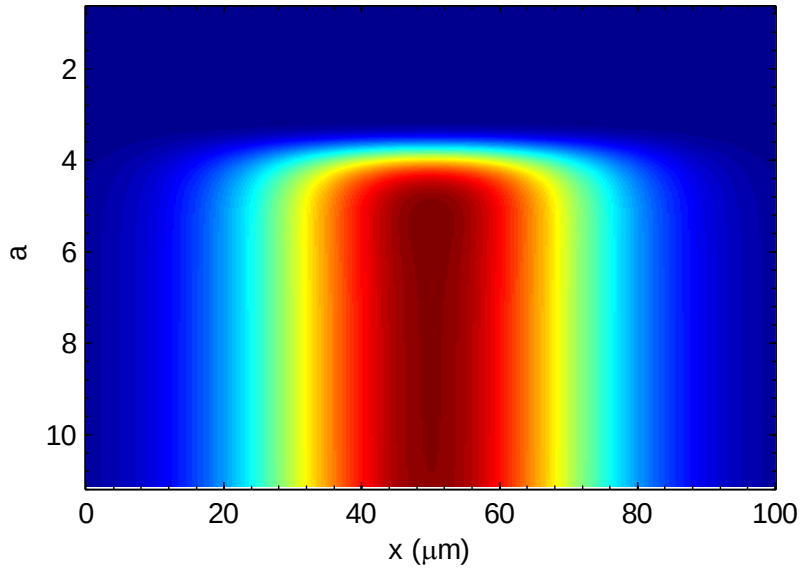

Figure 5-9- The wavelet modulus based on the proposed discretization scheme.

An inherent property of any experimental data is the noise and therefore its effect on the accuracy of the postprocessing method has to be evaluated. This noise

may come from the scattered light, the surface roughness, a misalignment in the optical setup, and the electrical CCD noise and the dark current.

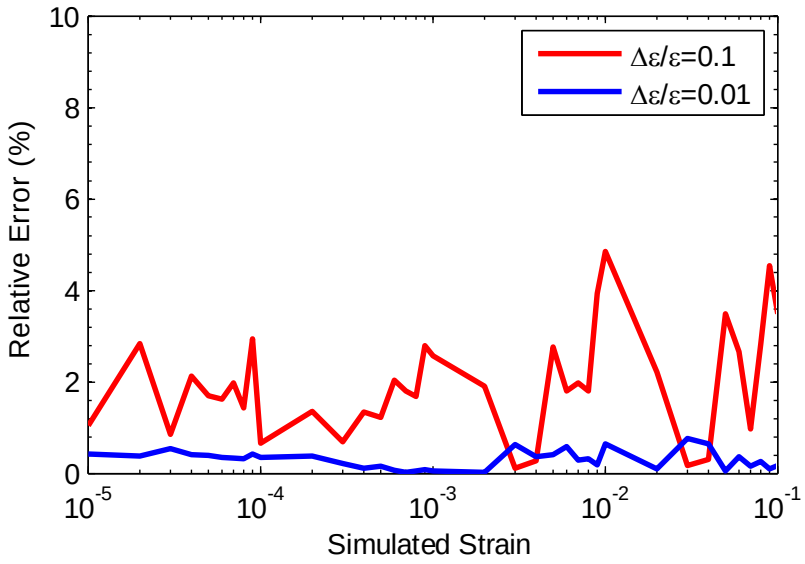

Figure 5-10- Effect of scale discretization parameter $\frac{\Delta\epsilon}{\epsilon}$ on the relative error in calculated strain values.

In section 5.3.1, it was shown that the scale parameter at the wavelet ridge is only affected by the instantaneous frequency of the sine or cosine wave. Therefore, the wavelet transform and respective wavelet ridge detection should inherently denoise the interferogram. To evaluate this characteristic, additive random noise with different noise amplitudes were added to the background intensity $I_0(x,y)$, the visibility $\gamma(x,y)$, and the phase $\phi(x,y)$ of equation (5-24), such that

$$I(x,y) = [1 + n_I w_n] + [1 + n_\gamma w_n] \cos\left[2\pi(2f_s\epsilon_{xx} + m)x + \frac{2\pi}{\lambda} n_\phi w_n\right] \qquad \textbf{(5-27)}$$

where w_n is a random white noise on the [-1,1] interval and n_I, n_γ, and n_ϕ are the amplitudes of the background noise, visibility noise, and phase noise, respectively, and $I_0(x,y)$ and $\gamma(x,y)$ were assumed to be unity. Therefore, noise amplitudes n_I, n_γ, and n_ϕ are a good representation of the signal to noise ratio (SNR).

Figure 5-11 and Figure 5-12 show the effect of background noise amplitude n_I on the accuracy of the wavelet transform. Even at very low SNR values, i,e, $n_I = 1$, the wavelet transform can reconstruct the signal with acceptable error. This error, as it was stated earlier, can be reduced by the choice of scale discretization parameter $\frac{\Delta\epsilon}{\epsilon}$. The background noise may come from many different sources and they do exist in the recorded interferograms in real experiments. Ambient light, CCD dark current, scattered rays from the setup, and scattered light from the surface features of the specimen are the important causes of the background noise. Ambient light noise was filtered by using a laser line bad-pass filter at the CCD aperture. The effect of CCD dark current can be suppressed by using the thermoelectric cooler of the CCD camera, decreasing the exposure time, and increasing the laser power. Scattered light from the setup can also be cancelled by using dark non-reflecting materials. The most important source of background noise is the surface roughness of the specimen which cannot be removed, because it is an inherent characteristic of the material under study. However, as it is shown in these simulations, the de-noising capability of the strain extraction algorithm is so high that even at very high background noise levels, the strain can be calculated with high accuracy.

However, if the additive is noise is added to the visibility of the interferogram waveform, the scale discretization parameter $\frac{\Delta\epsilon}{\epsilon}$ cannot be as effective. As shown in Figure 5-13 and Figure 5-14, the effect of same level of noise in visibility is higher than the same level of noise in background intensity. The main reason is that the visibility noise is not an additive white noise for the signal and hence the noise is correlated to the signal. In physical sense, the amount of this noise is almost negligible. The reason is that visibility, from equation (3-9), is resulted from the amplitude of the two incident beams. In practice, the intensity noise in the laser beam that was used in this thesis was below 1% [121] which corresponds to $n_\gamma \approx 0.01$, which is well below the noise level that can be de-noised by the wavelet transform, as shown in Figure 5-14. Therefore, the effect of n_γ can be neglected in the current application.

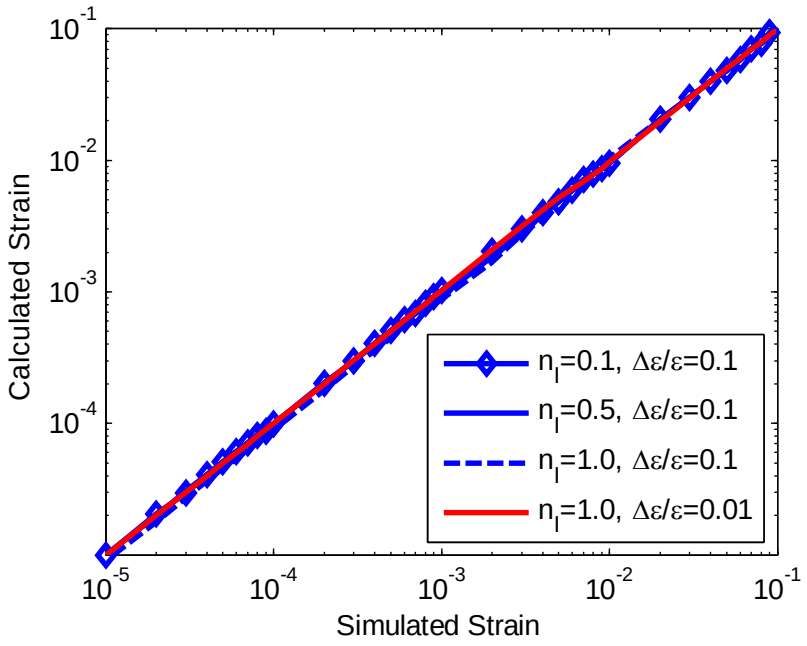

Figure 5-11- Effect of background noise amplitude n_I and scale discretization parameter $\frac{\Delta\epsilon}{\epsilon}$ on the accuracy of the calculated strain value.

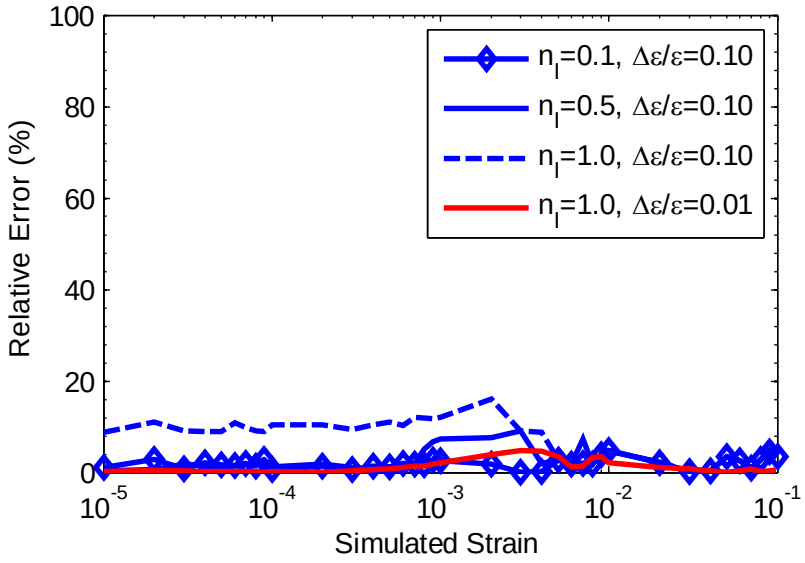

Figure 5-12- Effect of background noise amplitude n_I and scale discretization parameter $\frac{\Delta\epsilon}{\epsilon}$ on the relative error in the calculated strain value.

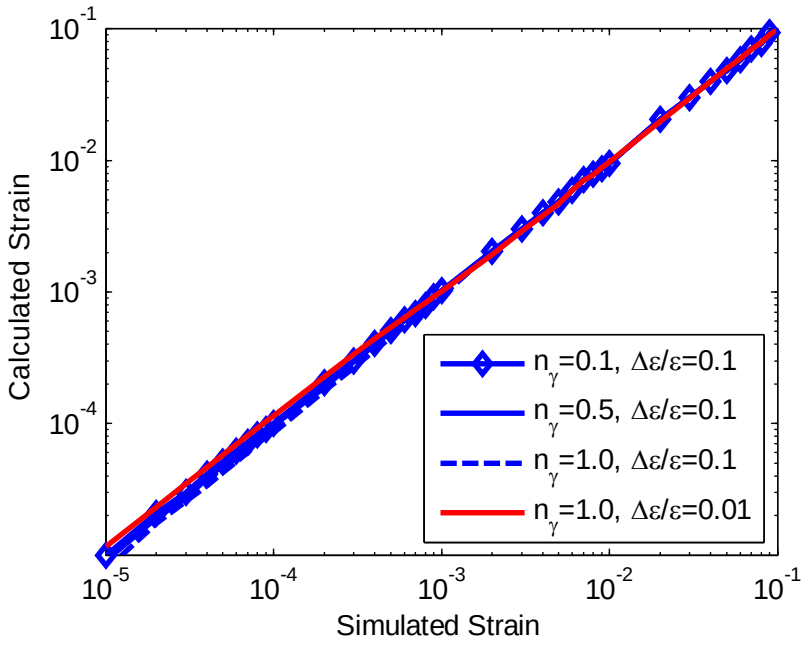

Figure 5-13- Effect of visibility noise amplitude n_γ and scale discretization parameter $\frac{\Delta\epsilon}{\epsilon}$ on the relative error in the calculated strain value.

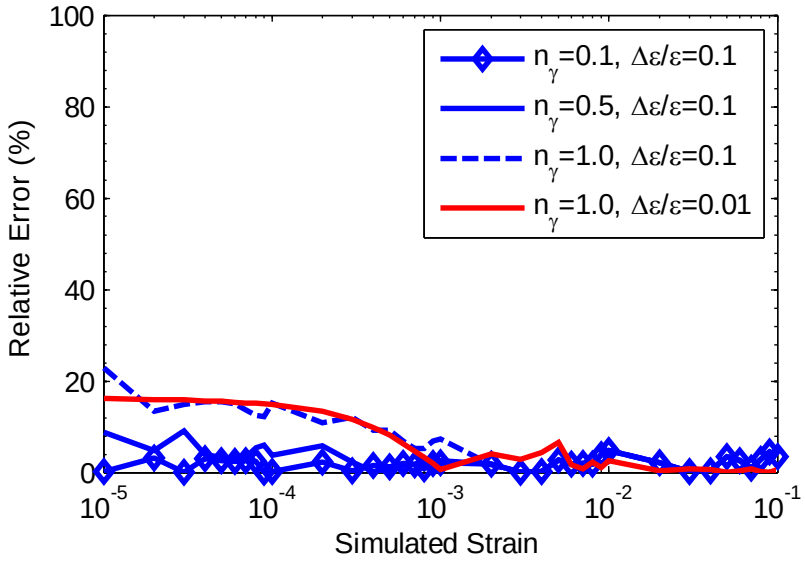

Figure 5-14- Effect of visibility noise amplitude n_γ and scale discretization parameter $\frac{\Delta\epsilon}{\epsilon}$ on the relative error in the calculated strain value.

Figure 5-15 and Figure 5-16 show the effect of phase noise amplitude n_ϕ on the accuracy of the extraction algorithm. The range of the phase noise amplitude is chosen based on the deviations in optical path that might be induced by the optical flatness of the optical setup. Most of the optical elements that were used in this thesis, like mirrors and beam splitters have flatness of $\frac{\lambda}{10}$ or better. This means that the amount of warpage that is induced in the laser beam is within $\frac{\lambda}{10}$. This assumption is the worst case scenario because only small regions of each element at the size of the specimen grating area was used and within this area the devotions are much smaller. Even at this level of phase error, the simulated interferograms show that the strain extraction algorithm can extract the strain values at a satisfactory relative error. Note that the optical flatness and wavefront warpage level is two times the value of n_ϕ.

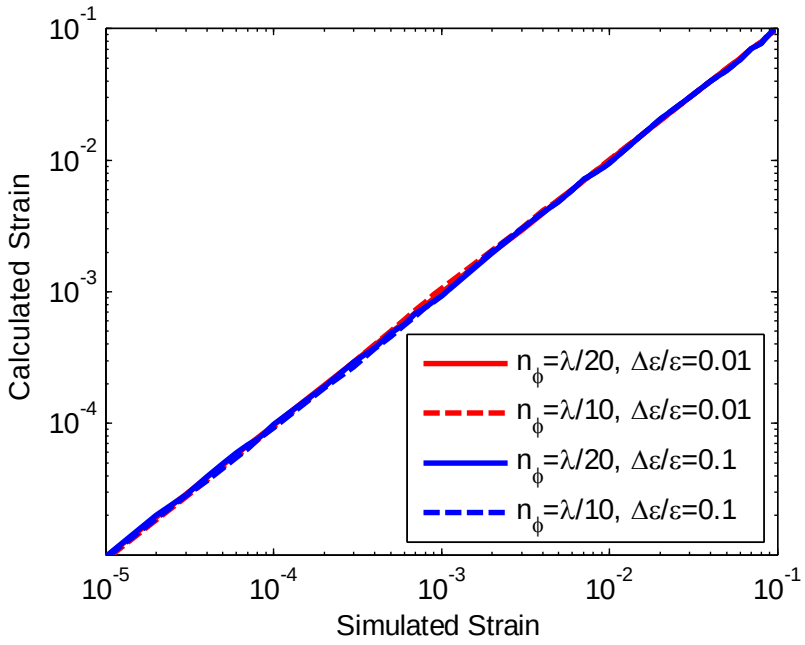

Figure 5-15- Effect of phase noise amplitude n_ϕ and scale discretization parameter $\frac{\Delta\epsilon}{\epsilon}$ on the accuracy of the calculated strain value.

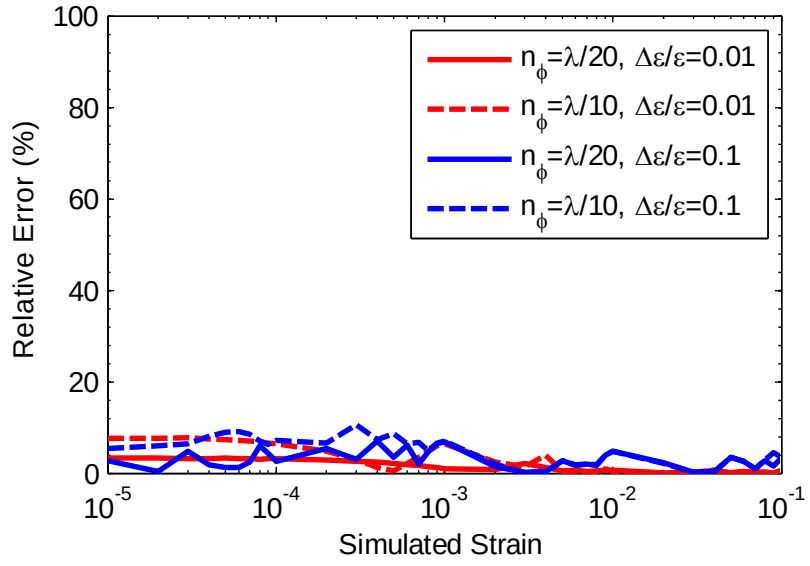

Figure 5-16- Effect of phase noise amplitude n_ϕ and scale discretization parameter $\frac{\Delta\epsilon}{\epsilon}$ on the relative error in the calculated strain value.

In order to show the efficiency of the strain extraction algorithm that was used in this thesis in de-noising the 2-D interferogram, the corresponding interferogram image to the strain value of 5×10^{-5} was simulated with background noise amplitude $n_I = 1$ and phase noise amplitude $n_\phi = \frac{\lambda}{10}$. Figure 5-17 shows the reconstructed 2-D interferogram. The 2-D interferogram was reconstructed by processing 1-D signals corresponding to each row. In order to extract the phase of the interferogram signal, the method presented in equation (5-20) was used. Since this equation uses the phase of the wavelet transform and this phase is in the interval [-π π], the extracted phase for the interferogram is modulo 2π. Therefore, a phase unwrapping procedure is required if one is interested in the displacement field. Figure 5-18 shows the original and reconstructed interferogram signal at middle row corresponding to locations y=5μm.

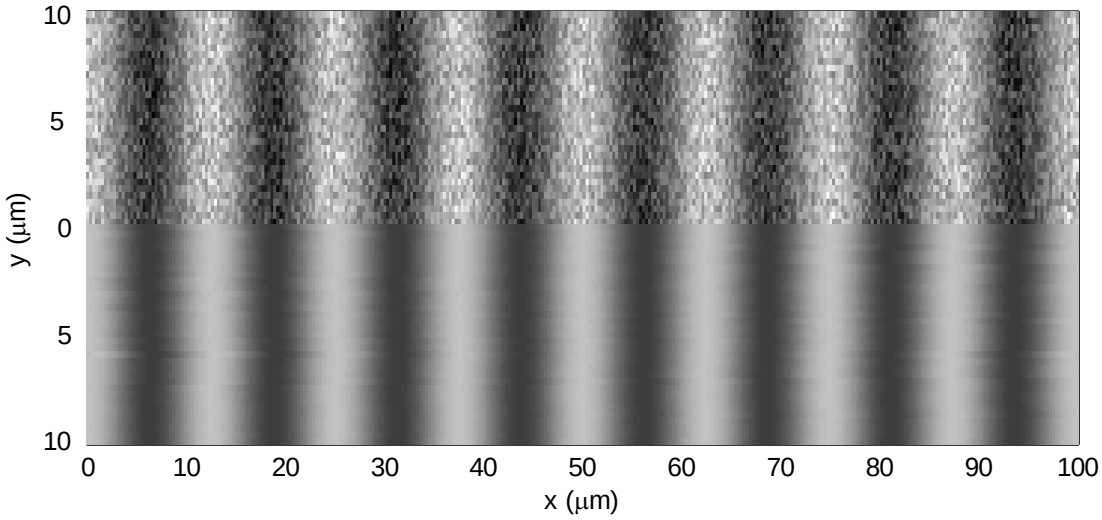

Figure 5-17- Original (top) and reconstructed (bottom) 2-D interferogram images corresponding to 50μstrains and noise level $n_I = 1$ and $n_\phi = \frac{\lambda}{10}$.

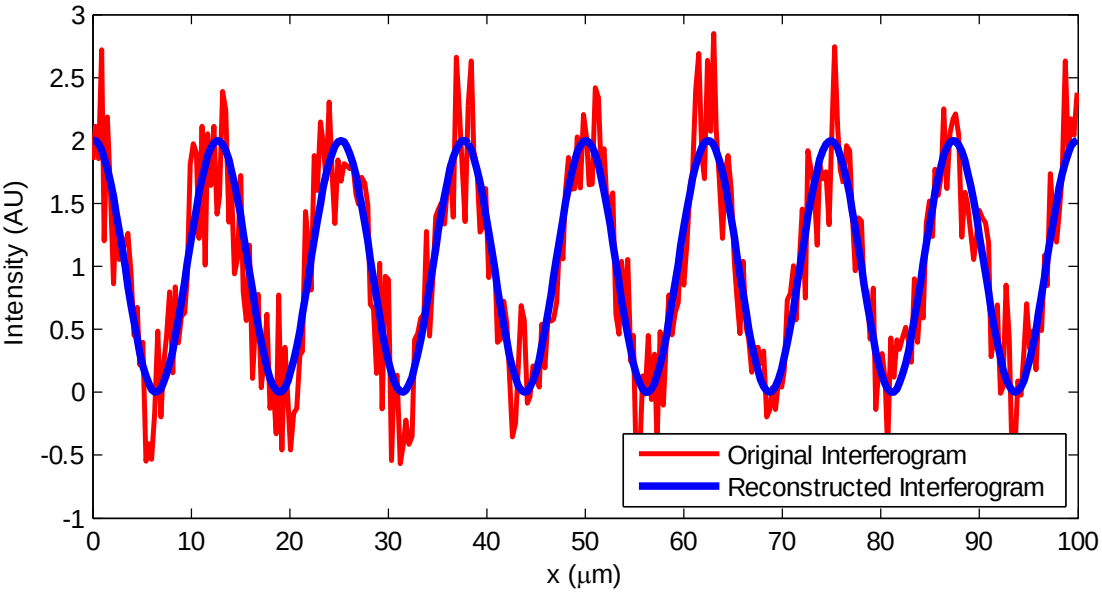

Figure 5-18- Original and reconstructed interferogram of Figure 5-17 at y=5μm.

5.3.3 Nonuniform Deformation

An advantage of the moiré interferometry over other interferometry and strain measurement methods is the ability of this method to measure strain and displacement field rather just a strain value across the gage length. Therefore, the wavelet transformations were used in this thesis to extract the strain field from moiré interferogram images. In this section the capability of wavelet transformations and ridge detection algorithm discussed in sections 5.3.1 and 5.3.2 are evaluated.

In order to simulate a nonuniform strain field and evaluate the strain extraction algorithm on it, the analytic solution to the strain filed in an infinite plate with a circular hole under uniaxial tension was used. Boundary conditions and the problem geometry are shown in Figure 5-19. For this classic problem, the displacement filed in polar coordinates is given by [122]

$$u_r = \frac{\sigma(1+\nu)}{2Er}\left[\frac{1-\nu}{1+\nu}r^2 + a^2 + \left(\frac{4a^2}{1+\nu} + r^2 - \frac{a^4}{r^2}\right)\cos 2\theta\right] \quad \textbf{(5-28)}$$

$$u_\theta = -\frac{\sigma(1+\nu)}{2Er}\left(\frac{1-\nu}{1+\nu}2a^2 + r^2 + \frac{a^4}{r^2}\right)\sin 2\theta \quad \textbf{(5-29)}$$

where σ is stress, a is the hole radius, and E and ν are the Young's modulus and Poisson's ratio of the material, respectively. The displacement field and normal strain field along the x-axis for the x and y interval [-50,50] μm and a 10μm radius circular hole are shown in Figure 5-20. The material properties of Aluminum were used (E=70GPa and ν=0.3) and stress is set to 10MPa.

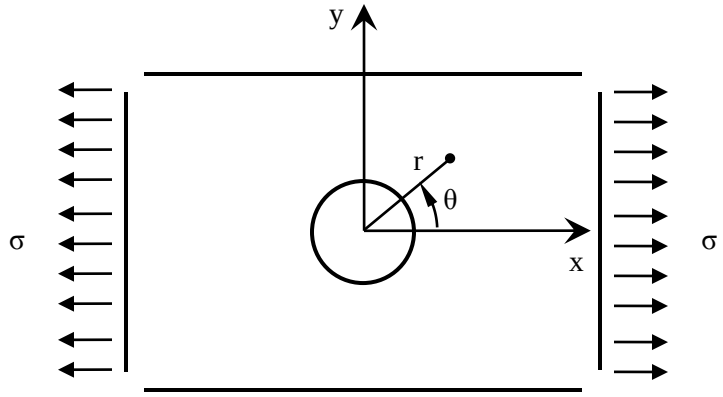

Figure 5-19- Schematic representation of the boundary conditions and the geometry of an infinite plane with circular hole under uniaxial tension.

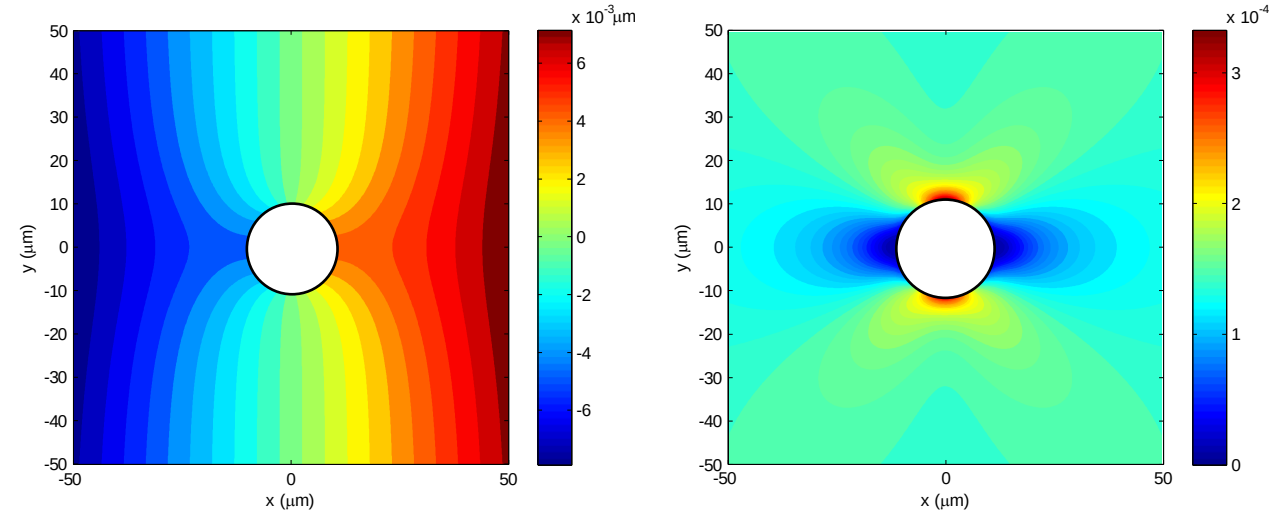

(a) (b)

Figure 5-20- Displacement (a) and normal strain (b) fields along the x-axis for geometry of Figure 5-19.

In order to evaluate the strain extraction algorithm, the strain data along the line y=12µm was used. (Figure 5-21) The sharp variations of strain across this coordinate helps better evaluate the capabilities of the method in extracting instantaneous

frequencies of the moiré interferogram and hence the local strain values. As it was discussed earlier in this thesis, the best simultaneous strain resolution and spatial resolution for the Morlet wavelet is achieved at variance of unity. This requires that the $a^2 f_b$ value is in the vicinity of 2. With this assumption the spatial and frequency spread of the wavelet family will be about the same, resulting in the best localization and resolution possible.

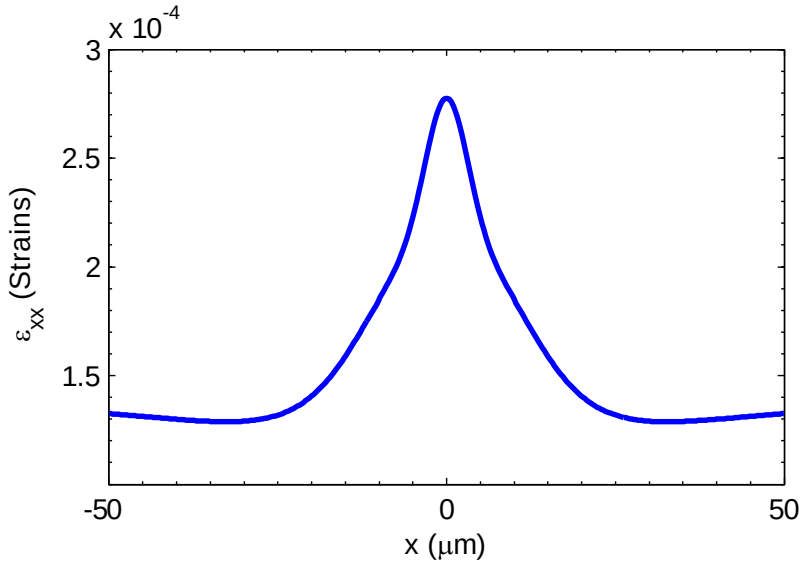

Figure 5-21- ϵ_{xx} across the line y=12μm for the simulated strain field of Figure 5-20-b.

Values of scale parameter *a*, on the other hand, are dependent upon the choice of center frequency f_c and the range of strains under study. From equation (5-25)

$$\frac{f_c}{a} = 2 f_s \epsilon_{xx} + m. \qquad \textbf{(5-30)}$$

Since the range of strain values are constant for almost all strain measurement applications and f_c was chosen based on the conventional admissibility condition, the

parameter that controls the range of scale parameters is carrier frequency *m*. The advantage of this parameter is that it can be adjusted by tuning the experimental setup and the corresponding optical elements, as discussed in 3.3.2. A good choice of interval for scale parameters is the range that for all of the wavelet family, the variance remains in the vicinity of two. Since the variation of the first term on the right hand side of equation (5-30) for the strain interval 10^{-5} to 2×10^{-1} is very small, a good choice for m can be such that $\frac{f_c}{a} = m$ and $a \approx 1$. This results in a choice of $m \approx f_c$. For the case of this thesis, the value of carrier frequency can be set to 0.8, ten times the carrier frequency that was used for uniform deformations in the previous section. The scale parameter interval will, therefore, be [0.4-1.1].

Figure 5-22 and Figure 5-23 show the reconstructed strain field for line y=12μm with *m*=0.08 and *m*=0.8, respectively. As it can be seen in these figures, the reconstructed strain with higher carrier fringe frequency could better localize the strain values and the relative error was below 5% in this case. On the other hand, due to the higher spatial spread of the case of *m*=0.08, the strain values were "averaged" over the special extent of the signal. As it is presented in these figures, the wavelet transformation does not reveal accurate results at the edges of the signal extent. This discrepancy is due to the fact that the signal is finite and the transformation is calculated over an infinite extent.

Figure 5-24 and Figure 5-25 show the accuracy of the algorithm for two other orders of strain, namely 10^{-5} and 10^{-3}, respectively.

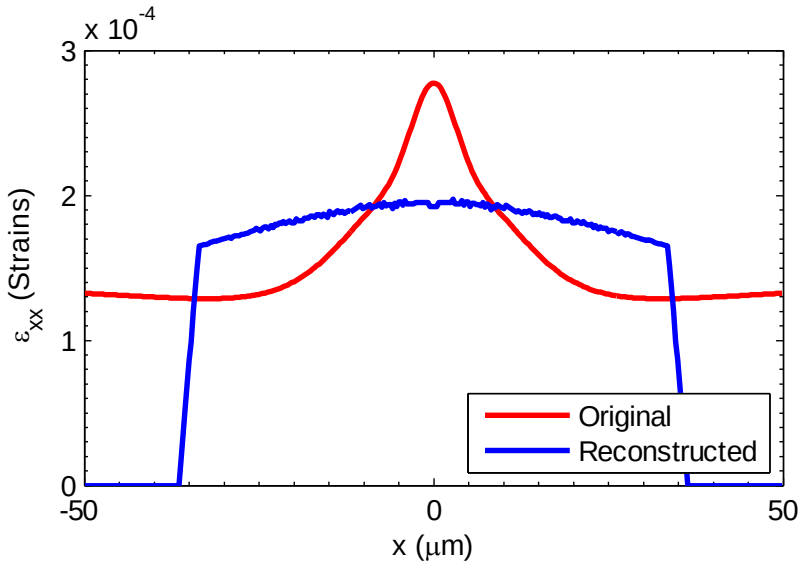

Figure 5-22- The reconstructed strain field at y=12μm with carrier frequency m=0.08, f_b=5, and $\frac{\Delta\epsilon}{\epsilon}$=0.5% and strain order 10^{-4}.

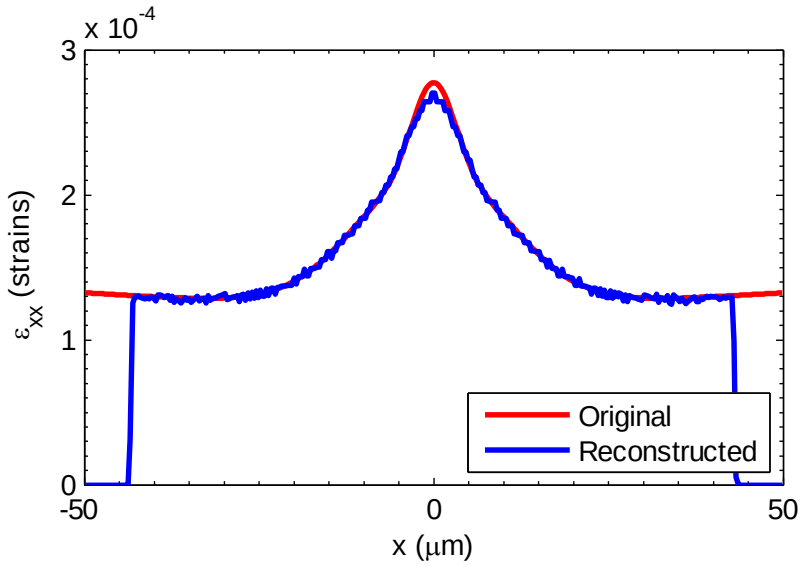

Figure 5-23- The reconstructed strain field at y=12μm with carrier frequency m=0.8, f_b=5, and $\frac{\Delta\epsilon}{\epsilon}$=0.5% and strain order 10^{-4}.

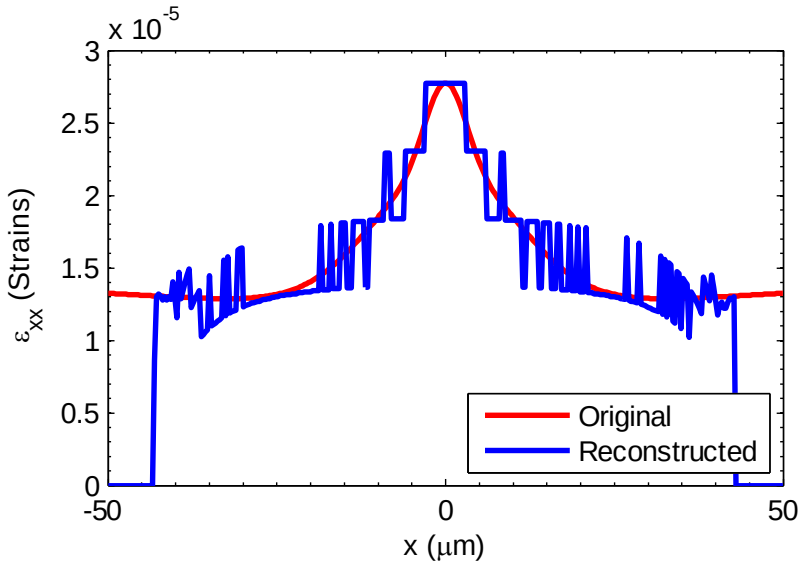

Figure 5-24- The reconstructed strain field at y=12μm with carrier frequency *m*=0.8, f_b=5, and $\frac{\Delta\epsilon}{\epsilon}$=0.5% and strain order 10^{-5}.

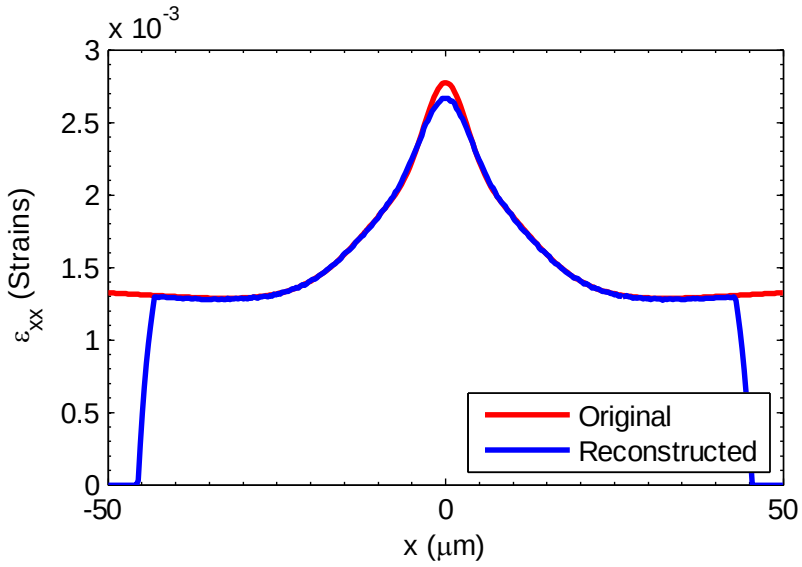

Figure 5-25- The reconstructed strain field at y=12μm with carrier frequency *m*=0.8, f_b=5, and $\frac{\Delta\epsilon}{\epsilon}$=0.5% and strain order 10^{-3}.

It is also worthwhile to evaluate the efficiency of the extraction algorithm at discontinuities in the domain. This discontinuity can be a geometric inclusion in the specimen like a notch, perforation, or a crack. For this purpose the strain data at the center of the domain of Figure 5-20 , i.e. y=0μm is evaluated. As it is shown in Figure 5-26, up to about a distance of 5μm away from the edge of the hole, the reconstructed strain data are not reliable and are, therefore, set to zero in this figure. This discrepancy is resulted from the first order approximation of the equation (5-14) and also the bandwidth of the wavelet family in spatial domain that for a certain distance from the discontinuity its effect is still included in the transformation.

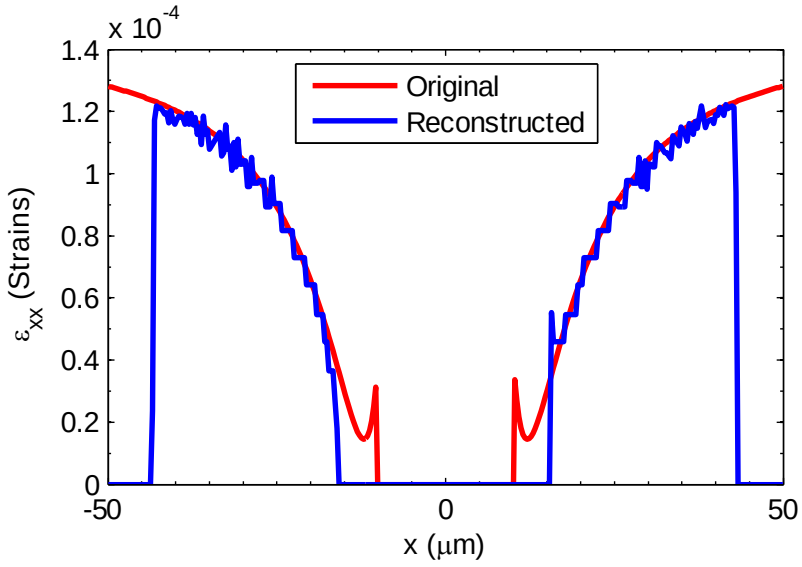

Figure 5-26- The reconstructed strain field at y=0μm with carrier frequency *m*=0.8, f_b=5, and $\frac{\Delta\epsilon}{\epsilon}$=0.5% and strain order 10^{-4}.

The reconstructed strain field for half the width of the domain is shown in Figure 5-27 and is compared to the original strain field in the same domain. As it was discussed earlier the strain values up to a 5μm distance from the edge of the hole is set to zero.

Since the method is very sensitive to noise at small spatial bandwidth, the results are not presented here. More investigations are required to reliably extract the strain information in presence of noise in nonuniform fields.

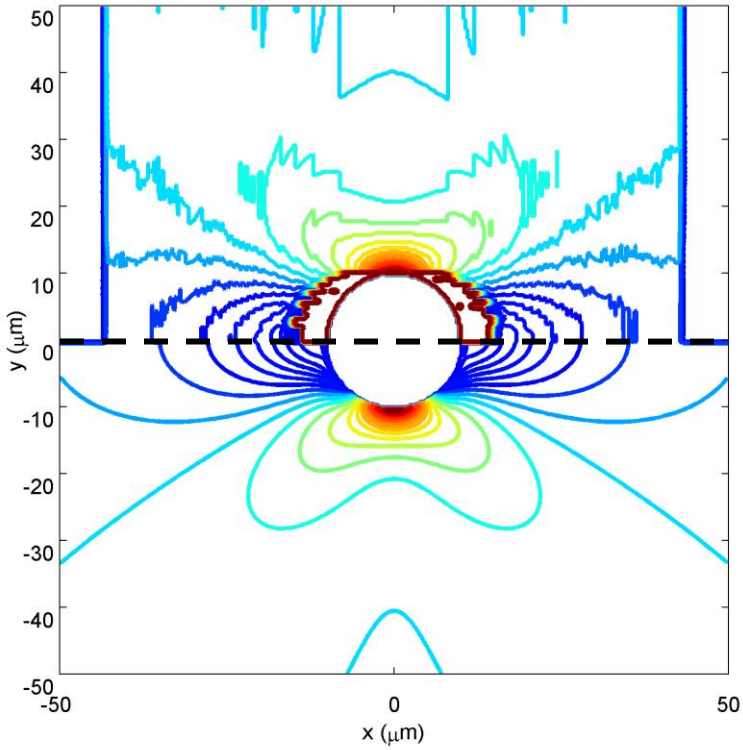

Figure 5-27- Reconstructed (top) and original (bottom) strain in a plate with hole.

5.4 Summary

In this chapter, the phase stepping and continuous wavelet transformation (CWT) techniques were introduced. Due to the high mechanical vibration level of the lab, phase stepping method was abandoned and the CWT method was therefore replaced. The CWT postprocessing is shown to be a versatile tool in extracting the local strain values. The localization and accuracy of the method was evaluated on uniform and nonuniform simulated strain fields and the effect of wavelet parameters and the noise level was studied. Wavelet parameters were tuned so as to provide the best localization, de-noising, and strain accuracy.

Chapter 6

Summary

In this research, a tensile testing device was designed to probe the mechanical behavior of thin film materials. The designed gripper was evaluated and a reliable gripping under monotonic tension was achieved. This novel gripper will address the demanding requirements for testing micro- and nano-scale thin film specimens. The device is capable of testing thin films on substrate and free-standing thin film specimens. The loading subsystem was designed to induce required stresses in the gage section. The setup is capable of loading thin film specimens under tension to investigate static, fatigue, creep, and relaxation behavior of the material. A strain measurement setup was developed based on moiré interferometry technique. The optical setup was designed and evaluated and moiré interferograms were successfully captured.

The method is capable of measuring strain field rather than only one strain value across the gage length.

A versatile microfabrication process was developed to fabricate thin film dog-bone specimens. The process can efficiently accommodate any metallization layer and can be used for process temperatures up to 100ºC. In this research aluminum was used as the metallization layer. Fabricated films were characterized by SEM, AFM, and TEM. The films had columnar micro-structure. Growth hillocks were formed during sputtering of the film. TEM analysis showed that they existed from the beginning of the deposition process and is formed as large grains sticking out of the surface of the film. AFM results revealed that the surface roughness of the specimen has changed for different batches of sputtering. Although constant sputtering parameters were used, different batches had different surface roughness. This anomaly can be due to the lack of control on substrate temperature and the deposition pressure.

Diffraction gratings were made on the surface of the specimen with FIB. Different beam parameters were used to mill the gratings. The diffraction efficiency of the gratings were studied and a grating geometry that provides the best diffraction efficiency and yet the less damage to the specimen was chosen. The Ga ion is known to cause structural damage to the sample during FIB milling of the gratings. The ion induced damage was studied by STEM and EDS. The studies showed that Ga has been implanted in the film and might have caused damage to the specimen.

In order to extract the strain field data, phase stepping method was evaluated and the required optical setup was integrated in the device. However, due to the high

vibration level of the laboratory, this method did not provide reliable strain data. Therefore, the continuous wavelet transform (CWT) was used to extract the local strain values. The local strain values were shown to be located on the ridge of the wavelet. This fact was mathematically proved for the case of Morlet wavelet. The localization properties and accuracy of the method was evaluated on simulated strain fields. The method was used to extract the strain value from simulated uniform interferograms. The wavelet parameters were tuned to achieve best accuracy. The method was also tested on interferograms in presence of noise and by adjusting the wavelet parameters, the de-noising capabilities of the wavelet transform was demonstrated. In order to evaluate the localization and spatial resolution of the method, the analytic solution of infinite plane with a hole under tension was used to simulate an interferogram representing nonuniform strain field. The wavelet parameters as well as the carrier fringe frequency were studied and the spatial resolution and strain accuracy of the method were evaluated.

6.1 Recommendations

For the future work, the following recommendations are suggested:

1. The experimental results have to be verified and the test setup needs to be calibrated;
2. The current microfabrication process is limited to processes that are below 100ºC. The main limiting part of the process is the sacrificial layer which

drastically flows in temperatures higher than 100ºC. A cross-linking process by UV irradiation was tried; however, no reliable results were achieved to date. The UV cross-linking process needs more investigation to achieve a sacrificial layer that has higher thermal stability.

3. The ion damage to the sample during the FIB milling of diffraction gratings is one of the issues that require more investigation. The microstructural studies can be continued in order to assess the level of the ion induced damage.
4. Most of the background noise can be removed from the interferogram data by a phase step of π. This phase stepping can be achieved in presence of mechanical vibrations. This method can also be integrated into the post-processing to remove the background noise, especially in nonuniform strain field measurements.
5. The strain measurement method is versatile enough to be used for device level characterizations other than the tensile testing. This advantage needs to be investigated in more details in future.
6. A FIB-assisted pseudo hole-drilling method was proposed to measure the residual stress in thin film materials, utilizing the strain field information provided by moiré interferometry and CWT. This capability of the method needs more investigations in future to develop a versatile tool in the local characterization of residual stresses in thin film materials.

References

[1] Tuck, K., Jungen A., Geisberger, Ellis, M., and Skidmore, G., “A study of creep in polysilicon MEMS devices”, Journal of Engineering Materials and Technology, Vol. 127, 2005, pp. 90-96.

[2] Paryab, N., Jahed, H., and Khajepour, A., “Failure mechanisms of MEMS thermal actuators”, Proceedings of the ASME IMECE, 2006.

[3] Mulhstein, C. L., Brown, S. B., and Ritchie, R. O., “High cycle fatigue of single crystal silicon thin films”, Journal of Microelectromechanical Systems, Vol. 10, No. 4, 2001, pp. 593-600.No. 4, 2001, pp. 593-600.

[4] Shrotriya, P., Allameh, S. M., and Soboyejo, W. O., "On the evolution of surface morphology of polysilicon MEMS structures during fatigue", Mechanics of Materials, Vol. 36, 2004, pp. 35-44.

[5] Eberl, C., Spolenak, R., Arzt, E., Kubat, F., Leidl, A., Ruile, W., and Kraft, O., "Ultra high-cycle fatigue in pure Al films and line structures", Materials Science and Engineering A, Vol. 421, 2006, pp. 68-76.

[6] Larsen, k. P., Rasmussen, A. A., Ravnkilde, J. T., Ginnerup, M., and Hansen, O., "MEMS device for bending test: measurements of fatigue and creep of electroplated nickel", Sensors and Actuators A, Vol. 103, 2003, pp. 156-164.

[7] Park, J. H., Kim, Y. J., and Choa, S. H., "Mechanical properties of Al-3%Ti thin films for reliability analysis of RF MEMS switch", Key Engineering Materials, Vol. 306-308, 2006, pp. 1319-1324.

[8] Modlinski, R., Witvrouw, A., Ratchev, P., Jourdain, A., Simons, V., Tilmans, H. A. C., Toonder, J. M. J., Puers, R., and De Wolf, I., "Creep as a reliability problem in MEMS", Microelectronics Reliability, Vol. 44, 2004, pp. 1733-1738.

[9] Gall, K., West, N., Spark, K., Dunn, M. L., and Finch, D. S., "Creep of thin film Au on biomaterial Au/Si microcantilevers", Acta Materialia, Vol. 52, 2004, pp. 2133-2146.

[10] Sontheimer, A. B., "Digital Micromirror Device (DMD) hinge memory lifetime reliability modeling", Proceedings of IEEE International Reliability Physics Symposium, 2002, pp. 118-121.

[11] van Spengen, W. M., "MEMS reliability from a failure mechanisms perspective", Microelectronics Reliability, Vol. 43, 2003, pp. 1049-1060.

[12] Gudmundson, P., and Wikstrom, A., "Stresses in thin films and interconnect lines", Microelectronics Engineering, Vol. 60, 2002, p. 17-29.

[13] Huang, M., Suo, Z., and Ma, Q., "Plastic ratcheting induced cracks in thin film structures", Journal of the Mechanics and Physics of Solids, Vol. 50, 2002, pp. 1079-1098.

[14] He, M. Y., Evans, A. G., and Hutchinson, J. W., "The ratcheting of compressed thermally grown thin films on ductile substrate", Acta Materialia, Vol. 48, pp. 2593-2601.

[15] Li, T., and Suo, Z., "Deformability of thin metal films on elastomer substrates", International Journal of Solids and Structures, Vol. 43, 2006, pp. 2351-2363.

[16] Tsui, T. Y., McKerrow, A. J., and Vlassak, J. J., "Constraint effect on thin film channel cracking behavior", Journal of Materials Research, Vol. 20, 2005, pp. 2266-2273.

[17] He, J., Suo, Z., Marieb, T. N., and Maiz, J. A., "Electromigration lifetime and critical void volume", Applied Physics Letters, Vol. 85, 2004, pp. 4639-4641.

[18] Wang, G., Ho, P. S., and Groothuis, S., "Chip-packaging interaction: a critical concern for Cu/Low-k packaging", Microelectronics Reliability", Vol. 45, 2005, pp. 1079-1093.

[19] Sridhar, N., Srolovitz, D. J., and Suo, Z., "Kinetics of buckling of a compressed film on a viscous substrate", Applied Physics Letters, Vol. 78, 2001, pp. 2482-2484.

[20] Xiang, Y., "Plasticity in Cu thin films: an experimental investigation of the effect of microstructure", PhD Dissertation, Harvard University, 2005.

[21] Oliver, W. C., and Pharr, G. M., “Measurement of hardness and elastic modulus by instrumented indentation: Advances in understanding and refinements to methodology”, Journal of Materials Research, Vol. 19, 2004, pp. 3-20.

[22] Vlassak, J. J., and Nix, W. D., “A new buldge test technique for the determination of Young’s modulus and Poisson’s ratio of thin films”, Journal of Materials Research, Vol. 7, 1992, pp. 3242-3249.

[23] Xiang, Y., Chen, X., and Vlassak, J. J., “Plane-strain buldge test for thin films”, Journal of Materials Research, Vol. 20, 2005, pp. 2360-2370.

[24] Freund, L. B., and Suresh, S., “Thin Film Materials, Stress, Defect Formation and Surface Evolution”, Cambridge University Press, Cambridge, UK, 2003.

[25] Ruud, J. A., Josell, D., Spaepen, F., and Greer, A. L., “A new method for tensile testing of thin films”, Journal of Materials Research, Vol. 8, No.1, 1993, pp. 112-117.

[26] Koskinen, J., Steinwall, J. E., Soave, R., and Johnson, H. H., “Microtensile testing of free-standing polysilicon fibers of various grain sizes”, Journal of Micromechanics and Microengineering, Vol. 3, 1993, pp. 13-17.

[27] Read, D. T., and Dally, J. W., “A new method for measuring the strength and ductility of thin films”, Journal of Materials Research, Vol. 8, No. 7, 1993, pp. 1542-1549.

[28] Huang, H., and Spaepen F., “Tensile testing of free-standing Cu, Ag, and Al thin films and Ag/Cu multilayers”, Acta Materialia, Vol. 48, 2000, pp. 3261-3269.

[29] Yu, D. Y. W., and Spaepen, F., "The yield strength of thin copper films on Kapton", Journal of Applied Physics, Vol. 95, No. 6, 2204, pp. 2991-2997.

[30] Yu, D. Y. W., "Microtensile testing of free-standing and supported metallic thin films", PhD Dissertation, Harvard University, 2003.

[31] Read, D. T., "Piezo-actuated microtensile test apparatus", Journal of Testing and Evaluation, Vol. 26, No. 3, 1998, pp. 255-259.

[32] Cornella, G., "Monotonic and cyclic testing of thin film materials for MEMS applications", PhD Dissertation, Stanford University, 1999.

[33] Zhang, P., Lee, H. J., and Bravman, "Mechanical testing of free-standing aluminum microbeams for MEMS application", in Mechanical Properties of Structural Films, Ed. Mulstein, C. and Brown, S. B., ASTM STP 1413, 2001.

[34] Lee, H. J., Zhang, P., and Bravman J. C., "Stress relaxation in free-standing aluminum beams", Thin Solid Films, Vol. 476, 2005, pp. 118-124.

[35] Lee, H. J., Cornella, G., and Bravman J. C., "Stress relaxation of free-standing aluminum beams for microelectromechanical systems applications", Applied Physics Letters, Vol. 76, No. 23, 2000, pp. 3415-3417.

[36] Lee, H. J., Zhang, P., Bravman, J. C., "Study on the strength and elongation of free-standing Al beams for microelectromechanical systems applications", Applied Physics Letters, Vol. 84, No. 6, 2004, pp. 915-917.

[37] Lee, H. J., Zhang, P., Bravman, J. C., "Tensile failure by grain thinning in micromachined aluminum thin films", Journal of Applied Physics, Vol. 93, No. 3, 2003, pp. 1443-1451.

[38] Read, D. T., "Young's modulus of thin film by speckle interferometry", Measurement Science and Technology, Vol. 9, 1998, pp. 676-685.

[39] Cheng, Y. W., Read, T. D., McCloskey, J. D., and Wright, J. E., "A tensile-testing technique for micrometer-sized free-standing thin films", Thin Solid Films, Vol. 484, 2005, pp. 426-432.

[40] Sharpe, W. N., Yuan, B., and Edwards, R. L., "A new technique for measuring the mechanical properties of thin films", Journal of Microelectromechanical Systems", Vol. 6, No. 3, 1997, pp. 193-199.

[41] Yuan, B., and Sharpe, W. N., "Mechanical testing of polysilicon thin films with the ISDG", Experimental Techniques, Vol. , No. , 1997, 32-35.

[42] Sharpe, W. N., Bagdahn, J., Jackson K., and Coles , G., "Tensile testing of MEMS materials – recent progress", Journal of Materials Science, Vol. 38, 2003, pp. 4075-4079.

[43] Oh, C. S., and Sharpe, W. N., "Techniques for measuring thermal expansion and creep of polysilicon", Sensors and Actuators A, Vol. 112, 2004, pp. 66-73.

[44] Edwards, R. L., Coles, G., and Sharpe, W. N., "Comparison of tensile and buldge tests for thin film silicon nitride", Experimental Mechanics, Vol. 44, No. 1, 2004, pp. 49-54.

[45] Sharpe, W. N., "An interferometric strain/displacement measurement system", NASA Technical Memorandum 101638, 1989.

[46] Sharpe, W. N., "The interferometric strain gage", Experimental Mechanics, Vol. 8,No. 4, 1968, pp. 164-170.

[47] Sharpe, W. N., "Application of the interferometric strain/displacement gage", Optical Engineering, Vol. 21, No. 3, 1982, pp. 483-488.

[48] Li, K., and Sharpe, W. N., "Viscoplastic behavior of a notch root at 650ºC: ISDG measurement and finite element modeling", Journal of Engineering Materials and Technology, Vol. 118, 1996, pp. 88-93.

[49] Born, M., and Wolf, E., "Principles of Optics: Electromagnetic Theory of Propagation, Interference, and Diffraction of Light", Cambridge University Press, Cambridge, UK, 1983.

[50] Zupan, M. and Hemker, K. J., "High temperature microsample tensile testing of γ-TiAl", Materials Science and Engineering A, Vol. 319-321, 2001, pp. 810-814.

[51] Zupan, M., Hayden, C., Boehlert, C. J., and Hemker, K. J., "Development of high temperature microsample testing", Experimental Mechanics, Vol. 41, No. 3, pp. 1-6.

[52] Emry, R. D., and Povirk, G. L., "Tensile behavior of free-standing gold films. Part I. Coarse grained films", Acta Materialia, Vol. 51, 2003, pp.2067-2078.

[53] Emry, R. D., and Povirk, G. L., "Tensile behavior of free-standing gold films. Part II. Fine grained films", Acta Materialia, Vol. 51, 2003, pp.2079-2087.

[54] Allameh, S. M., Lou, J., Kavishe, F., Buchheir, T., and Soboyejo, W. O., "An investigation of fatigue in LIGA Ni MEMS thin films", Materials Science and Engineering A, Vol. 371, 2004, pp. 256-266.

[55] Allameh, S. M., "An introduction to mechanical properties related issues in MEMS structures", Journal of Materials Science, Vol. 38, 2003, pp. 4115-4123.

[56] Chassiotis, I., and Knauss, W. G., "A new microtensile tester for the study of MEMS materials with the aid of Atomic Force Microscopy", Experimental Mechanics, Vol. 42, No. 1, 2002, pp. 51-57.

[57] Chasiotis, I., "Mechanics of thin films and microdevices", IEEE Transactions on Device and Materials Reliability, Vol. 4, No. 2, 2004, pp. 176-188.

[58] Knuass, W. G., Chasiotis, I., and Huang, Y., "Mechanical measurements at the micron and nanometer scales", Mechanics of Materials, Vol. 35, 2003, pp. 217-231.

[59] Tsuchiya, T., Tabata, O., Sakata, J., and Taga, Y., "Specimen size effect on tensile strength of surface micromachined polycrystalline silicon thin films", Proceedings of IEEE Microelectromechanical Systems, 1997, pp. 529-534.

[60] Tsuchiya, T., Tabata, O., Sakata, J., and Taga, Y., "Specimen size effect on tensile strength of surface micromachined polycrystalline silicon thin films", Journal of Microelectromechanical Systems, Vol. 7, No. 1, 1998, pp. 106-113.

[61] Chasiotis, I., and Knauss, W. G., "The mechanical strength of polysilicon films: Part 1. The influence of fabrication governed surface conditions", Journal of the Mechanics and Physics of Solids, Vol. 51, 2003, pp. 1533-1550.

[62] Chasiotis, I., and Knauss, W. G., "The mechanical strength of polysilicon films: Part 2. Size effects associated with elliptical and circular perforations", Journal of the Mechanics and Physics of Solids, Vol. 51, 2003, pp. 1551-1572.

[63] Chasiotis, I., Bateson, C., Timpano, K., McCarty, A. S., Barker, N. S., and Stanec, J. R., "Strain rate effects on the mechanical behavior of nanocrystalline Au films", Thin Solid Films, Vol. 515, No. 6, 2007, pp. 3183-3189.

[64] Zhu Y., Barthelat, F., Labossiere, P. E., Moldovan, N., Espinosa, H. D., 2003, "Nanoscale displacement and strain measurement", Proceedings of the SEM Annual Conference on Experimental and Applied Mechanics, paper 155, 2003.

[65] Haque, M. A., and Saif, M. T. A., "Deformation mechanisms in free-standing nano-scale thin films: A quantitative *in situ* transmission electron microscope study", Proceedings of the National Academy of Science, Vol. 101, No. 17, 2004, pp. 6335-6340.

[66] Haque, M. A., Saif, M. T. A., 2003, "A review of MEMS based microscale and nanoscale tensile and bending testing", Experimental Mechanics, Vol. 43, No.3, pp. 248-255.

[67] Samuel, B. A., and Haque, M. A., "Room temperature relaxation of freestanding nanocrystalline gold films", Journal of Micromechanics and Microengineering, Vol. 16, 2006, pp. 929-934.

[68] Rajagopalan, J., Han, J. H., Saif, M. T. H., "Plastic deformation recovery in freestanding nanocrystalline aluminum and gold thin films", Science, Vol. 315, 2007, pp. 1831-1834.

[69] Stance, J. R., Smith, C. H., Chasiotis, I., and Barker, N. S., "Realization of low-stress Au cantilever beams", Journal of Micromechanics and Microengineering, Vol. 17, 2007, N7-N10.

[70] Greek, S., and Johnson, S., "Tensile Testing of thin film microstructures", Proceedings of the SPIE, Vol. 3224, 1997, pp. 344-351.

[71] Greek, S., Ericson, F., Johnsson, S., and Schweitz, J. A., "In situ tensile strength measurement and Weibull analysis of thin film and thin film micromachined polysilicon structures", Thin Solid Films, Vol. 292, 1997, pp. 247-254.

[72] Buchheit, T. E., Glass, S. J., Sullivan, J. R., Mani, S. S., Lavan, D. A., Friedmann, T. a., and Janek, R., "Micromechanical testing of MEMS materials", Journal of Materials Science, Vol. 38, 2003, pp. 4081-4086.

[73] Sharpe, W. N., and Bagdahn, J., "Fatigue testing of polysilicon – A review", Mechanics of Materials, Vol. 36, No. 1-2, 2004, pp. 3-11.

[74] Zhu, Y., Ke, C., and Espinosa, H. D., "Experimental techniques for the mechanical characterization of one-dimensional nanostructures", Experimental Mechanics, Vol. 47, No. 1, 2007, pp. 7-24.

[75] Ogawa, H., Suzuki, K., Kaneko, S., Nakano, Y., Ishikawa, Y., and Kitahara, T., "Measurements of mechanical properties of microfabricated thin films", Proceedings of IEEE Microelectromechanical Systems Workshop, 1997, pp. 430-435.

[76] Zupan, M., and Hemker, K. J., "Application of Fourier analysis to the laser based interferomteric strain/displacement gage", Experimental Mechanics, Vol. 42, No. 2, 2002, pp. 214-220.

[77] Hemker, K. J. and Sharpe, W. N., "Microscale characterization of mechanical properties", Annual Review of Materials Research, Vol. 37, 2007, pp. 93-126.

[78] Chasiotis, I., Cho, S. W., and Jonnalagadda, K., "Fracture toughness and subcritical crack growth in polycrystalline silicon", Journal of Applied Mechanics, Vol. 73, No. 5, 2006, pp. 714-722.

[79] Cho, S. W., Jonnalagadda, K., and Chasiotis, I., "Mode I and mixed mode fracture of polysilicon for MEMS", Fatigue and Fracture of Engineering Materials and Structures, Vol. 30, No. 1, 2007, pp. 21-31.

[80] Lord Rayleigh, “On the manufacture and theory of diffraction gratings”, Philosophical Magazine, Vol. 47, 1874, pp. 193-205.

[81] Guild, J., “The Interference Systems of Crossed Diffraction Gratings; Theory of Moiré Fringes”, Oxford Press, Oxford, UK, 1956.

[82] McKelvie, J., “Moiré strain analysis: an introduction, review and critique, including related techniques and future potentials”, Journal of Strain analysis, Vol. 33, No. 2, 1998, pp. 137-151.

[83] Post, D., Han, B., and Ifju, P., “High Sensitivity Moiré”, Springer-Verlag, New York, 1994.

[84] Cloud, G. L., “Optical Methods of Engineering Analysis”, Cambridge University Press, New York, 1995.

[85] “Handbook of Moiré Measurements”, Ed. Walker, C. A., Institute of Physics Publishing, London, 2004.

[86] Walker, C. A., “A historical review of moiré interferometry”, Experimental Mechanics, Vol. 34, No. 3, 1994, pp. 281-299.

[87] Dai, F., McKelvie, J., and Post, D., “An interpretation of moiré interferometry from wavefront interference theory”, Optics and Lasers in Engineering, Vol. 12, 1990, pp. 101-118.

[88] Kern, W., and Puotinen, D. A., “Cleaning solutions based on hydrogen peroxide for use in silicon semiconductor technology”, RCA Review, Vol. 31, 1970, pp. 187-206.

[89] Cheng, J., and Steckl, A. J., "Focused ion beam fabricated microgratings for integrated optics applications", IEEE Journal of Selected Topics in Quantum Electronics, Vol. 8, No. 6, 2002, pp. 1323-1329.

[90] Chaganti, K., Salakhutdinov, I., Avrutsky, I., and Auner, G. W., "Sub-micron grating fabrication on hafnim oxide thin film waveguides with focused ion beam milling", Optics Express, Vol. 14, No. 4, 2006, pp. 1505-8624.

[91] Zinoviev, K. E., and Dominguez, C., "Diffraction grating couplers milled in Si_3N_4 rib waveguides with a focused ion beam", Optics express, Vol. 13, No. 21, 2005, pp.8618-8624.

[92] Soares, L. L., and Cescato, L., "Metalized photoresist grating as a polarizing beam splitter", Applied Optics, Vol. 40, No. 32, 2001, pp. 5906-5910.

[93] Gunawan, O., Hoe, L. W., Ooi, B. S., Chan, y. C., and Zhou, Y., "Development of a laser holographic interference lithography system", Proceedings of the SPIE, Vol. 3896, 1999, pp. 515-522.

[94] Giannuzzi, L. A., and Stevie, F. A., "Introduction to Focused Ion Beams: Instrumentation, Theory, Techniques, and Practice", Springer, NY, 2005.

[95] Matteson, T. L., "Electron backscattering diffraction investigation of focused ion beam surfaces", Journal of Electronic Materials, Vol. 31, 2002, pp.33-39.

[96] Mayer, J., Giannuzzi, L. A., Kamino, T., and Michael, J., "TEM sample preparation and FIB induced damage", MRS Bulletin, Vol. 32, 2007, pp.400-407.

[97] Kiener, D., Motz, C., Rester, M., Jenko, M., and Dehn, G., "FIB damage of Cu and possible consequences for miniaturized mechanical tests", Materials Science and Engineering A, Vol. 459, 2007, pp.262-272.

[98] Volkert, C. A., and Minor, A. M., "Focused ion beam microscopy and micromachining", MRS Bulletin, Vol. 32, 2007, pp. 389-395.

[99] Yu, J., Liu, J., Zhang, J., and Wu, J., "TEM investigation of FIB induced damages in preparation of metal material TEM specimens by FIB", Materials Letters, Vol. 60, 2006, pp. 206-209.

[100] Phaneuf, M. W., Li, J., and Casey, J. D., "Gallium phase formation in Cu and other FCC metals during near normal incident Ga-FIB milling and techniques to avoid this phenomenon", Microscopy and Microanalysis, Vol. 8, 2002, pp. 52-53.

[101] Park, C. M., and Bain, J. A., "Focused ion beam induced grain growth in magnetic materials for recording heads", Journal of Applied Physics, Vol. 91, 2002, pp. 6830-6832.

[102] Robinson, D. W., and Reid, G. T., "Interferogram Analysis", Institute of Physics Publishing, London, UK, 1993.

[103] Qian, K., "Two-dimensional windowed Fourier transform for fringe pattern analysis: principles, applications, and implementations", Optics and Lasers in Engineering, Vol. 45, 2007, pp. 304-317.

[104] Watkins, L. R., Tan, S. M., and Barnes, T. H., "Determination of interferometer phase distributions by use of wavelets", Optics Letters, Vol. 24, No. 13, 1999, pp. 905-907.

[105] Watkines, L. R., "Phase recovery from fringe patterns using the continuous wavelet transform", Optics and Lasers in Engineering, Vol. 45, 2007, pp. 298-303.

[106] Liu, H., Cartwright, N. A., and Basaran, C., "Sensitivity improvement in phase shifted moiré interferometry using 1-D continuous wavelet transform image processing", Optical Engineering, Vol. 42, 2003, pp. 2646-2652.

[107] Liu, H., Cartwright, N. A., and Basaran, C., "Moiré interferogram phase extraction: a ridge detection algorithm for continuous wavelet transforms", Applied Optics, Vol. 43, 2004, pp. 850-857.

[108] Sciammarella, C. A., and Kim, T., "Determination of strains from fringe patterns using space-frequency representations", Optical Engineering, Vol. 42, 2003, pp. 3182-3193.

[109] Dursun, A., Ozder, S., and Ecevit, F. N., "Continuous wavelet transform analysis of projected fringe patterns", Measurement Science and Technology, Vol. 15, 2004, pp. 1768-1772.

[110] Wang, Z., and Ma, H., "Advanced continuous wavelet transform algorithm for digital interferogram analysis and processing", Optical Engineering, Vol. 45, 2006, 045601.

[111] Federico, A., and Kaufmann, G. H., "Evaluation of the continuous wavelet transform method for the phase measurement of electronic speckle pattern interferometry fringes", Optical Engineering, Vol. 41, 2002, pp. 3209-3216.

[112] Kadooka, K., Kunoo, K., Uda, N., Ono, K., and Nagayasu, T., "Strain analysis for moiré interferometry using the two dimensional continuous wavelet transform", Experimental Mechanics, Vol. 43, No. 1, 2003, pp. 45-51.

[113] Kemao, Q., Soon, S. H., and Asundi, A., "Instantaneous frequency and its application to strain extraction in moiré interferometry", Applied Optics, Vol. 42, No. 32, 2003, pp. 6504-6512.

[114] Fu, Y., Tay, J. C., Quan, C., and Miao, H., Wavelet analysis of speckle patterns with a temporal carrier", Applied Optics, Vol. 44, No. 6, 2005, pp. 959-965.

[115] Liebling, M., Bernhard, T. F., Bachmann, A. H., Froehly, L., Lasser, T., and Unser, M., "Continuous wavelet transform ridge extraction for spectral interferometry imaging", Proceeding of the SPIE, Vol. 5690, pp. 397-402.

[116] Tay, C. J., Quan, C., un, W., and He, X. Y., "Demodulation of a single interferogram based on continuous wavelet transform and phase derivative", Optics Communications, Vol. 280, 2007, pp. 327-336.

[117] Mallat, S. A., "A Wavelet Tour of Signal Processing", Second Edition, Academic Press, CA, 2001.

[118] Delpart, N., Escudie, B., Guillemain, P., Kronland-Martinet, R., Tchamitchian, P., and Torresani, B., "Asymptotic wavelet and Gabor analysis: Extraction of instantaneous frequency", IEEE Transactions on Information Theory, Vol. 38, No. 2, 1992, pp. 644-664.

[119] Zhong, J., and Weng, J., "Phase retrieval of optical fringe patterns from ridge of a wavelet transform", Optics Letters, Vol. 30, No. 19, 2005, pp. 2560-2562.

[120] Goupillaud, P., Grossmann, A., and Morlet, J., "Cyclic-octave and related transforms in seismic signal analysis", Geoexploration, Vol. 23, 1984, pp. 85-102.

[121] HRP020 HeNe Laser Data Sheet, Thorlabs Inc., 2007.

[122] Saada, A. D., "Elasticity Theory and Applications", Second Edition, Krieger Publishing Company, FL, 1993.